

## Configurations of fluid membranes and vesicles

Udo Seifert

To cite this article: Udo Seifert (1997) Configurations of fluid membranes and vesicles, *Advances in Physics*, 46:1, 13-137, DOI: [10.1080/00018739700101488](https://doi.org/10.1080/00018739700101488)

To link to this article: <https://doi.org/10.1080/00018739700101488>



Published online: 28 Jul 2006.



Submit your article to this journal 



Article views: 3727



Citing articles: 922 [View citing articles](#) 

## Configurations of fluid membranes and vesicles

By UDO SEIFERT

Max-Planck-Institut für Kolloid- und Grenzflächenforschung, Kantstr. 55,  
14153 Teltow-Seehof, Germany

[Received 23 October 1995; accepted 14 February 1996]

### Abstract

Vesicles consisting of a bilayer membrane of amphiphilic lipid molecules are remarkably flexible surfaces that show an amazing variety of shapes of different symmetry and topology. Owing to the fluidity of the membrane, shape transitions such as budding can be induced by temperature changes or the action of optical tweezers. Thermally excited shape fluctuations are both strong and slow enough to be visible by video microscopy. Depending on the physical conditions, vesicles adhere to and unbind from each other or a substrate.

This article describes the systematic physical theory developed to understand the static and dynamic aspects of membrane and vesicle configurations. The preferred shapes arise from a competition between curvature energy, which derives from the bending elasticity of the membrane, geometrical constraints such as fixed surface area and fixed enclosed volume, and a signature of the bilayer aspect. These shapes of lowest energy are arranged into phase diagrams, which separate regions of different symmetry by continuous or discontinuous transitions. The geometrical constraints affect the fluctuations around these shapes by creating an effective tension.

For vesicles of non-spherical topology, the conformal invariance of the curvature energy leads to conformal diffusion, which signifies a one-fold degeneracy of the ground state. Unbinding and adhesion transitions arise from the balance between attractive interactions and entropic repulsion or a cost in bending energy, respectively. Both the dynamics of equilibrium fluctuations and the dynamics of shape transformations are governed not only by viscous damping in the surrounding liquid but also by internal friction if the two monolayers slip over each other. More complex membranes such as that of the red blood cell exhibit a variety of new phenomena because of coupling between internal degrees of freedom and external geometry.

Contents	PAGE
1. Introduction	16
1.1. Vesicles	16
1.2. Overview	21
1.3. Chemistry and thermodynamics	23
2. Curvature models	25
2.1. Local curvature energy in the classical model	25
2.2. Almost planar membrane and persistence length	27
2.3. Coupling between curvature and density	28
2.4. Global energy of a vesicle shape	32
2.4.1. Gauss–Bonnet theorem	32
2.4.2. Osmotic pressure	32
2.4.3. Minimizing with respect to lipid densities	32
2.4.4. Effective constraint on area and volume	33

2.4.5. Area-difference-elasticity model	34
2.5. A brief history of variants of the curvature model	35
2.5.1. Minimal model: local curvature energy only	35
2.5.2. Spontaneous curvature model	35
2.5.3. Bilayer couple model	36
2.5.4. Area-difference-elasticity model	36
2.5.5. Area-difference-elasticity model with spontaneous curvature	36
2.5.6. Summary of curvature models	36
3. Shapes and shape transformations	37
3.1. Stationary shapes	37
3.1.1. General energy functional and equivalence of the ensembles	37
3.1.2. Shape equation and scale invariance of the local curvature energy	39
3.1.3. Expansion around the sphere	40
3.1.4. Axisymmetric shapes	40
3.1.5. Limit shapes and neck condition	41
3.1.6. Cylinders and unduloids	42
3.2. Complementary techniques for shape determination	43
3.2.1. Variational approaches	43
3.2.2. Direct numerical minimization	43
3.3. Continuous and discontinuous transitions	43
3.4. A simple model: local curvature energy only	45
3.5. Bilayer-couple model	46
3.6. Area-difference-elasticity model	48
3.6.1. Mapping property	48
3.6.2. Phase diagram for $\alpha = 1.4$	50
3.7. Spontaneous curvature model	51
3.8. Temperature trajectories	51
3.9. Budding transition	54
3.9.1. Apparently conflicting experimental scenarios	54
3.9.2. Spinodal fluctuations	55
3.10. Other shape transformations	56
3.10.1. Re-entrant trajectory	56
3.10.2. Discocyte–stomatocyte transition	57
3.10.3. Equilibrium area difference as control parameter	57
3.10.4. Starfish vesicles	57
3.10.5. Membranes in electric fields	59
3.11. Shape changes induced by optical tweezers	59
4. Fluctuations	59
4.1. Gaussian fluctuations with constraints	60
4.1.1. Mode expansion	60
4.1.2. Correlation functions and effective tension	62
4.1.3. Stability	63
4.1.4. Thermal shift of the mean shape	63
4.1.5. Spherical limit	64
4.2. Quasi-spherical vesicles	64
4.2.1. Expansion around the sphere	64
4.2.2. Exact treatment of the area constraint	65
4.2.3. Conventional approach with effective tension	66
4.3. Monte Carlo simulations of very flexible vesicles	68
4.3.1. Two-dimensional vesicles	69
4.3.2. Three-dimensional vesicles	69
5. Vesicles of non-spherical topology	69
5.1. Conformal invariance of the local curvature energy	70
5.2. Willmore surfaces and the Willmore problem	71

5.2.1. Genus 0	71
5.2.2. Genus 1	71
5.2.3. Genus 2	72
5.2.4. Genus $\geq 3$	74
5.2.5. Energy of handles	74
5.3. Constraints and conformal invariance	74
5.3.1. Expansion for special conformal transformations	74
5.3.2. Symmetry of stationary shapes	75
5.3.3. Stability with respect to special conformal transformations	76
5.4. Shapes and phase diagrams for genus 1	76
5.4.1. Phase diagrams	76
5.4.2. Experiments	78
5.5. Shapes and phase diagram for genus 2	78
5.5.1. Conformal diffusion	78
5.5.2. Phase diagram beyond the conformal phase	80
5.6. Vesicles of higher genus	80
6. Adhesion	81
6.1. Experimental methods	82
6.1.1. Force apparatus	82
6.1.2. Osmotic stress method	83
6.1.3. Optical microscopy	83
6.1.4. Micropipette aspiration	83
6.1.5. Reflection interference contrast microscopy	83
6.2. Bound planar membranes	83
6.2.1. Direct interactions	84
6.2.2. Steric interaction in the presence of lateral tension	85
6.2.3. Unbinding transition	87
6.3. Adhesion in a contact potential	88
6.3.1. Contact potential and contact curvature	88
6.3.2. Curvature-driven adhesion transition	89
6.3.3. Strong adhesion: effective contact angle	91
6.3.4. Strong adhesion: adhesion-induced rupture and fusion	92
6.4. Adhesion in a potential with finite range: the pinned state	93
6.5. Self-consistent theory	95
6.6. Adhesion under gravity	98
6.7. Focal adhesion	100
7. Dynamics	100
7.1. Equations of motion	101
7.2. Almost planar membrane: classical model	103
7.3. Almost planar membrane: bilayer dynamics	105
7.3.1. Force balance	105
7.3.2. Dispersion relation and height-height correlation function	107
7.3.3. Experimental aspects	108
7.4. Relaxation of quasi-spherical modes	109
7.5. Dynamics of a bound fluid membrane	110
7.5.1. Hydrodynamics near a substrate	110
7.5.2. Damping rate and correlation function	111
7.5.3. Effect of bilayer architecture	112
7.6. Pearlning instability of cylindrical vesicles	113
7.6.1. Experimental facts	113
7.6.2. Theoretical modelling	114
8. More complex membranes	115
8.1. Mixed and inhomogeneous membranes	115
8.1.1. Curvature-induced phase separation	115
8.1.2. Domain-induced budding	118

8.1.3. Membranes with inclusions	119
8.2. Fluid membranes with internal degrees of freedom	119
8.3. Polymerized membranes and vesicles	120
8.3.1. Fluctuating almost flat polymerized membranes	120
8.3.2. Fluctuating polymerized vesicles	121
8.3.3. Stiff polymerized vesicles	121
8.4. Red blood cell membrane	121
Acknowledgements	122
Appendix A. List of recurrent symbols	123
Appendix B. Determination of the bending rigidity	125
References	126

## 1. Introduction

### 1.1. Vesicles

Membranes as studied in this article consist of a bilayer of lipid molecules that are composed of a hydrophilic head and two hydrophobic hydrocarbon chains. When introduced into an aqueous environment, these amphiphilic molecules aggregate spontaneously into two mono-molecular layers held together by weak non-covalent forces due to the hydrophobic effect. These membranes form large encapsulating ‘bags’ called *vesicles* because open sheet-like configurations would involve a large energy along the hydrophobic edges. Even though the membrane is only a few nanometres thick, the size of these vesicles can reach macroscopic dimensions of up to 100 micrometres. Video microscopy reveals both an extreme softness of the membrane, since thermally excited shape fluctuations are strong enough to become visible, and an amazing variety of different shapes, among which shape transformations can be induced by changing parameters like the temperature or osmotic conditions.

Interest in these systems arises from at least three perspectives emphasizing (i) the unique material properties of a fluid membrane resulting from its molecular architecture (the *physical chemistry* aspect), (ii) the enormous variety of configurations exhibited by membranes considered as two-dimensional (2D) surfaces (the *statistical physics* point of view), and (iii) the ubiquitousness of membranes in *biological* systems. Before we return to these aspects later in this introduction, a few examples will serve to introduce the physical object of this study.

The most prominent example of a shape transformation is the budding transition shown in figure 1, where the shape change of an initially spherical vesicle is recorded with video microscopy. As the temperature increases, the sphere becomes a prolate ellipsoid. While this transformation may seem inevitable given that the thermal expansion of the area is much larger than that of the enclosed volume, the surprise is the occurrence of a pear shape with broken up/down symmetry as the temperature is increased further. At even higher temperature, the neck closes, resulting in two spherical compartments that are sitting on top of each other but still connected by a narrow constriction. In all but the first and last shape, the video exhibits pronounced fluctuations which the still pictures, of course, cannot convey.

The budding transition does not necessarily happen; sometimes the reflection symmetry is restored upon further heating, as shown in the re-entrant sequence displayed in figure 2. Alternatively, the spherical shape can become oblate after a temperature increase. This shape then develops into a discocyte with subsequent transformation into a stomatocyte as shown in figure 3. This sequence is particularly

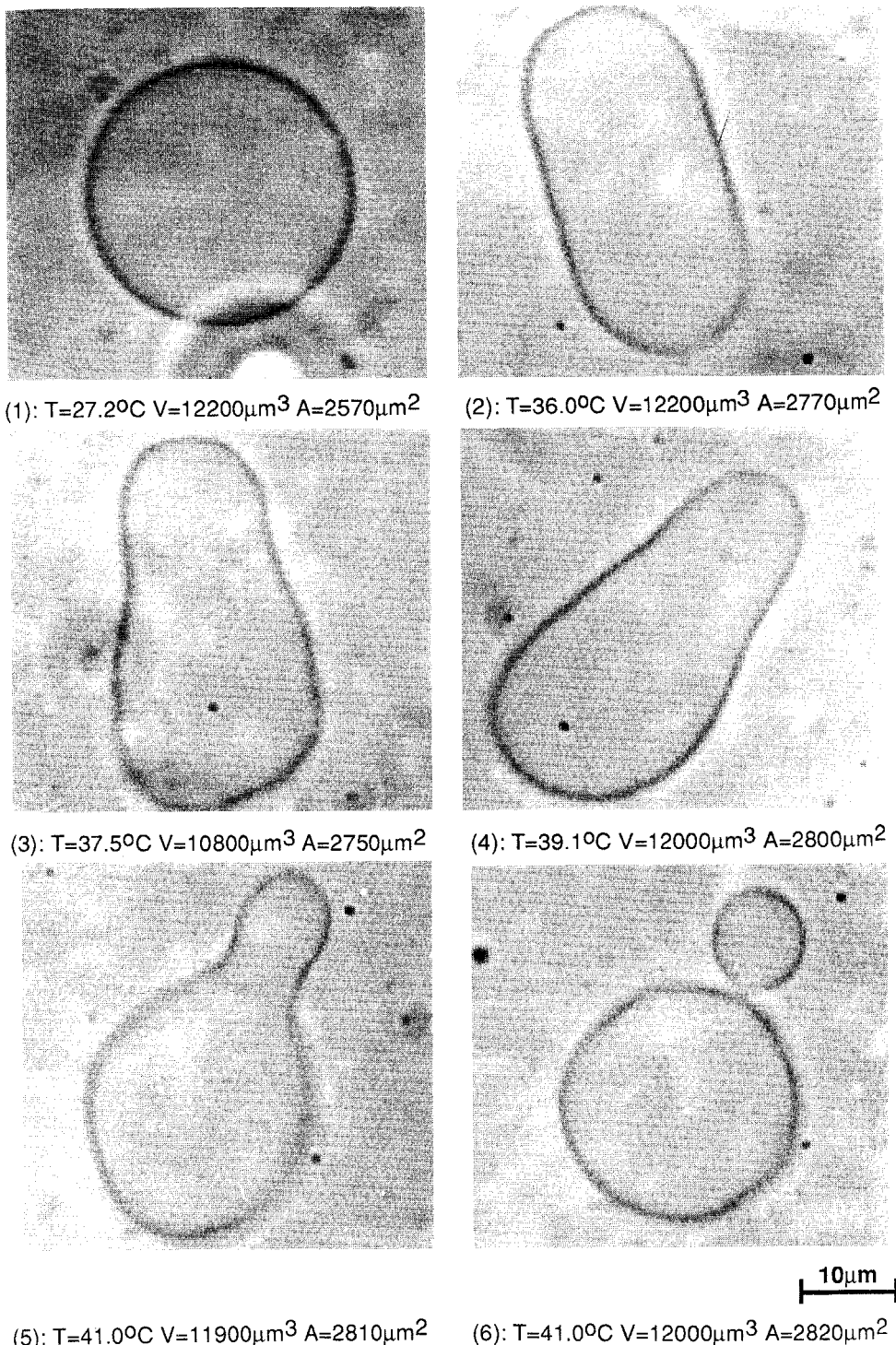


Figure 1. Budding transition. The temperature increases from 27.2, 36.0, 37.5, 39.1, 41.0 to 41.0°C from left to right and top to bottom (Käss and Sackmann 1991).

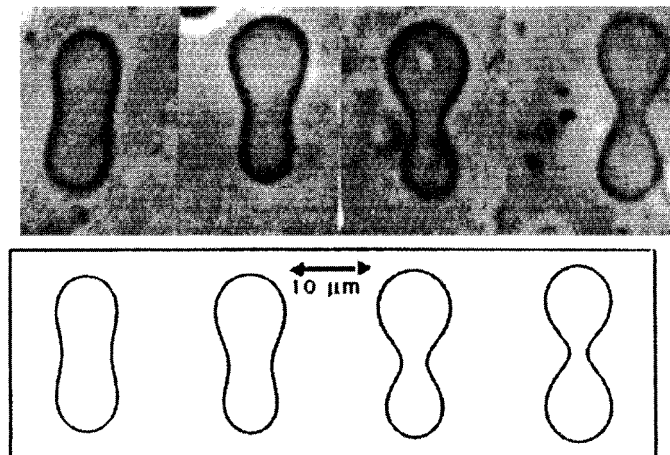


Figure 2. Re-entrant transition. The temperature increases from 20.7, 32.6, 40.0, to 44.3°C from left to right. The theoretical curves have been obtained with the BC model as discussed in section 3.10.1 (Berndl *et al.* 1990).

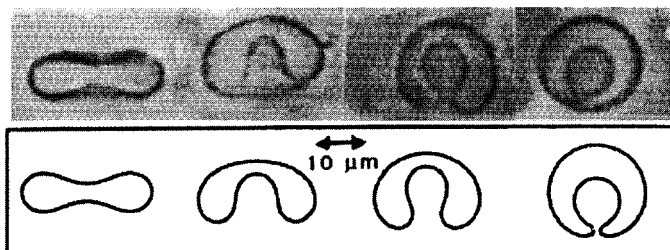


Figure 3. Discocyte/stomatocyte transition. The temperature increases from 43.8, 43.9, 44.0, to 44.1°C from left to right. The theoretical curves show the contour of corresponding stationary shapes (Berndl *et al.* 1990).

interesting since the discocytes look very much like the rest shape of red blood cells. Indeed, the quest for understanding the biconcave shape of the red blood cell motivated much of the earlier work on vesicles.

A significant shape change such as budding illustrates that fluidity is an important material property of this system. These shape transformations would hardly be possible if the membrane resisted shear. Still, the bilayer structure is quite robust; neither mesoscopic pores nor holes are formed, nor does the topology of the vesicle change since the buds are usually not fissioned from the mother vesicles.

Even though the topology remains the same on the timescale of minutes to hours on which these shape changes are recorded, vesicles of non-spherical topology do exist. Some of the experimentally observed shapes are shown in figure 4 for genus 1 (one hole), in figure 5 for genus 2 (two holes), and in figure 6 for higher genus, respectively. Characteristic for the latter shape are strong fluctuations of the position of the necks.

The dynamics of membrane configurations under non-equilibrium conditions has become accessible using laser tweezers. Figure 7 shows how an initially cylindrical vesicle hit by a laser spot develops a propagating peristaltic mode which finally transforms the cylinder into a sequence of pearls connected by a thin tether.

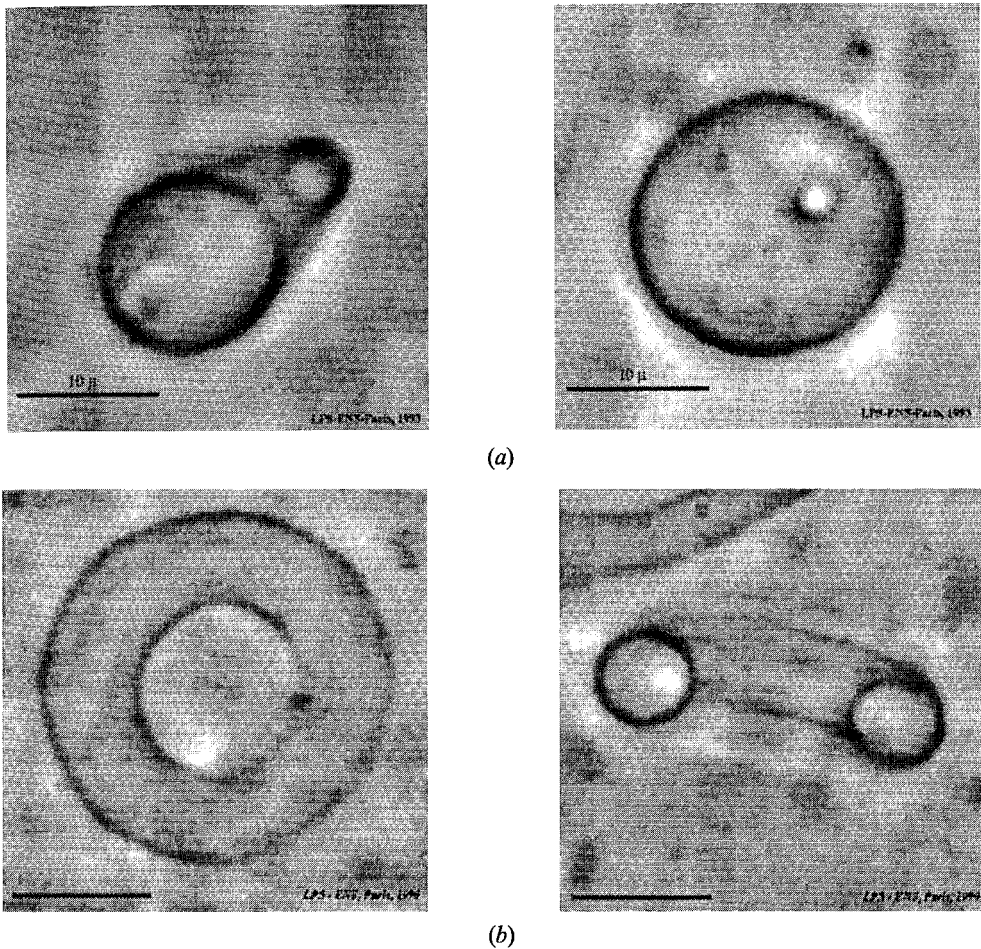


Figure 4. Toroidal vesicles: (a) a non-axisymmetric torus, (b) an axisymmetric circular torus. The bar denotes 10  $\mu\text{m}$  (Michalet and Bensimon 1995a).

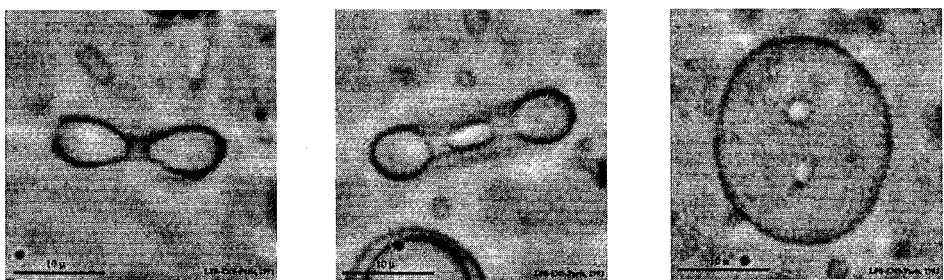


Figure 5. Three views of a vesicle with genus 2, the 'button' surface. The bar denotes 10  $\mu\text{m}$  (Michalet 1994).

For a theoretical description on mesoscopic length scales much larger than the bilayer thickness, membranes can be considered as 2D surfaces embedded in three-dimensional (3D) space. Their configurations, however, are fundamentally distinct from interfaces since they are not determined by a surface tension but rather by

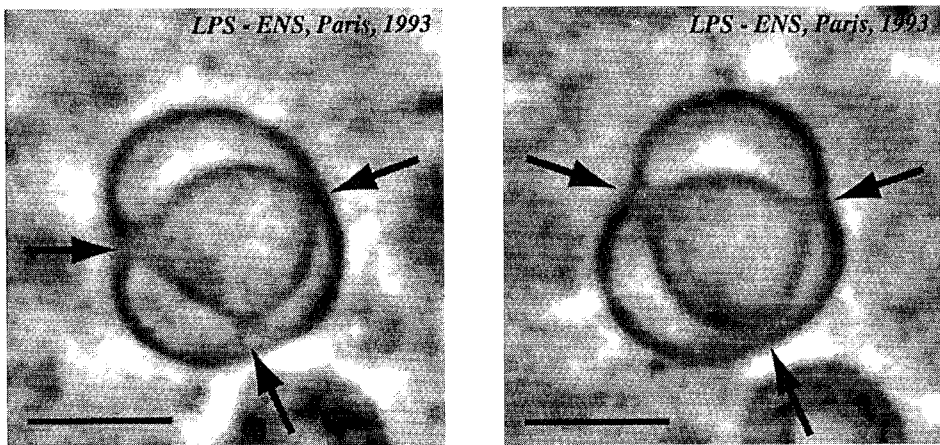


Figure 6. Vesicles of higher genus. The arrows point to necks whose positions strongly fluctuate. The bar denotes 10  $\mu\text{m}$  (Michalet *et al.* 1994a).

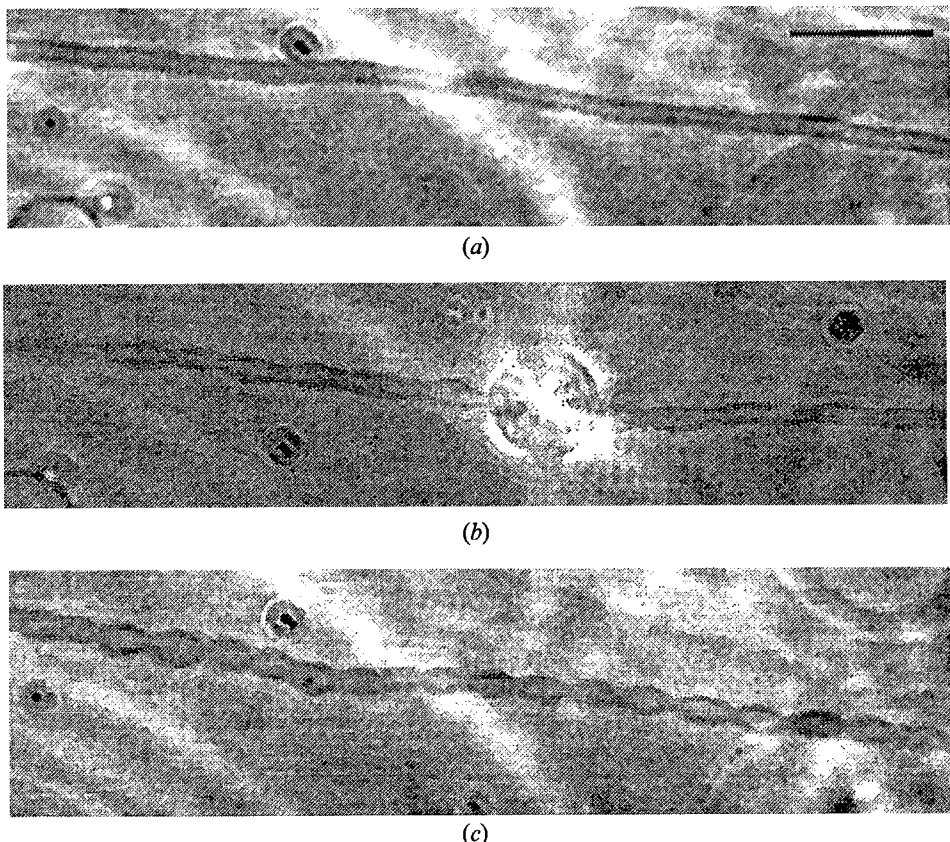


Figure 7. Laser-induced pearling instability of cylindrical vesicles. (a) Section of DMPC tube, (b) initial instability upon tweezing marked by the circular reflection. State (c) eventually decays back to state (a) if the laser is shut off. The bar denotes 10  $\mu\text{m}$  (Bar-Ziv and Moses 1994).

bending elasticity as introduced independently more than twenty years ago in three seminal papers (Canham 1970, Helfrich 1973, Evans 1974). This fundamental difference is the reason for the great variety of non-spherical shapes of vesicles, in contrast to the characteristic spherical equilibrium shapes of simple liquids which are governed by isotropic surface tension.

Bending elasticity or, in its mathematical formulation, curvature energy not only generates a large variety of shapes, it also leads to different fluctuation or excitation spectra of these shapes and different dynamics than is shown by simple liquid interfaces. As will be seen, these phenomena require different mathematical tools for their description, such as conformal transformations in three dimensions. The fact that these mathematical concepts become visible in the microscope definitely contributes to the appeal of these systems to statistical physicists. From a different perspective, these membranes also have a close resemblance to certain string models studied in high-energy physics, since the world sheet of a closed string is akin to a vesicle even though the embedding dimension in these string models may be much higher than three (Polyakov 1987, Wheater 1994).

A prime motivation to investigate membranes arises from biology in our 3D world. The lipid bilayer is the most elementary and indispensable structural component of biological membranes, which form the boundary of all cells and cell organelles (Alberts *et al.* 1989). In biological membranes, the bilayer consists of many different lipids and other amphiphiles. Biomembranes are ‘decorated’ with embedded membrane proteins, which ensure the essential functional properties of a biomembrane such as ion pumping, conversion from light energy to chemical energy, and specific recognition. Often a polymeric network is anchored to the membrane endowing it with further structural stability. This stability is particularly spectacular in red blood cells which can squeeze through tiny capillaries and still recover their rest shape countless times in a life cycle.

Understanding the physical properties of the bilayer through the study of vesicles should provide valuable insight into the physical mechanisms that also govern the more complex biomembranes for which, from this perspective, the artificial vesicle is a model system. Striking phenomenological similarities between the budding transition as shown in figure 1 and exo-cytosis where small vesicles bud off the cell membrane encourage a thorough analysis of these artificial membranes.

Referring to the biological motivation, a distinction has been emphasized between classical ‘biophysics’ and a field which acquired the somewhat fancy notion of ‘biologically inspired physics’ (Peliti 1991). While the former field is concerned with the detailed modelling of real biological processes—often at the cost of many parameters in a theoretical description—the latter approach takes the biological material as inspiration for asking questions biologists often may not even find relevant (yet). Even though the present work originates in the latter approach, an optimist would hope for a reconciliation of these perspectives in the future. The impressive success biomedical applications of vesicles (often called ‘liposomes’ in this field) have already reached in areas like drug delivery (Cevc 1995, Lasic 1995) proves that at least some crucial mechanisms of biological systems have already been identified correctly by studying these model systems.

### 1.2. Overview

A systematic theory of vesicle configurations is the topic of this article. ‘Configurations’ is used here in a broad sense including not only the mean shapes

as illustrated above but also the thermal excitations of these shapes, the shapes of vesicles adhering to a substrate and dynamical aspects of these configurations.

To transform the basic concept of curvature energy as introduced twenty years ago into a systematic quantitative theoretical description remained a challenge for quite some time. In particular, the implementation of the fact that the membrane is a bilayer (rather than a structureless monolayer) has been controversial, giving rise to various variants of curvature models which will be presented from a unifying point of view in section 2. The starting point in this chapter is the trivial level of an almost planar membrane to which are introduced complications that arise from the closure of the membrane. The relationship between the various variants of the curvature model, which appear in the literature, are examined and incorporated under one general model.

In section 3, the methods used to calculate shapes of lowest energy are described. For the different variants of the curvature model, these shapes are arranged in phase diagrams. Such a systematic study can become the basis for a comparison between theory and experiments as is discussed in some detail for the budding transition. Other experimentally observed shape transitions are also related to the theory.

Due to the softness of the membrane, thermally excited shape fluctuations ('flickering') are visible under a microscope for most mean shapes. In section 4, the subtleties of calculating thermal fluctuations around non-trivial mean shapes subject to geometrical constraints are discussed. In particular, the fluctuations for 'quasi-spherical' vesicles, which are spherical in the mean, are addressed. This case is important from an experimental perspective since the flicker spectrum yields the bending rigidity, which is the basic material parameter of the fluid membrane.

Section 5 is devoted to the theory of vesicles of non-spherical topology. A variety of these shapes for genus 1 have been predicted independently from their experimental observation. In particular, the theory predicted the prominence of non-axisymmetric shapes. For genus 2 and higher, the shape of lowest energy was predicted to be one-fold continuously degenerate due to the conformal invariance of the curvature energy. Experimental evidence for this phenomenon was found soon after.

Section 6 deals with a vesicle adhering to a substrate. This configuration has fundamental relevance since very often vesicles and membranes are not isolated but rather interact with each other through a variety of forces. We focus on the shape change induced by adhesion and discuss in particular unbinding transitions caused either by the competition between curvature and adhesion or by the interplay between entropic repulsion and attractive interactions.

Section 7 is devoted to the dynamics of fluid membranes. Since the embedding of the membrane into the fluid is crucial to all dissipative processes, the full hydrodynamics of the coupled system comprising both the membrane and the embedding liquid has to be treated. For general configurations, this can become quite involved. We focus on the paradigmatic situation of an almost planar membrane and examine in particular the role of the coupling between the two monolayers on the damping of membrane fluctuations. The discussion of the dynamics of a bound membrane is motivated by a promising recent experimental development. As an example of a non-equilibrium shape transformation we discuss the pearling instability of cylindrical membranes induced by a laser tweezer.

Section 8 gives a quite subjective selection of more complex membrane systems where interesting new effects arise from the coupling between internal degrees of freedom and the external geometry.

I have attempted to achieve a pedagogical, self-contained, systematic presentation rather than following the chronological development. Such an approach risks not giving proper reference to earlier or alternative work for which I apologize to the respective authors in advance.

An emphasis on other aspects of the physics of membranes can be found *inter alia* in reviews (Lipowsky 1991, Bloom *et al.* 1991, Wortis *et al.* 1993, Michalet *et al.* 1994b, Sackmann 1994, Gompper and Schick 1994, Menger and Gabrielson 1995), collections (Meunier *et al.* 1987, Nelson *et al.* 1989, Lipowsky *et al.* 1992, Beysens *et al.* 1991), at least three textbooks (Israelachvili 1991, Safran 1994, Evans and Wennerström 1994) and a two-volume handbook containing nineteen review articles (Lipowsky and Sackmann 1995).

### 1.3. Chemistry and thermodynamics

Any theoretical treatment has to be aware of a few basic properties of the membrane resulting from its molecular architecture. The bilayers discussed in this work are formed by so-called lipids, which constitute a particular class of amphiphilic molecules. Lipids consist of a polar or negatively charged head group, which is highly soluble in water, and a hydrophobic part, which consists of two hydrocarbon chains (Cevc and Marsh 1987). The various bilayer-forming lipids differ in the length of the hydrocarbon chains, the number of unsaturated bonds within a chain, the chemistry of the head group and of the backbone connecting chains and head (Marsh 1990). For the mesoscopic configuration studied in this work, the molecular details are believed to be largely irrelevant, in the sense that they can be subsumed into effective elastic constants of the continuum theory described below.

Phase diagrams for the binary system that consists of lipid and water have been studied experimentally with a variety of techniques such as X-ray diffraction, electron microscopy, differential scanning calorimetry and NMR spectroscopy (Marsh 1990). Quite generally, these phase diagrams are governed by the amphiphilic nature of the lipid molecule, which tries to avoid contact of the chain region with water. Bilayer formation as one way to achieve this depends crucially on the molecular geometry of the amphiphile (Israelachvili 1991). If the chain is too short, or the head is too bulky, the amphiphiles prefer to self aggregate into micelles, which are spherical (or cylindrical) conformations of a ‘monolayer’ with no water in the interior.

In figure 8, the phase diagram for dimyristoyl phosphatidylcholine (DMPC)/water is shown. In the large parts of the phase diagram, swollen bilayers are the stable phase. This lamellar phase is fluid at high temperature (the so-called  $L_\alpha$  phase) whereas at low temperature, the bilayers become a 2D gel ( $L_\beta'$ ). For DMPC, there is also an intervening ‘ripple phase’ with surface texture ( $P_\beta'$ ). At very low water content, liquid crystalline phases form which may be cubic or hexagonal. The  $L_\alpha$  phase can take up only a certain amount of water. Adding more water leads to phase coexistence between the  $L_\alpha$  phase and excess water.

Vesicles as they will be studied here belong to this excess water phase since typically only a very small amount of lipid is swollen with water. The thermodynamic properties of this excess water phase are not yet well characterized since topological equilibration requires too long a time for it to be experimentally accessible. One would expect that this phase is characterized by an equilibrium

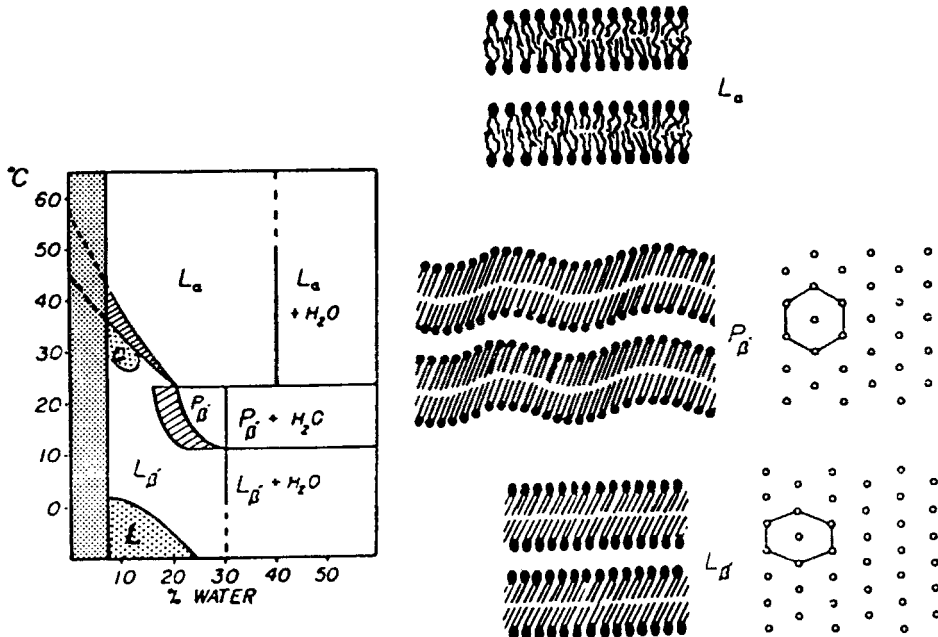


Figure 8. Phase diagram of DMPC/water. L<sub>α</sub>, L<sub>β'</sub> and P<sub>β'</sub> denote the fluid lamellar, the gel and the ripple phase, respectively (Janiak *et al.* 1979).

distribution of vesicles of different sizes and topologies (Helfrich 1986, Morse and Milner 1994, 1995).

An even richer phase behaviour has been found for tensides, which are single-chain amphiphiles, in water at high dilution. Such a system exhibits several vesicular phases and also a random bicontinuous phase, the so-called sponge phase, which have been identified experimentally (Hoffmann *et al.* 1992) in agreement with theoretical predictions (Roux *et al.* 1992, Porte 1992). The larger stiffness of phospholipid bilayers, however, may prevent the formation of some of these phases, such as the sponge phase, by pre-empting the theoretically expected second-order transition to this phase with a strong first order transition (Helfrich 1994).

As interesting as the issue of the global phase diagram may be, the problem of thermal equilibrium on very long time scales is fortunately mostly irrelevant as long as one focuses on a particular vesicle as seen through the microscope. Our ‘observables’ will be quantities referring to this particular vesicle and not quantities characterizing a whole ensemble of vesicles. In this sense, the often-made statement that ‘vesicles are only metastable’ is somewhat misleading since it precludes the fact that on experimentally relevant time scales (up to at least an hour) a vesicle can be considered as a system in a well-defined constrained equilibrium. The constraints characteristic for this equilibrium arise from physical properties of the bilayer as follows.

First, due to the strong hydrophobic effect, the concentration of ‘free’ lipid molecules in aqueous solution is tiny, with a typical value of the order of 1–100 molecules  $\mu\text{m}^{-3}$  (Marsh 1990). Consequently, the number of lipid molecules within the bilayer is constant for a vesicle. This fact implies that the area of a vesicle is also constant at constant temperature since it can adjust to its optimal value. Moreover,

even the number of molecules within each layer is practically constant since interchange of lipid molecules from one monolayer to the other is slow due to the large activation barrier for dragging a polar head group through the hydrocarbon chain region. Measurements of this flip-flop rate are somewhat controversial due to the various measurement techniques, but there is consensus that for phospholipids this time scale is of the order of hours (Homan and Pownall 1988). However, there are amphiphilic molecules that can be present as solutes in the bilayer, such as the biologically ubiquitous cholesterol, that are known to flip much faster between the layers (Backer and Dawidowicz 1981).

Even though membranes are permeable to water, the enclosed volume of a vesicle is typically a constrained variable, too. The reason lies in the presence of molecules to which the membrane is impermeable such as sugar molecules or large ions, that are either deliberately added to the aqueous solution, or are inevitably present in low concentration due to impurities. In either case, any net transfer of water would generate an osmotic pressure that cannot be counterbalanced by the relatively weak forces arising from additional bending of the membrane, as will be quantified in section 2.4 below. Thus, the enclosed volume of a vesicle is controlled by the condition that basically no osmotic pressure builds up (Helfrich 1973).

## 2. Curvature models

In this section, we motivate, in three steps, the energy for any specific vesicle shape. First, the concept of local curvature energy in the classical model (section 2.1) is discussed and its basic consequences are recalled (section 2.2). Then, the refinement arising from the bilayer nature of the membrane is introduced (section 2.3) and finally non-trivial effects arising from the closure of an open bilayer sheet to a vesicle is taken into account (section 2.4). Since our treatment does not quite follow the chronology, a brief history of the various variants of the curvature models that appear in the literature is presented in section 2.5 to give credit to previous work.

### 2.1. Local curvature energy in the classical model

Three or four orders of magnitude separate the thickness of the bilayer, which is about four nanometres, from the overall size of vesicles which are observable through the microscope. This separation of length scales suggests a description of the membrane as a 2D surface  $\mathbf{R}(s_1, s_2)$  embedded in 3D space. Here,  $s_1$  and  $s_2$  denote (arbitrary) internal coordinates. Such a surface can locally be characterized by its two radii of curvature  $R_1$  and  $R_2$ , as shown in figure 9. From the radii of curvature, both the mean curvature

$$H \equiv (1/R_1 + 1/R_2)/2 \quad (2.1)$$

and the Gaussian curvature

$$K \equiv 1/(R_1 R_2) \quad (2.2)$$

can be derived.

For a mathematical definition of these quantities (see, for example, do Carmo (1976)), one first introduces the tangential vectors

$$\mathbf{R}_i \equiv \partial_i \mathbf{R}(s_1, s_2) \quad \text{for } i = s_1, s_2, \quad (2.3)$$

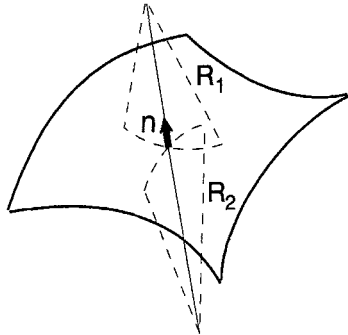


Figure 9. Curvature on a 2D surface. The length scales  $R_1$  and  $R_2$  denote the radii of curvature. The vector  $\mathbf{n}$  denotes the normal.

from which one obtains the metric tensor

$$g_{ij} \equiv \mathbf{R}_i \cdot \mathbf{R}_j. \quad (2.4)$$

Its determinant,  $g \equiv \det(g_{ij})$ , yields the area element

$$dA = \sqrt{g} \, ds_1 \, ds_2. \quad (2.5)$$

The normal vector  $\mathbf{n}(s_1, s_2)$  is given by

$$\mathbf{n} = \frac{\mathbf{R}_1 \times \mathbf{R}_2}{|\mathbf{R}_1 \times \mathbf{R}_2|}. \quad (2.6)$$

Finally, the mean and the Gaussian curvature follow from the curvature tensor

$$h_{ij} \equiv (\partial_i \partial_j \mathbf{R}) \cdot \mathbf{n} \quad (2.7)$$

according to

$$H \equiv -\frac{1}{2} \operatorname{tr} h_j^i \quad (2.8)$$

and

$$K \equiv \det(h_j^i), \quad (2.9)$$

where  $h_j^i \equiv g^{ik} h_{kj}$  and  $g^{ij}$  are the matrix elements of the (matrix) inverse of  $(g_{ij})$ . The minus sign in (2.8) ensures a positive mean curvature for the sphere with the usual spherical coordinates ( $s_1 = \theta, s_2 = \phi$ ), contrary to the convention used in differential geometry. Comparison of (2.1) and (2.2) with (2.8) and (2.9) shows that the radii of curvature are the negative inverse eigenvalues of the curvature tensor.

In the classical curvature model for symmetric membranes, the local bending energy  $f_0$  of a non-flat membrane is written as an expansion in the curvature. To lowest order, one obtains (Canham 1970, Helfrich 1973)

$$f_0 \equiv (\kappa/2)(2H)^2 + \kappa_G K. \quad (2.10)$$

The two elastic constants  $\kappa$  and  $\kappa_G$  both have the dimension of an energy. They are called bending rigidity and Gaussian bending rigidity, respectively.

A constant term in the energy density (2.10) which would correspond to a ‘surface tension’ or chemical potential for area has to be omitted. The fixed number of molecules in the membrane ensures a fixed internal area because stretching or compressing the membrane involves much larger energies than the cost of bending deformations. The absence of a surface tension in the ordinary sense distinguishes bilayer membranes fundamentally from liquid interfaces or even Langmuir monolayers, where interfacial area can be created or destroyed at a cost that is given by the surface tension. For an interface, the ‘interfacial’ particles are the same as the bulk particles whereas a membrane consists of a fixed number of ‘particles’ each of which can assume its preferred area in the conformations studied here. The more subtle notion of an effective tension generated by thermal fluctuations in the presence of constraints will be discussed in section 4 below.

## 2.2. Almost planar membrane and persistence length

Before we consider vesicles, it is instructive to recall some basic properties of the curvature energy for almost planar membranes. We use a Monge representation for the displacements  $h(\mathbf{x})$  of the membrane which is oriented in the  $z = 0$  plane, with  $\mathbf{x} = (x, y)$ . The mean curvature is then given as (do Carmo 1976)

$$2H = -\frac{\nabla^2 h + (\partial_x h)^2 \partial_y^2 h + (\partial_y h)^2 \partial_x^2 h - 2\partial_x h \partial_y h \partial_x \partial_y h}{[1 + (\nabla h)^2]^{3/2}} = -\nabla^2 h \{1 + O[(\nabla h)^2]\}. \quad (2.11)$$

As will be discussed below, the Gaussian curvature is a total divergence and need not be considered here. Introducing a Fourier representation

$$h(\mathbf{x}) \equiv \int \frac{d^2 q}{(2\pi)^2} h_{\mathbf{q}} \exp(i\mathbf{q}\mathbf{x}), \quad (2.12)$$

the bending energy is given by

$$F_0 \equiv \int dx dy \sqrt{g} f_0(x, y) \approx \frac{\kappa}{2} \int \frac{d^2 q}{(2\pi)^2} q^4 h_{\mathbf{q}} h_{\mathbf{q}}^* \equiv \frac{1}{2} \int \frac{d^2 q}{(2\pi)^2} E_0(q) h_{\mathbf{q}} h_{\mathbf{q}}^* \quad (2.13)$$

to lowest order, where  $*$  denotes the complex conjugate. Here, we have defined the ‘energy’

$$E_0(q) \equiv \kappa q^4 \quad (2.14)$$

of a bending mode.

The static correlation functions can easily be obtained from (2.13) as

$$\langle h_{\mathbf{q}} h_{\mathbf{q}'}^* \rangle = \frac{T}{E_0(q)} (2\pi)^2 \delta(\mathbf{q} - \mathbf{q}') = \frac{T}{\kappa q^4} (2\pi)^2 \delta(\mathbf{q} - \mathbf{q}'), \quad (2.15)$$

where  $\langle \dots \rangle$  is the thermal expectation value taken with the Boltzmann weight,  $\exp(-F_0/T)$ . Boltzmann's constant is set to unity throughout the article.

It is consistent to neglect the higher-order terms in the expansion (2.13) as long as the expectation value  $\langle (\nabla h)^2 \rangle$  is small compared to 1. Using the correlation function (2.15), one finds

$$\langle (\nabla h)^2 \rangle = \int \frac{d^2 q}{(2\pi)^2} \int \frac{d^2 q'}{(2\pi)^2} \mathbf{q} \mathbf{q}' \langle h_{\mathbf{q}} h_{\mathbf{q}'}^* \rangle = \frac{T}{2\pi\kappa} \int_{1/L}^{1/a} dq/q = \frac{T}{2\pi\kappa} \ln(L/a). \quad (2.16)$$

Here,  $L$  is the linear extension of the membrane and  $a$  is a molecular cut-off of the order of nanometres. Thus, the notion of an almost planar membrane is meaningful only if  $L \ll L_p$  where the *persistence length* (de Gennes and Taupin 1982)

$$L_p \equiv a \exp(2\pi\kappa/T) \quad (2.17)$$

is also the correlation length for the normals.

If higher-order terms occurring in the expansion (2.13) are treated perturbatively, the result can be formulated as a length-dependent bending rigidity

$$\kappa(L) = \kappa - (c/4\pi)T \ln(L/a), \quad (2.18)$$

where  $L$  is the length scale on which the membrane is bent. There has been some controversy about the correct value of the factor  $c$ . Depending on the measure used to integrate out the fluctuations,  $c = 1$  has been found for the 'curvature measure' (Helfrich 1985, 1986, 1987) and  $c = 3$  for the 'displacement measure' (Peliti and Leibler 1985, Förster 1986, Kleinert 1986). The latter value has recently been confirmed by Monte Carlo simulations (Gompper and Kroll 1994). A real-space renormalization group scheme yields  $c \approx 1.4$  and an exponential dependence of the bending rigidity on length-scales beyond the persistence length (Mecke 1995). Beyond the scale  $L_p$ , membrane configurations are characterized by irregular shapes for which self-avoidance becomes crucial.

For phospholipid membranes as studied here, the bending rigidity can be obtained by different techniques discussed in Appendix A. The typical range of values  $\kappa \approx (10 - 25)T$  leads to an astronomical persistence length  $L_p \approx a \exp(60 - 150)$ . This result shows that the concept of a mean orientation of the membrane makes sense for these bilayers. A much smaller persistence length applies if so-called bola-lipids are added to the membrane (Duwe *et al.* 1990). The corresponding vesicles have shown strong fluctuations. However, a naive application of the results developed here to this system is dangerous for two reasons. First, bola lipids are soluble in substantial fraction so that the concept of a vanishing surface tension may break down. Secondly, the local composition in mixed membranes can couple to the shape, which leads to spatial inhomogeneities as will be discussed in section 8.1.

### 2.3. Coupling between curvature and density

Further analysis of the energy density (2.10) as described in section 3.4 below shows that it cannot explain typical phenomena observed in shape transformations of vesicles such as the budding transition. The reason for this failure is its lack of any signature of the bilayer architecture. In fact, the energy (2.10) would be appropriate for a symmetric lipid monolayer for which so far no physical realization is known.

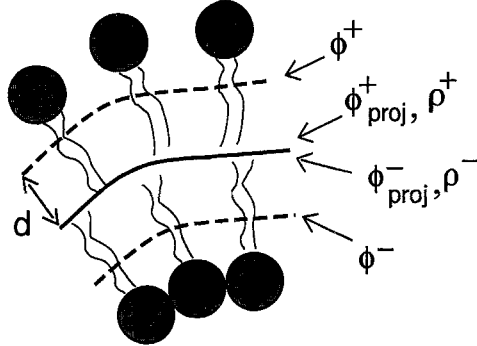


Figure 10. Cartoon of a *bilayer* membrane. The densities  $\phi^\pm$  are defined on the neutral surfaces of the two monolayers shown as dashed curves. The projected densities  $\phi_{\text{proj}}^\pm$  and the scaled quantities  $\rho^\pm$  are defined on the bilayer mid-plane (bold curve).

The bilayer aspect can easily be incorporated by ‘decorating’ each side of the mathematical surface  $\mathbf{R}(s_1, s_2)$  with a fluid of lipids as shown in figure 10. Such a 2D fluid can be characterized by its number densities  $\phi^\pm(s_1, s_2)$ . Deviations from the equilibrium density  $\phi_0$  cost an energy

$$f_1^\pm \equiv (k^m/2)(\phi^\pm/\phi_0 - 1)^2, \quad (2.19)$$

to lowest order in  $\phi^\pm/\phi_0 - 1$ . Here,  $k^m$  can be interpreted as the elastic compression modulus for the 2D fluid within each monolayer. This elasticity acts in the so-called neutral surface of each monolayer. The neutral surface is defined by the property that bending and stretching are decoupled in energy when both deformations are defined with respect to it. The neutral surface of each monolayer is at a distance  $d$  from the bilayer mid-plane.

It will be very convenient to have all physical quantities defined on the bilayer midplane. Therefore, we project the densities  $\phi^\pm$  onto this surface. If the membrane is curved, the projected densities  $\phi_{\text{proj}}^\pm$  deviate from the densities  $\phi^\pm$ . To lowest order in  $dH$ , the relation between both densities is given by

$$\phi^\pm = \phi_{\text{proj}}^\pm(1 \mp 2dH + O(d^2K)). \quad (2.20)$$

For small curvature, the elastic energy,  $f_1^\pm$ , can thus be written as

$$f_1^\pm = (k^m/2)(\rho^\pm \mp 2dH)^2, \quad (2.21)$$

where we introduce the reduced density deviations

$$\rho^\pm \equiv (\phi_{\text{proj}}^\pm/\phi_0 - 1). \quad (2.22)$$

The total energy of a symmetric bilayer membrane is thus given by (Seifert and Langer 1993)

$$f \equiv f_0 + f_1^+ + f_1^- = \frac{\kappa}{2}(2H)^2 + \kappa_G K + \frac{k^m}{2} [(\rho^+ - 2dH)^2 + (\rho^- + 2dH)^2]. \quad (2.23)$$

We have retained the bending part of the classical model. Physically, it signifies the energy stored in the bending of each individual monolayer even if the lateral densities are adjusted to the shape in such a way that the contributions  $f_1^\pm$  vanish.

The coupling between the local shape and the densities becomes more evident if we introduce the reduced density difference

$$\rho \equiv (\rho^+ - \rho^-)/2, \quad (2.24)$$

and the deviation

$$\bar{\rho} \equiv (\rho^+ + \rho^-)/2 \quad (2.25)$$

of the mean density from its equilibrium value. Using these quantities, the energy (2.23) can be written as

$$f = \frac{\kappa}{2}(2H)^2 + \kappa_G K + k^m [\bar{\rho}^2 + (\rho - 2dH)^2]. \quad (2.26)$$

Disregarding the phenomenological ‘derivation’ of the energy (2.23) or (2.26) given here, one could also have postulated this form as following from two principles. First, the relevant ‘degrees of freedom’ are identified, which are the ‘shape’ and the two densities of the two monolayer liquids. Then, the energy is expanded in the lowest-order terms in these variables taking into account the obvious symmetry requirements of a symmetric bilayer. The slight advantage of our presentation is the identification of the ‘coupling constant’ between  $\rho$  and  $H$  as given by the material parameters  $k^m d$ . Along the same lines, it should be clear that there will be all sorts of higher-order terms which are compatible with the symmetry of the membrane. For instance, we have not treated any explicit interaction between the two layers but rather postulated a fixed distance  $d$ . On a more microscopic level, one could expect that the local distance or thickness of the membrane depends on its local lateral density. Thus, one could introduce a field for the deviations from the mean thickness  $d$  which, however, would not couple to the shape  $H$  nor to  $\rho$  in quadratic order by symmetry.

For a discussion of small displacements about the almost planar shape for the bilayer energy, the reduced densities are expanded as

$$\rho^\pm(\mathbf{x}) \equiv \int \frac{d^2 q}{(2\pi)^2} (\bar{\rho}_q \pm \rho_q) \exp(iq\mathbf{x}). \quad (2.27)$$

The total energy of a bilayer membrane, thus, becomes

$$F \equiv \int \frac{d^2 q}{(2\pi)^2} f_q \equiv \frac{1}{2} \int \frac{d^2 q}{(2\pi)^2} (h_q, \rho_q, \bar{\rho}_q) \mathbf{E}(q) \begin{pmatrix} h_q \\ \rho_q \\ \bar{\rho}_q \end{pmatrix}^*, \quad (2.28)$$

with the ‘energy’ matrix

$$\mathbf{E}(q) \equiv \begin{pmatrix} \tilde{\kappa}q^4 & -2k^m dq^2 & 0 \\ -2k^m dq^2 & 2k^m & 0 \\ 0 & 0 & 2k \end{pmatrix}, \quad (2.29)$$

where the renormalized bending rigidity  $\tilde{\kappa}$  is defined by

$$\tilde{\kappa} \equiv \kappa + 2d^2 k^m. \quad (2.30)$$

Minimizing the single mode energy  $f_q$  in (2.) with respect to  $\rho_q$  leads to

$$\rho_q^{\min}(h_q) = dq^2 h_q. \quad (2.31)$$

Using this relation in (2.28), we recover the energy of the classical model:

$$f_q(h_q, \rho_q^{\min}, \bar{\rho}_q = 0) = \frac{\kappa}{2} q^4 h_q h_q^*. \quad (2.32)$$

This shows that the classical model implicitly assumes that the densities in each monolayer adjust optimally to the local shape, i.e., in the classical model bending takes place at a relaxed lateral density within each monolayer.

For bending at ‘frozen’ density  $\rho^\pm = 0$ , we get

$$f_q(h_q, \rho_q = 0, \bar{\rho}_q = 0) = \frac{\tilde{\kappa}}{2} q^4 h_q h_q^*. \quad (2.33)$$

Whether the difference between bending at relaxed and bending at frozen densities is significant depends on the relative magnitude of  $\kappa$  and  $\tilde{\kappa}$ . For a simple estimate, we assume that each monolayer is a homogeneous thin plate of thickness  $2d$ . For such a plate, the bending rigidity  $\kappa^m$  (with a superscript for ‘monolayer’ ) and the area compression modulus  $k^m$  are related by (Landau and Lifshitz 1989)

$$\kappa^m = k^m d^2 / 3. \quad (2.34)$$

With the bending rigidity of the bilayer  $\kappa = 2\kappa^m$  and (2.30), we find  $\tilde{\kappa} = 4\kappa$ . This significant difference shows that lateral relaxation is an important factor in bending deformations (Evans 1974, Helfrich 1974a). Two effects can impede this lateral relaxation. First, lateral relaxation is effective only if the time scale associated with this relaxation is faster than a typical time-scale for the bending relaxation. This issue will be addressed in Section 7 below. Secondly, lateral relaxation implicitly assumes a reservoir of lipid molecules at the boundaries. For closed membranes such a reservoir is not available, leading to consequences discussed in the next subsection.

We close this subsection by quoting the static correlation functions which follow from (2.28)

$$\begin{aligned} \left\langle \begin{pmatrix} h_q \\ \rho_q \\ \bar{\rho}_q \end{pmatrix} (h_{q'}, \rho_{q'}, \bar{\rho}_{q'})^* \right\rangle &= T \mathbf{E}^{-1}(q) (2\pi)^2 \delta(\mathbf{q} - \mathbf{q}') \\ &= T \begin{pmatrix} 1/\kappa q^4 & dq^2/\kappa & 0 \\ dq^2/\kappa & \tilde{\kappa}/2k^m \kappa & 0 \\ 0 & 0 & 1/2k^m \end{pmatrix} (2\pi)^2 \delta(\mathbf{q} - \mathbf{q'}). \end{aligned} \quad (2.35)$$

#### 2.4. Global energy of a vesicle shape

The energy of a closed membrane configuration follows from integrating the energy density (2.26) over the closed vesicle surface. This leads to the total energy of a vesicle,

$$F = \frac{\kappa}{2} \oint dA (2H)^2 + \kappa_G \oint dA K + k^m \oint dA (\rho - 2dH)^2 + k^m \oint dA \bar{\rho}^2 + F_V \quad (2.36)$$

as a sum of five contributions which we now discuss in detail.

##### 2.4.1. Gauss–Bonnet-theorem

The second integral in the energy (2.36) does not depend on the specific shape of the vesicle. Due to the Gauss–Bonnet theorem (see, for example, do Carmo (1976)), this term is the topological invariant  $\kappa_G 4\pi(1 - g)$ , where  $g$  is the genus, i.e. the number of handles, of the vesicle. For any fixed topology, this energy can be neglected. We will proceed to do so by formally setting  $\kappa_G = 0$ .

##### 2.4.2. Osmotic pressure

The last term,  $F_V$ , in the energy (2.36) arises from the presence of molecules in the solution, such as large ions or sugar molecules, to which the membrane is impermeable on the time scales considered here. With  $c$  as the total concentration in moles per unit volume of these osmotically active molecules, there arises an osmotic pressure

$$\Pi \equiv R_g T(n/V - c), \quad (2.37)$$

where  $R_g \simeq 8.31 \text{ J (mol K}^{-1}\text{)}$  is the gas constant,  $V$  is the volume of the vesicle and  $n$  is the total number of moles of these molecules caught within the vesicle. For simplicity, an ideal solution was assumed. Such an osmotic pressure leads to the energy

$$F_V(V) \equiv \int_{V_0}^V dV' \Pi(V') = R_g T[n \ln(V/V_0) - c(V - V_0)] \approx \frac{R_g T c V_0}{2} \left( \frac{V}{V_0} - 1 \right)^2. \quad (2.38)$$

The latter approximation holds for small  $V/V_0 - 1$ , where

$$V_0 \equiv n/c \quad (2.39)$$

is the volume for which the osmotic pressure vanishes.

##### 2.4.3. Minimizing with respect to lipid densities

First, the energy  $F$  is minimized with respect to the density variables  $\rho$  and  $\bar{\rho}$ , taking into account that the number  $N^+$  and  $N^-$  of lipid molecules within each layer is conserved. Using

$$N^\pm = \oint dA \phi_{\text{proj}}^\pm \quad (2.40)$$

and the definitions (2.22),(2.24) and (2.25), this conservation implies the integral constraints

$$\int dA \bar{\rho} = \int dA [(\phi_{\text{proj}}^+ + \phi_{\text{proj}}^-)/\phi_0 - 1] = (N^+ + N^-)/(2\phi_0) - A, \quad (2.41)$$

where  $A$  is the total area of the vesicle and

$$\int dA \rho = \frac{1}{2} \int dA (\phi_{\text{proj}}^+ - \phi_{\text{proj}}^-)/\phi_0 = (N^+ - N^-)/(2\phi_0). \quad (2.42)$$

If these constraints are added with Lagrange multipliers to the energy  $F$ , minimization at fixed shape (and, thus, at fixed area  $A$ ) immediately leads to a constant mean density given by

$$\bar{\rho} = (N^+ + N^-)/(2\phi_0 A) - 1. \quad (2.43)$$

For the local density difference, minimization shows that the density difference follows the local mean curvature according to

$$\rho(s_1, s_2) - 2dH(s_1, s_2) = -2dM/A + (N^+ - N^-)/(2\phi_0 A), \quad (2.44)$$

where

$$M \equiv \oint dA H \quad (2.45)$$

is the total (integrated) mean curvature. The geometrical quantity  $M$  also determines the actual area difference

$$\Delta A = 4dM + O(d^2) \quad (2.46)$$

between the neutral surfaces of the two monolayers which will, in general, differ from the optimal area difference

$$\Delta A_0 \equiv (N^+ - N^-)/\phi_0, \quad (2.47)$$

which is determined by the number of molecules in each layer.

If the expressions (2.44) and (2.43) for the density variables are inserted into the energy (2.36), one obtains an energy

$$\begin{aligned} F \equiv & (\kappa/2) \oint dA (2H)^2 + \frac{k^m}{4A} (\Delta A - \Delta A_0)^2 \\ & + k^m A [(N^+ + N^-)/(2\phi_0 A) - 1]^2 + \frac{R_g T c V_0}{2} \left( \frac{V}{V_0} - 1 \right)^2. \end{aligned} \quad (2.48)$$

#### 2.4.4. Effective constraint on area and volume

A convenient simplification arises from the fact that there are two well-separated energy scales present in the four terms of the energy (2.48). The first and the second terms both are, as shown below, of the order  $\kappa$ . The third term depends strongly on the total area of the vesicle. For a large vesicle with  $A = 1000 \mu\text{m}^2$ , and the typical

material constants  $k = 10^2$  erg cm $^{-2}$ , and  $\kappa = 10^{12}$  erg (Evans and Needham 1987), the energy scale of this term,  $k^m A \simeq 10^9 \kappa$  vastly exceeds the energy of the curvature elasticity. Thus, one can determine the area  $A$  by the requirement that the third term vanishes. This leads to the area constraint

$$A = (N^+ + N^-)/(2\phi_0) \equiv 4\pi R_0^2, \quad (2.49)$$

given by the mean number of lipid molecules in the two layers. For later reference, we define here an equivalent sphere radius  $R_0$ .

Likewise, the energy scale involving osmotic differences,  $RTcV_0/2 \simeq 10^3 \kappa$ , for the typical values  $R_0 = 10$  μm and  $c = 10^{-4}$  mol m $^{-3}$  as a typical sugar concentration, shows that only minute concentration differences between interior and exterior solution of the order of  $10^{-7}$  mol m $^{-3}$  can be balanced by the curvature energy. To an excellent approximation, the volume is thus constrained to the value  $V_0 = n/c$  for which the osmotic pressure vanishes (Helfrich 1973). Any change in the ambient osmotic conditions will lead to an adaption of the vesicle volume such that the resulting osmotic pressure difference effectively vanishes again.

From a theoretical point of view, one could easily proceed without making these two simplifications even though they are convenient and well justified for giant vesicles. In fact, the theory as developed in the next section also captures the more general case where volume and area are subject to the energy terms present in (2.48).

#### 2.4.5. Area-difference-elasticity model

If the terms in the second line of the energy (2.48) are thus replaced by hard constraints on the area and volume, one obtains the so-called area-difference-elasticity (ADE) model in which the energy of a vesicle is given by (Seifert *et al.* 1992, Wiese *et al.* 1992, Bozic *et al.* 1992, Miao *et al.* 1994)

$$W \equiv \kappa \left[ G + \frac{\alpha\pi}{8Ad^2} (\Delta A - \Delta A_0)^2 \right], \quad (2.50)$$

with the dimensionless ‘local’ bending energy

$$G \equiv (1/2) \oint dA (2H)^2 \quad (2.51)$$

and the dimensionless material parameter

$$\alpha \equiv 2k^m d^2 / (\pi\kappa). \quad (2.52)$$

The second term in (2.50) is the so-called area-difference elasticity or non-local curvature energy. In the form  $\alpha\kappa$ , the elastic constant in front of this term is sometimes called the non-local bending rigidity. If one assumes that the monolayers are homogeneous sheets of thickness  $2d$ , one obtains with (2.34) the estimate  $\alpha = 3/\pi \simeq 1$ . However, it may be advisable to leave the value of  $\alpha$  open and treat it as an independent material parameter because the ADE model may be applicable even if a simple relation like (2.34) breaks down due to the internal structure of the monolayer. Corrections to the energy (2.50) can be expected to be of the order of

$d/R_0$ , which is the basic expansion parameter of these curvature models for symmetric membranes.

### 2.5. A brief history of variants of the curvature model

The derivation of the ADE model given above reflects an evolution of curvature models dating to their first appearance in the early seventies. All these models can be cast in a form amounting to special cases of a generalized ADE model.

In this section, we introduce these variants roughly according to their historical occurrence partly in order to assign credit for the essential steps. Considerable parts of the literature still deal with these variants, especially since they contain typically one less parameter than the ADE model. We will also have to specialize to these limiting cases sometimes in later sections.

#### 2.5.1. Minimal model: local curvature energy only

The first description of fluid membranes by a curvature model was given by Canham (1970), in which the local energy density of the form  $\sim(1/R_1^2 + 1/R_2^2) = (2H)^2 - 2K$  was introduced. Since the Gaussian term is irrelevant for all but topological transformations, this model amounts to retaining just the local curvature energy from (2.50). For later reference, we define the energy of this ‘minimal model’ as

$$F_M \equiv \kappa G. \quad (2.53)$$

From the present perspective, this energy is a faithful description of a vesicle which consists of a symmetric bilayer with rapid flip-flop of the lipid molecules. While it is known that cholesterol flips quite rapidly between the two layers (Backer and Dawidowicz 1981), pure cholesterol does not form bilayers. For vesicles consisting of mixtures, however, the presence of two components leads to an additional degree of freedom which has to be taken into account as discussed in section 8. Likewise, lipid molecules with two polar head groups connected by hydrocarbon chains such as the bola lipids (Marsh 1990) would constitute a model system for this minimal model. Again, these molecules can be added to a lipid bilayer but they are not able to form bilayers as a single component system. Thus, there is not yet a genuine physical realization of this ‘minimal model’.

#### 2.5.2. Spontaneous curvature model

Helfrich (1973) in a seminal paper introduced the energy

$$F_{SC} \equiv \frac{\kappa}{2} \oint dA (2H - C_0)^2 + \kappa_G \oint dA K, \quad (2.54)$$

where the so-called spontaneous curvature  $C_0$  is supposed to reflect a possible asymmetry in the membrane. The energy (2.54) together with constraints on the total area and the enclosed volume defines the spontaneous-curvature (SC) model. The physical origin of the spontaneous curvature could be either a different chemical environment on both sides of the membrane, or a different chemical composition of the two monolayers. In the latter case, however, the fluidity of the lipids will lead to a lateral adjustment of the local composition to the local curvature, i.e. to the local shape, as we will discuss in section 8. The spontaneous curvature then becomes a dynamical variable and is no longer constant over the vesicle surface. Indeed, the

spontaneous curvature has remained elusive since there seem to be no measurements of this quantity for phospholipid vesicles. Fischer (1993) has recently suggested an alternative formulation of the spontaneous curvature model.

### 2.5.3. Bilayer couple model

In a complementary approach, building on earlier work (Sheetz and Singer 1974, Evans 1974, 1980), Svetina and Zeks introduced the so-called bilayer couple (BC) model, in which a hard constraint on the area difference  $\Delta A$ , i.e.  $\alpha = \infty$ , is imposed (Svetina *et al.* 1982, Svetina and Zeks 1983, 1989). Thus, this model is defined by the energy (2.53) together with the three constraints on area, volume and total mean curvature. In view of the derivation given above for the ADE model, the bilayer couple model can be rationalized by assuming the monolayers as incompressible but still bendable. Any spontaneous curvature is irrelevant in the BC model since it would add only a constant term to the energy at constant  $\Delta A$  (Seifert *et al.* 1991).

### 2.5.4. Area-difference-elasticity model

The physical effect of the area-difference-elasticity has been appreciated early on (Evans 1974, 1980, Helfrich 1974a). The model as defined in (2.50) has been introduced independently by three groups (Seifert *et al.* 1992, Wiese *et al.* 1992, Bozic *et al.* 1992). The derivation as presented above is related to the one given in Miao *et al.* (1994).

### 2.5.5. Area-difference-elasticity model with spontaneous curvature

The ADE model can also be derived if the two monolayers are asymmetric in the first place (Miao *et al.* 1994). This leads to a systematic spontaneous curvature which amounts to replacing  $(2H)^2$  by  $(2H - C_0)^2$  in (2.50). However, at constant area  $A$  and optimal area-difference  $\Delta A_0$ , the latter model is equivalent to the ADE model without spontaneous curvature but with a renormalized area-difference  $\Delta A_0$  given by (Miao *et al.* 1994)

$$\Delta A_0 = \widehat{\Delta A_0} + 8C_0dR_0^2/\alpha. \quad (2.55)$$

Thus, within the ADE model the spontaneous curvature leads only to a trivial modification. Only for the limit  $\alpha \rightarrow 0$  must one include a spontaneous curvature in order to end up with the SC model. If the limit  $\alpha \rightarrow 0$  is taken in the energy (2.50), one recovers the minimal model (2.53).

### 2.5.6. Summary of curvature models

For later reference, the energy and the applicable constraints on the various models are summarized in table 1. It is useful to introduce scaled quantities as

Table 1. Variants of the curvature models.

Model	Energy without Gaussian part	Constraints
Minimal	$F_M \equiv \kappa G$	$A, V$
BC	$F_M \equiv \kappa G$	$A, V, M$
ADE	$W \equiv \kappa[G + (\alpha/2)(m - m_0)^2]$	$A, V$
SC	$F_{SC} \equiv \kappa(G - c_0m + 2\pi c_0^2)$	$A, V$
ADE-SC	$W_{SC} \equiv \kappa[G - c_0m + 2\pi c_0^2 + (\alpha/2)(m - m_0)^2]$	$A, V$

follows. The reduced mean curvature  $m$ , the reduced optimal area difference  $m_0$ , and the reduced spontaneous curvature  $c_0$  are defined by

$$m \equiv M/R_0, \quad m_0 \equiv \Delta A_0/(4dR_0), \quad \text{and} \quad c_0 \equiv C_0 R_0. \quad (2.56)$$

### 3. Shapes and shape transformations

Vesicles will acquire the shape at which their curvature energy subject to the appropriate constraints is minimal. This basic premise of the approach using curvature models assumes both that non-equilibrium effects such as convection and temperature gradients are small, and that the effect of thermal fluctuations on the shape can be neglected except at shape transitions. While the former assertion has to be taken care of by the experimentalist, the latter holds to a first approximation since the bending rigidity is still large compared to the thermal energy.

Three different approaches have been developed to find the shape of lowest energy for given parameters. These techniques are (i) solving Euler–Lagrange equations, (ii) using ‘trial’ shapes within a variational approach, and (iii) minimizing numerically the curvature energy on a triangulated surface. The latter two techniques will be discussed in section 3.2 below.

Most work has been done within the first approach. As described in section 3.1, solutions of the Euler–Lagrange equations yield the set of *stationary shapes* for which the first variation of the appropriate energy, subject to the applicable constraints, vanishes. The set of stationary shapes comprises both locally stable shapes and saddle points. Saddle points can be identified by a stability analysis which requires considerable numerical effort. However, stability with respect to axisymmetric deformations is easy to check by close inspection of the bifurcation diagram. We explain this method in section 3.3, where we introduce the crucial concept of a continuous and a discontinuous transition.

These transitions separate different regions in a phase diagram, which shows the shape of lowest energy (and sometimes also locally stable shapes of higher energy) for a given set of controlled variables such as the reduced volume and the area difference. Since both the energy and the relevant parameters depend on the specific variant of the curvature model, the phase diagrams and the character of a shape transformation differ between the various variants as well. These phase diagrams are presented in sections 3.4 through 3.7 for the most important variants of the curvature model.

For a comparison of the theoretical results with experimental findings, we discuss the notion of temperature trajectories in the phase diagram in section 3.8. In section 3.9, the budding transition will serve as an example to show how detailed a comparison is possible at the present stage. Other shape transformations are described in section 3.10. The dramatic shape changes under the action of optical tweezers are briefly reviewed in section 3.11.

#### 3.1. Stationary shapes

##### 3.1.1. General energy functional and equivalence of the ensembles

The set of stationary shapes is the same for all variants of the curvature energy (except the minimal model which contains only a subset). Consider the general variational free energy

$$\Phi[S] = \kappa G[S] + \Sigma A[S] + PV[S] + QM[S], \quad (3.1)$$

where the dimensionless local curvature energy  $G$  has been defined in equation (2.51) and  $[S]$  denotes symbolically the dependence on the shape  $S$ . The parameters  $\Sigma$ ,  $P$  and  $Q$  will be specified later. The stationarity condition for the functional  $\Phi[S]$  formally reads

$$\delta^1 \Phi[S] = \kappa \delta^1 G[S] + \Sigma \delta^1 A[S] + P \delta^1 V[S] + Q \delta^1 M[S] = 0, \quad (3.2)$$

where  $\delta^1$  denotes the first variation. The set of stationary shapes  $\mathcal{S}_\Phi$  contains all shapes which obey this equation as  $\Sigma$ ,  $P$  and  $Q$  are varied. In the BC model,  $\Sigma$ ,  $P$  and  $Q$  are Lagrange multipliers chosen such that the area  $A$ , the volume  $V$  and the integrated mean curvature  $M$  acquire the appropriate values. These Lagrange parameters fulfil the relations

$$\Sigma/\kappa = -\frac{\partial G}{\partial A|_{V,M}}, \quad P/\kappa = -\frac{\partial G}{\partial V|_{A,M}}, \quad \text{and} \quad Q/\kappa = -\frac{\partial G}{\partial M|_{A,V}}. \quad (3.3)$$

We now show that the set  $\mathcal{S}_\Phi$  contains as a subset the set of stationary shapes  $\mathcal{S}_B$  which belong to the energy  $B$  of the general form

$$B \equiv \kappa G + g(A, V, M), \quad (3.4)$$

where  $g(A, V, M)$  is an arbitrary function. Such an energy, for example, has been encountered during the derivation of the ADE model where the last three terms of the energy  $F$  in equation (2.48) are of this type. If there are constraints,  $g(A, V, M)$  has to include terms of the type  $\Sigma_B A$ ,  $P_B V$  and  $Q_B M$ , where, for example,  $\Sigma_B$  is the Lagrange multiplier for the area. The stationarity condition for the energy  $B$  is

$$\delta^1 B \equiv \kappa \delta^1 G + \frac{\partial g}{\partial A} \delta^1 A[S] + \frac{\partial g}{\partial V} \delta^1 V[S] + \frac{\partial g}{\partial M} \delta^1 M[S] = 0. \quad (3.5)$$

A comparison of (3.5) with (3.2) shows that any stationary shape of the energy  $B$  is also stationary for  $\Phi$  provided the parameters  $\Sigma$ ,  $P$  and  $Q$  are chosen according to

$$\Sigma = \frac{\partial g}{\partial A}, \quad P = \frac{\partial g}{\partial V}, \quad \text{and} \quad Q = \frac{\partial g}{\partial M}. \quad (3.6)$$

Note that the reverse is not quite true. Depending on the specific form of  $g$ , there may be values of  $\Sigma$ ,  $P$  and  $Q$  which are not accessible through (3.6). Specializing the energy  $B$  to the various variants of the curvature models discussed above, we collect the interpretation of the parameters  $\Sigma$ ,  $P$  and  $Q$  for the respective models in table 2. In all cases,  $P$  is the Lagrange multiplier that ensures the constraint on area. For historical reasons, we will often replace  $Q$  by  $-2\kappa C_0$  in the rest of this article.

Table 2. Parameters in the various models.

Model	$g(A, V, M) - PV$	$\Sigma$	$Q$
Minimal	$\Sigma_M A$	$\Sigma_M$	0
BC	$\Sigma A + QM$	$\Sigma$	$Q$
ADE	$\Sigma_{ADE} A + (\alpha/2)\kappa(M - M_0)^2/R_0^2$	$\Sigma_{ADE}$	$\alpha\kappa(M - M_0)$
SC	$\Sigma_{SC} A - \kappa C_0 M + \kappa C_0^2 A/2$	$\Sigma_{SC} + \kappa C_0^2/2$	$-2\kappa C_0$
ADE-SC	$\Sigma_{ADE-SC} A - \kappa C_0 M + \kappa C_0^2 A/2 + \alpha/2\kappa(M - M_0)^2/R_0^2$	$\Sigma_{ADE-SE} + \kappa C_0^2/2$	$-2\kappa C_0 + \alpha\kappa(M - M_0)$

### 3.1.2. Shape equation and scale invariance of the local curvature energy

The formal shape equation (3.2) corresponds to a partial differential equation for the shape. This equation can be derived by parametrizing small deviations around a stationary shape  $\mathbf{R}_0(s_1, s_2)$  by

$$\mathbf{R}(s_1, s_2) = \mathbf{R}_0(s_1, s_2) + \epsilon(s_1, s_2) \mathbf{n}(s_1, s_2), \quad (3.7)$$

where  $\mathbf{n}(s_1, s_2)$  is the local normal vector. The stationarity condition  $\delta\Phi/\delta\epsilon(s_1, s_2) = 0$  (3.2) then becomes

$$P + 2\Sigma H - 2\kappa[2H(H^2 - K) + C_0K - \Delta H] = 0. \quad (3.8)$$

In the original derivation of this general shape equation a different sign convention for  $H$  and a shift in the tension  $\Sigma$  compared to our definition was used (Ou-Yang and Helfrich 1989). In equation (3.8),

$$\Delta \equiv (1/\sqrt{g})\partial_i(g^{ij}\sqrt{g}\partial_j) \quad (3.9)$$

is the Laplace–Beltrami operator on the surface. For  $\kappa = 0$ , equation (3.8) corresponds to Laplace’s equation which describes the balance of pressure and surface tension for soap films. For finite bending rigidity, bending moments contribute to this force balance.

An important general statement about the solutions of the fourth-order partial differential equation (3.8) follows from the scale invariance of the local curvature energy  $G$ . This energy does not depend on the size of the vesicle but only on its shape. If  $\mathbf{R}_0(s)$  is a solution to (3.8), the rescaled shape  $\mathbf{R}_0(s) \rightarrow \mathbf{R}_0(s)/\lambda$ , with  $\lambda > 0$ , is also a solution provided  $\Sigma \rightarrow \lambda^2\Sigma$ ,  $P \rightarrow \lambda^3P$  and  $C_0 \rightarrow \lambda C_0$  are rescaled properly. Writing  $\lambda = 1 + \epsilon$ , one obtains from the stationarity condition (3.2), the homogeneity relation

$$2\Sigma A + 3PV + QM = 0. \quad (3.10)$$

Because of the scale invariance, it is sufficient to consider the solutions of the shape equation at fixed  $C_0$ , where the two possible signs for  $C_0$  as well as  $C_0 = 0$  have to be considered separately. The solutions to (3.8) then depend only on the two parameters  $\Sigma C_0^2$ , and  $PC_0^3$ . Since for any given value of these two parameters one will, in general, find a discrete set of solutions to (3.8), the set of all solutions to (3.8) is a 2D manifold with countable degeneracy if trivial rescalings are ignored. Rather

than characterizing these shapes by the values of  $\Sigma C_0^2$  and  $PC_0^3$ , we will use two geometrical quantities, the reduced volume

$$\nu \equiv \frac{V}{(4\pi/3)R_0^3} \leq 1, \quad (3.11)$$

(where equality holds for the sphere only) and the integrated mean curvature  $m > 0$  defined in equation (2.56).

### 3.1.3. Expansion around the sphere

The only known analytical solution of spherical topology of (3.8) is the sphere. Indeed, inserting a sphere with radius  $R_0$  into (3.8) shows that it is a solution whenever

$$PR_0 + 2\Sigma - \kappa C_0/R_0 = 0. \quad (3.12)$$

Some insight into the structure of the solutions to (3.8) can be gained by an expansion around the sphere. A slightly deformed sphere can be parametrized by spherical harmonics  $Y_{lm}(\theta, \phi)$  according to

$$R(\theta, \phi) = R_0 \left[ 1 + \sum_{l \geq 0, m} u_{l,m} Y_{lm}(\theta, \phi) \right], \quad (3.13)$$

where  $|m| \leq l$  and  $u_{l,-m} = (-1)^m u_{l,m}^*$ .

Whenever the second variation of  $\Phi$ ,

$$\delta^2 \Phi = (\kappa/2R_0^2) \sum_{l \geq 0, m} |u_{l,m}|^2 [l(l+1) - 2][l(l+1) - C_0 R_0 - PR_0^3/2\kappa], \quad (3.14)$$

vanishes around the sphere, stationary shapes bifurcate from it. Here, the stationarity (3.12) has been used to eliminate  $\Sigma$ . The second variation  $\delta^2 \Phi$  does not depend on  $m$  for symmetry and is identical to zero for the ( $l = 1$ ) modes which correspond to rigid translations of the sphere. With increasing  $P$ , the sphere thus becomes unstable with respect to deformations with index  $l$  at a critical pressure (Ou-Yang and Helfrich 1987, Peterson 1988)

$$P_c(l)R_0^3/\kappa \equiv 2l(l+1) - 2C_0 R_0. \quad (3.15)$$

However, all shapes which result from the sphere by a bifurcation labelled with  $l \geq 3$  are unstable with respect to an ( $l = 2$ ) deformation (Peterson 1989). According to this general result, only the ( $l = 2$ ) shapes are suitable candidates for local minima near the sphere.

### 3.1.4. Axisymmetric shapes

In order to investigate the evolution of the shapes which bifurcate from the sphere at the critical value  $P_c(l)$ , the fourth-order partial differential equation (3.8) has to be solved numerically. In full generality, this task has not yet been accomplished. A significant simplification arises if the search for stationary shapes is restricted to axisymmetric ones. This restriction is not as severe as it may look in

the first place since it turns out that in large regions of the interesting parameter space the shape of lowest energy is indeed axisymmetric for vesicles of spherical topology.

For axisymmetric shapes, the shape equation becomes an ordinary differential equation of higher order. It can be derived either by specializing the general shape equation (3.8) to axisymmetric contours, or by inserting a parametrization of an axisymmetric vesicle into the energy functional and then deriving the corresponding Euler–Lagrange equations. Shape equations for axisymmetric vesicles have been derived and solved using various parametrizations (Helfrich 1973, Deuling and Helfrich 1976, Jenkins 1977, Luke and Kaplan 1979, Luke 1982, Peterson 1985b, Svetina and Zeks 1989, Miao *et al.* 1991, Seifert *et al.* 1991). Recently, there have been claims that the shape equations as derived in the cited works are incorrect (Hu and Ou-Yang 1993, Naito *et al.* 1993, Zheng and Liu 1993). In the rebuttal of these claims it is pointed out that particular attention has to be given to the variation at the boundaries (Jülicher and Seifert 1994, Podgornik *et al.* 1995).

In principle, a systematic procedure can be conceived that exhausts all solutions of the axisymmetric shape equations using a shooting method (Seifert *et al.* 1991). Since its practical implementation, however, can become quite time-consuming, one rather needs a guided search for solutions. Such a guidance is provided by the bifurcations from the sphere, for which the parameters like  $P$  and  $\Sigma$  follow from the relations (3.12) and (3.15). These values can be used as good guesses for the shooting method.

For the ( $l = 2$ ) bifurcation, one thus finds prolate and oblate ellipsoids. Both types of shapes constitute a 2D sheet emerging from the sphere which can be parametrized by the reduced volume  $v$  and the reduced mean curvature  $m$ . As one follows these shapes away from the sphere, the prolates become continuously more dumbbell-like while the oblates become biconcave. Along a 1D curve in this sheet, sheets of shapes with broken up/down symmetry bifurcate from these up/down symmetric shapes. These are the pear shapes and the stomatocytes, respectively, as shown in the scheme in figure 11 (Seifert *et al.* 1991).

While the oblates and prolates as well as the pears and the stomatocyte sheets have been studied quite exhaustively, little is known about other sheets which correspond to bifurcations from the sphere at larger values of  $l$ . These shapes are unstable close to the sphere (Peterson 1989) but they could become stable for smaller reduced volume.

### 3.1.5. Limit shapes and neck condition

Sheets of shapes typically end in limit shapes where the contour becomes singular. The most prominent limit shape is that for the pears where the diameter of the neck has shrunk to zero. In this case, the shape consists of two spheres of radius  $R_A$  and  $R_B$ . It turns out that these radii have to fulfil the so-called ‘kissing’ or ‘ideal neck’ condition (Seifert 1990, Berndl 1990, Miao *et al.* 1991, Seifert *et al.* 1991)

$$1/R_A + 1/R_B = C_0. \quad (3.16)$$

This condition was first found empirically. It can also be proven by a subtle matching procedure (Fourcade *et al.* 1994). Despite its superficial simplicity, this condition has, however, so far evaded any ‘simple’ proof. A hint to where such a

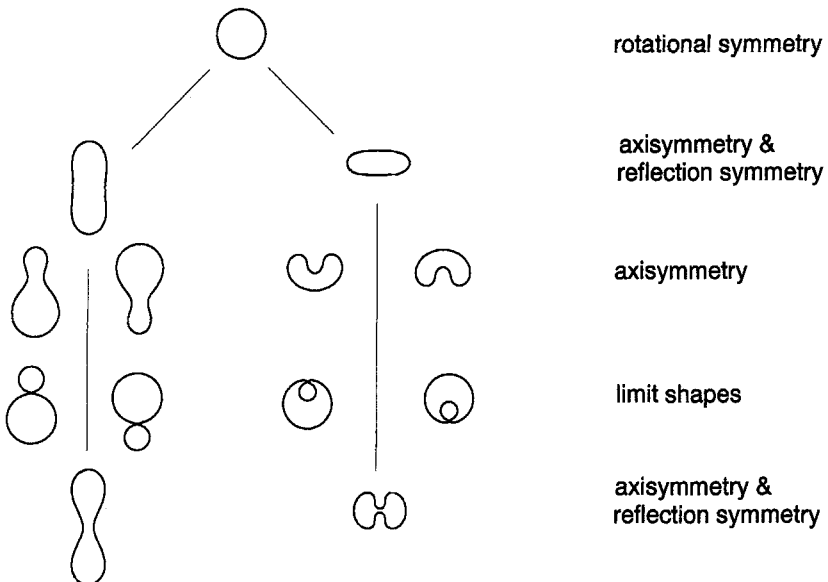


Figure 11. Bifurcation scheme with stationary shapes and their symmetry.

proof could start follows from the observation that the kissing condition implies that the curvature energy density  $(2H - C_0)^2$  is the same in both adjacent segments. The ideal neck condition applies also to limit shapes for which one segment, say A, is a prolate. In this case,  $R_A$  denotes the curvature of this shape at the pole.

Other limit shapes include an infinitely thin cylinder (for the prolates), two spheres of equal size (also for the prolates), a spherical cavity embedded in a larger sphere (for the stomatocytes), as well as shapes which self-intersect along the axis (for the discocytes and the stomatocytes) (Seifert *et al.* 1991). In the latter case, the sheets can be extended mathematically beyond the lines of self-intersection. Physically, however, such a limit line shows that for those parameters, self-interaction of the membrane has to be taken into account.

### 3.1.6. Cylinders and unduloids

Even though the main topic of this paper is that of closed vesicles, a brief look at cylindrical shapes is instructive. Cylindrical shapes are axisymmetric and no specific boundary condition at the end is implied. Clearly, in the presence of a spontaneous curvature  $C_0$ , cylinders with radii  $R_c = 1/C_0$  cost no bending energy. Likewise, a necklace of spheres with radius  $R_s = 2/C_0$  has no curvature energy. In the nineteenth century, Delaunay found a one-parameter family of constant mean curvature, the unduloids, which interpolate smoothly between these two shapes as shown in figure 12. These shapes resemble the myelin shapes found on the outside of aged red blood cells (Deuling and Helfrich 1977). In the absence of a spontaneous curvature, one needs a delicate balance of pressure and tension terms to stabilize cylinders. These terms can also arise from area and volume constraints (Ou-Yang and Helfrich 1989). Analytical expressions of unduloid-like axisymmetric solutions of the general shape equations (3.8) with *non-constant* mean curvature have recently been found (Naito *et al.* 1995).

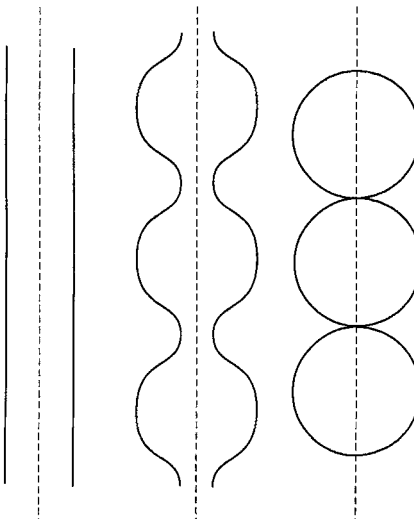


Figure 12. Cylinder, necklace of spheres, and interpolating unduloids. All shapes have locally the same constant mean curvature.

### 3.2. Complementary techniques for shape determination

#### 3.2.1. Variational approaches

Approximation to vesicle shapes can be obtained by minimizing in a restricted parameter space. In the apparently earliest paper concerned with shape determination of vesicles, Cassini ovals were used to parametrize discocytes in an attempt to find red blood cell shapes (Canham 1970). More recently, shapes parametrized by spherical harmonics have been used to investigate nonaxisymmetric ellipsoids (Heinrich *et al.* 1993). Certain amplitudes are fixed by the constraints. The minimization with respect to the free amplitudes in a subspace  $l \leq l_{\max}$  is better the larger the reduced volume.

#### 3.2.2. Direct numerical minimization

Non-axisymmetric shapes can be calculated by direct minimization of the curvature energy on a triangulated surface. Starting from some suitable initial shape, such an algorithm is supposed to find an adjacent local minimum by downhill minimization. Special care has to be taken to ensure stability and convergence of such an algorithm. Reliable results still require considerable computer time.

Brakke's surface evolver (Brakke 1992) is a quite flexible software package which has been used to obtain both vesicles of higher genus as discussed in more detail in section 5, and vesicle shapes subject to gravity as discussed in section 6.6 below. A somewhat different algorithm has been developed by Wintz to calculate non-axisymmetric ellipsoidal shapes (Jaric *et al.* 1995) and starfish vesicles (Wintz *et al.* 1996).

### 3.3. Continuous and discontinuous transitions

Any bifurcation between different branches of shapes can occur as a continuous or a discontinuous transition (Seifert *et al.* 1991). In this section, we discuss the two

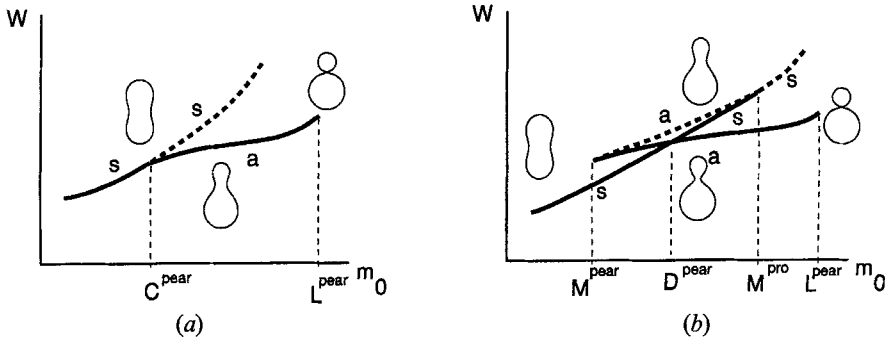


Figure 13. Continuous (a) and discontinuous (b) transition. Both figures show the energy  $W$  of the symmetric (s) and asymmetric (a) shapes as a function of the optimal reduced area difference  $m_0$  at fixed reduced volume  $\nu$  for (a) large  $\alpha$  and (b) small  $\alpha$ . Typical shapes are sketched along the branches. The dashed curves show the energy of unstable shapes. In case (a), all asymmetric shapes are locally stable; the symmetric shapes are unstable to the right of  $C^{\text{pear}}$ . In case (b), the asymmetric shapes are unstable on top of the Gibbs' wing.  $M^{\text{pear}}$  and the bifurcation point  $M^{\text{pro}}$  denote the spinodals of the discontinuous transition. The asymmetric branch ends in the limit shape  $L^{\text{pear}}$  (after Miao *et al.* (1994)).

variants paradigmatically for the prolate/pear bifurcation. The systematics and specific parameters for which each case applies will be given in section 3.6 below.

In figure 13, the energy  $W$  within the ADE model of the (symmetric) prolates and the (asymmetric) pears is sketched for two different values of  $\alpha$  as a function of the reduced area difference  $m_0$  while the reduced volume  $\nu$  is kept constant (Miao *et al.* 1994). Thus, the same one-parameter family of prolates and pears is involved in both cases because at constant  $\nu$  there is only a one-parameter family of prolates and pears, respectively. However, the topology of the energy close to the transition is qualitatively different. In the diagram on the left (typical for large  $\alpha$ ), which corresponds to a *continuous transition*, the symmetric shapes become unstable with increasing  $m_0$  beyond the point marked  $C^{\text{pear}}$ . In the diagram on the right hand side (typical for small  $\alpha$ ), the symmetric shapes become unstable with increasing  $m_0$  beyond the point marked  $M^{\text{pro}}$ . In the latter case, the asymmetric shapes close to the bifurcation, however, are also unstable since their energy constitutes the upper part of the ‘Gibbs’ wing’. This situation corresponds to a *discontinuous transition* since with increasing  $m_0$  the symmetric shapes become metastable beyond  $D^{\text{pear}}$  and unstable beyond  $M^{\text{pro}}$ . With decreasing  $m_0$ , the asymmetric shapes become metastable below  $D^{\text{pear}}$  and become unstable below  $M^{\text{pear}}$ . In the regime between  $M^{\text{pear}}$  and  $M^{\text{pro}}$ , the asymmetric shapes of the upper part of the Gibbs’ wing, in fact, correspond to the saddle points (and their energy to the activation energy) of this discontinuous transition. The asymmetric shapes close to the bifurcation thus change their stability as a function of  $\alpha$ . For large  $\alpha$ , they are stabilized by the area-difference-elasticity energy, while for small  $\alpha$  they become unstable.

In such a qualitative discussion of the generic feature of the energy diagrams, notions borrowed from thermodynamics have been used. Despite the appeal of such an analogy, it is important to keep in mind that there are fundamental differences between a thermodynamic phase transition and a shape transformation of a vesicle which, in fact, more closely resembles a bifurcation. A single vesicle does not form a

thermodynamic system in which phases of the same energy could coexist. The vesicle is either symmetric or asymmetric but it is not half symmetric and half asymmetric. As quantitative energy diagrams show, the activation energy between two locally stable shapes is of the order of  $\kappa$  times a numerical prefactor. The shape transformation in the case of a discontinuous transition will set in as soon as the activation energy between the ‘metastable’ and the globally stable shape becomes comparable to the thermal energy  $T$ . Depending on the specific transition, this point will be close to the limits of metastability as given by  $M^{\text{pro}}$  and  $M^{\text{pear}}$  for a ‘strong’ discontinuous transition and may be closer to  $D^{\text{pear}}$  for a weak transition. In the latter case, one may even expect fluctuations of the shape across the weak barrier.

A bifurcation diagram like figure 13 could easily be mistaken as suggesting too simple a view of a discontinuous transition. There is, in general, no guarantee that a metastable state will decay to a shape which corresponds to the Gibbs wing of this bifurcation if there are several branches of shapes involved (Jaric *et al.* 1995). Knowing what happens after the instability would require formulating properly the full dynamics, which is not yet possible even for axisymmetric shapes.

### 3.4. A simple model: local curvature energy only

The simplest model for vesicles consisting of symmetric bilayers is given by the local curvature energy  $G$  (2.51) and the constraints on area and volume. Because of the scale invariance of the curvature energy, this model depends only on one parameter, the reduced volume  $\nu$  defined in (3.11).

The axisymmetric stationary shapes in this model, which can be found by solving the shape equations (Seifert *et al.* 1991), comprise both the oblate ellipsoids (which become biconcave discocytes as the reduced volume is decreased) and the prolate ellipsoids (which acquire a long cylindrical shape as the reduced volume decreases). A third class of stationary shapes are the stomatocytes which bifurcate from the oblates through a transition which breaks the reflection symmetry. Both the energy of these branches and typical shapes are shown in figure 14.

Perturbation theory in the spherical limit (Milner and Safran 1987, Heinrich *et al.* 1992) shows (i) that the oblates which show up as stationary shapes in the energy diagram, in fact, are unstable, and (ii) that there are no stationary (let alone stable) non-axisymmetric ellipsoids in this limit. A systematic stability analysis shows that the oblates become locally stable for  $\nu < \nu_C^{\text{ob}} \simeq 0.75$  (Jaric *et al.* 1995). The same approach also indicates that the prolates remain locally stable for all  $\nu$ .

Collecting these results, the one-dimensional (1D) phase diagram contains the following sequence of absolute minimal shapes with decreasing  $\nu$  as shown in figure 14: prolates for  $\nu > \nu_D \simeq 0.65$ , oblates for  $\nu_D^{\text{sto}} < \nu < \nu_D$ , with  $\nu_D^{\text{sto}} \simeq 0.59$ , and finally stomatocytes for  $\nu < \nu_D^{\text{sto}}$ . The discontinuous prolate/oblate transition has a spinodal for the oblates at  $\nu_C^{\text{ob}}$ , whereas the prolates are (at least) metastable for all  $\nu$ . The discontinuous oblate/stomatocyte transition has spinodals at  $\nu_M^{\text{sto}} \simeq 0.66$  for the stomatocyte and  $\nu_C^{\text{sto}} \simeq 0.51$  for the oblate, respectively (Seifert *et al.* 1991).

Three facts about this simple model should be emphasized. (i) The biconcave discocytes have the lowest energy in a narrow range of reduced volume  $\nu$ . Thus, neither a negative spontaneous curvature nor any specific bilayer feature is necessary to obtain red-blood-cell-like shapes. (ii) Budding does not occur in this model since pears do not show up as stationary shapes in this variant. (iii) So far, there is no indication of the presence of locally (let alone globally) stable non-axisymmetric shapes in this model for any  $\nu$ .

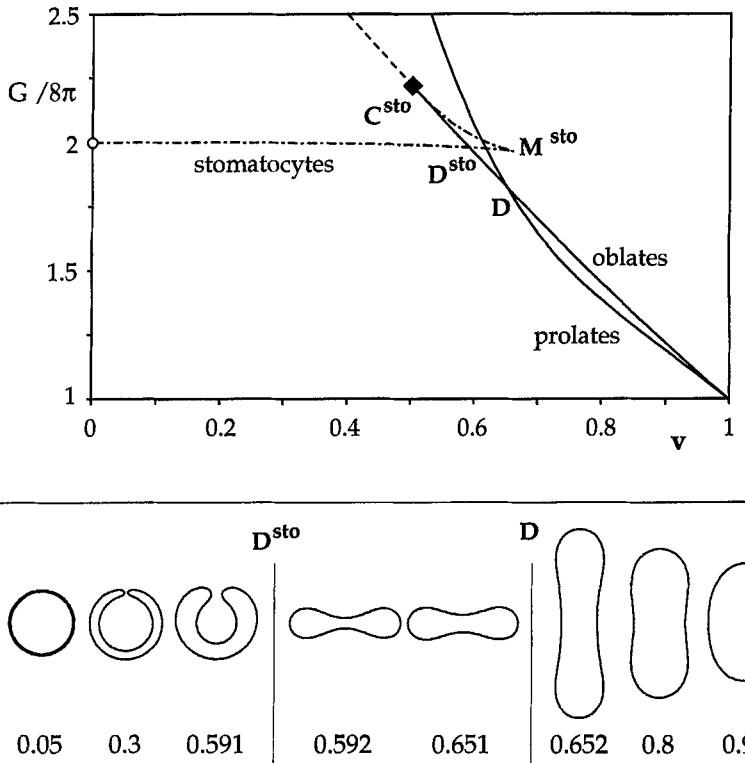


Figure 14. Energy  $G$  and contours of stationary shapes as a function of reduced volume  $v$ . All shapes have the same area.  $D$  and  $D^{sto}$  denote the discontinuous prolate/oblate and oblate/stomatocyte transition. The oblates and the stomatocytes lose metastability at  $C^{sto}$  and  $M^{sto}$ , respectively. Beyond the diamond, the oblates self-intersect (Seifert *et al.* 1991).

### 3.5. Bilayer-couple model

In this variant, a second constraint is imposed on the reduced mean curvature  $m$  which gives rise to a 2D phase diagram. A fourth class of axisymmetric shapes, the pears, as well as non-axisymmetric ellipsoids, now become relevant (Svetina and Zeks 1989, Seifert *et al.* 1991).

The axisymmetric shapes show up in two separate regions of the phase diagram shown in figure 15. The prolates and the pears occur for larger values of  $m$ , and the oblate shapes and the stomatocytes for smaller values of  $m$ . In both cases, the reflection symmetry is broken continuously at  $C^{sto}$  and  $C^{pear}$ , respectively. The pears and the stomatocytes are both bounded by a limit line. For the pears, this limit line  $L^{pear}$  is the vesiculation line where the neck diameter connecting the two spherical compartments has shrunk to zero. The location of this line follows straight from geometry as (Svetina and Zeks 1989, Seifert *et al.* 1991)

$$v_L^{pear}(m) = 1 - 3[m/(4\pi) - 1]^2/2 - [m/(4\pi) - 1]^3/2, \quad (3.17)$$

with  $1 \leq m/(4\pi) \leq \sqrt{2}$ . This limit line starts at the point  $E$  where two spheres with equal radius sit on top of each other and ends at the point  $S$  of a sphere. The same

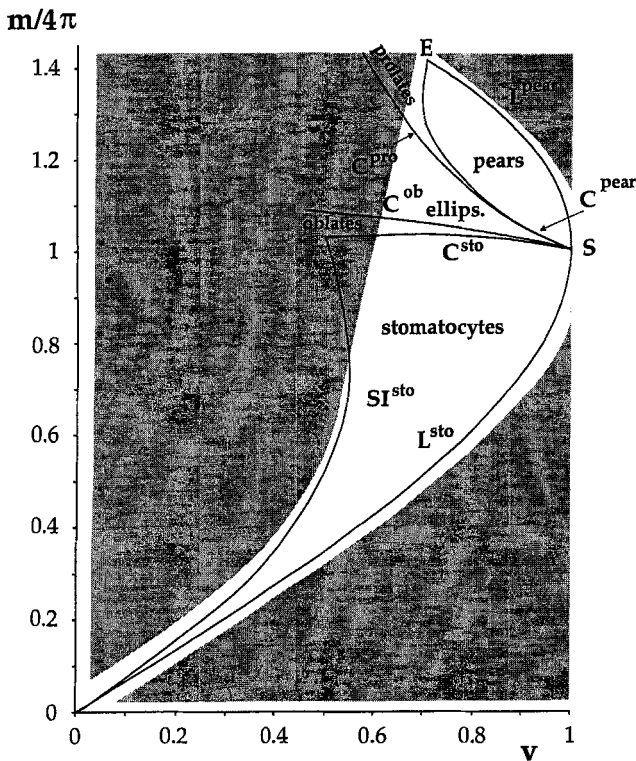


Figure 15. Phase diagram of the bilayer coupling model. This phase diagram shows the state of lowest energy as a function of the reduced area difference  $m$  and of the reduced volume  $\nu$ .  $C^{pear}$  denotes the line of continuous transitions between up-down symmetric prolate/dumb-bell shapes and up-down asymmetric pear shapes. Likewise,  $C^{sto}$  denotes the locus of the continuous transitions between the oblate/discocyte shapes and the stomatocytes.  $L^{pear}$  and  $L^{sto}$  are limit curves which correspond to budding and the inclusion of a spherical cavity, respectively.  $S$  corresponds to a sphere. In the region between the prolate/dumb-bell and discocyte regime, non-axisymmetric ellipsoids have lowest energy. This region is separated by continuous transitions  $C^{pro}$  and  $C^{ob}$  from the corresponding axisymmetric shapes.  $E$  denotes the point where two spheres of equal radii are sitting on top of each other. Along the line  $SI^{sto}$ , the two poles of the shape touch each other. In the shaded areas, the shape of lowest energy has not been determined so far. (After Seifert *et al.* (1991).)

two points are also connected by the line  $C^{pear}$  of continuous transitions between the prolates and the pears.

The stomatocytes are likewise bound by a limit line of shapes  $L^{sto}$  which consist of a sphere that encloses a smaller sphere. Both spheres are connected by an ideal neck. The locus  $L^{sto}$  is also given by (3.17) with  $0 < m/(4\pi) < 1$ .

The gap between the prolates and the oblates has been conjectured as filled with non-axisymmetric ellipsoids, which are separated by two continuous transitions  $C^{ob}$  and  $C^{pear}$  from the axisymmetric shapes (Seifert *et al.* 1991). This prediction has since been verified by the variational approach (Heinrich *et al.* 1993).

Significant parts of the phase diagram have not yet been systematically explored. There are three reasons for our lack of knowledge about shapes of lowest energy in these regions. First, there is a region above the oblates and to the left of  $\nu \simeq 0.7$

where shapes with different symmetry, such as starfish vesicles as described in section 3.10.4, or shapes with only two symmetry planes (Schnitzler 1993), become relevant. Secondly, above the limit line  $L^{\text{pear}}$  and below  $L^{\text{sto}}$ , two types of shapes can occur which have not yet been investigated in detail either. One would expect that either the necks remain ideal and one of the spheres becomes a prolate, or that shapes which involve three compartments with finite necks occur. From a more physical perspective one could consider how the membrane–membrane interaction, such as the van der Waals interaction in the region of the necks, becomes a relevant parameter for a faithful description of the physics in this region (Käss *et al.* 1993). The same remark applies to a third region which is to the left of the line  $SI^{\text{sto}}$  where the membrane self-intersects. Again, further energy terms should be invoked here. One could either apply just self-avoidance of the membrane, or one could allow for self-adhesion, in which case at least one more parameter, such as the adhesion energy becomes relevant. The latter case has recently been studied in the context of adhering vesicles (Kraus *et al.* 1995).

### 3.6. Area-difference-elasticity model

In this variant, the constraint on the total mean curvature  $m$  is relaxed. It becomes an elastic energy which arises physically from the relative compression and expansion of the two monolayers as derived in section 2.4. In dimensionless units, the energy  $W$  as defined in (2.50) is given by

$$W(\alpha, \nu, m_0) = \kappa[G(\nu, m) + \alpha(m - m_0)^2/2], \quad (3.18)$$

where the scaled optimal area difference  $m_0$  has been introduced in (2.56). Since the ADE model contains the three parameters  $\nu$ ,  $m_0$  and  $\alpha$ , its phase diagram is more complex than that of the BC model, even though no new shapes occur due to the fact that the manifold of all shapes is only (degenerate) two-dimensional. Two fairly detailed studies within this model focus on the budding regime (Seifert *et al.* 1992, Miao *et al.* 1994) and the prolate–oblate transition (Heinrich *et al.* 1993). A comprehensive study presents the phase diagram and stability limits for reduced volume  $\nu \gtrsim 0.6$  and a particular experimentally relevant value of the material parameter  $\alpha$  (Jaric *et al.* 1995).

#### 3.6.1. Mapping property

As a recurrent theme in the ADE model, transitions which are continuous in the BC model ( $\alpha = \infty$ ) become discontinuous at a tricritical point with decreasing  $\alpha$  (Seifert *et al.* 1992, Miao *et al.* 1994, Heinrich *et al.* 1993). This phenomenon applies to the budding transition, as well as to the oblate–ellipsoid–prolate transition. It originates in the equivalence of the ensembles discussed in section 3.1.1, which leads to a mapping of the energy diagrams from the BC model to the ADE model.

As the correspondence between the variants of the curvature model implicit in equations (3.3) and (3.5) shows, any particular shape with  $\nu$  and  $m$  is a stationary shape for all parameter sets which obey the relation

$$m_0^{(n)} = m^{(n)} + (\partial G / \partial m) / \alpha. \quad (3.19)$$

Here, and in the following, the derivative of the bending energy  $G(m)^{(n)}$  is taken at fixed  $\nu$  along a branch of stationary shapes labelled with  $^{(n)}$ . For each stationary shape, (3.19) establishes a one-to-one mapping from  $(m^{(n)}, \nu)$  in the BC model to  $(m_0^{(n)}, \nu)$  in the ADE model.

This mapping is very useful for the determination of the phase diagram in the ADE model from that of the BC model, since it allows us to map, in particular, the location of symmetry breaking bifurcations such as  $C^{\text{pear}}$ ,  $C^{\text{pro}}$ ,  $C^{\text{ob}}$  and  $C^{\text{sto}}$  as well as the location of the limit lines  $L^{\text{pear}}$  and  $L^{\text{sto}}$  to any finite  $\alpha$  subsection. One just needs to know  $m(\nu)$  and  $(\partial G/\partial m) = 2c_0(\nu)$  of these shapes.

For the limit lines  $L^{\text{pear}}$  and  $L^{\text{sto}}$ , the mapping can be performed analytically since  $m(\nu)$  and  $c_0(\nu)$  of these shapes are known from equation (3.17) and the ideal neck condition (3.16) if the latter is written in dimensionless variables. One thus obtains

$$m_{0,L}(\nu) = m(\nu) + [m(\nu)/\alpha\pi]/\{[m(\nu)/4\pi]^2 - 1\}. \quad (3.20)$$

The determination of the phase diagram in the ADE model from that of the BC model, however, is non-trivial since the mapping (3.19) can become non-monotonic as a function of  $m$ . Indeed, differentiating 3.19 with respect to  $m$  leads to the relation

$$\partial m_0^{(n)}/\partial m = 1 + \left(\partial^2 G^{(n)}/\partial m^2\right)_{|\nu}/\alpha, \quad (3.21)$$

which shows that with increasing  $\alpha$ , the mapping (3.19) becomes non-monotonic whenever  $\partial^2 G^{(n)}/\partial m^2 \equiv G^{(n)''}(\nu)$  is negative somewhere along a branch. For an illustration of this phenomenon, which ultimately changes the character of a bifurcation from continuous to discontinuous, we will consider the prolate–pear bifurcation where this mechanism has been studied in detail.

Numerically established properties of the symmetric and the asymmetric branches imply two different scenarios for the prolate/pear bifurcation in the ADE model, corresponding to the continuous and discontinuous transitions,  $C^{\text{pear}}$  and  $D^{\text{pear}}$ , respectively (Miao *et al.* 1994). (i) For  $\alpha > \alpha_T(\nu)$ , the mapping (3.19) is monotonic for both the symmetric and asymmetric branches, and the topology of the energy diagram of the BC model is well preserved, as illustrated in figure 13(a), so the symmetry-breaking transition is continuous. The corresponding phase boundary  $C^{\text{pear}}$  is given by

$$m_{0,C} = m_C + G^{(s,a)'}(\nu, m_C)/\alpha. \quad (3.22)$$

(ii) When  $\alpha < \alpha_T(\nu)$ , the mapping (3.19) becomes non-monotonic for the asymmetric branch, while it remains monotonic for the symmetric branch. As a consequence, a ‘wing’ structure in the energy diagram, as shown in figure 13(b), appears. The position of the cusp on the left side of the wing is determined by  $G^{(a)''}(\nu, m) = -\alpha$ . This relation determines the spinodal  $M^{\text{pear}}$ , for the pears. The corresponding discontinuous budding transition occurs at  $D^{\text{pear}}$ , the precise location of which must be computed numerically.

The tricritical point  $T^{\text{pear}}$  at which  $C^{\text{pear}}$  and  $D^{\text{pear}}$  meet has coordinates  $(\alpha_T(\nu), m_{0,T}(\alpha))$ , where  $\alpha_T$  satisfies the condition  $\alpha_T = -G^{(a)'}(\nu_T, m_C)$ , and  $m_{0,T}$  is given through the mapping (3.19).

### 3.6.2. Phase diagram for $\alpha = 1.4$

The phase diagram of the ADE model as shown in figure 16 has been obtained by using this mapping procedure and the following three methods (Jaric *et al.* 1995). First, axisymmetric shapes were calculated by solving the shape equations. Secondly, a systematic stability analysis of these shapes was performed. Finally, the relevant non-axisymmetric shapes were calculated by direct minimization. The choice of  $\alpha = 1.4$  corresponds to the measured value for SOPC (Miao *et al.* 1994, Waugh *et al.* 1992).

While the phase diagram refers to the shapes of lowest energy only, the stability diagram shown in figure 17 plots the regions in  $(v, m_0)$  over which each of the low-lying stationary branches  $n$  are locally stable. These regions, which in general overlap, represent the maximum domains of stability/metastability for each branch and include, of course, the corresponding regions of the phase diagram.

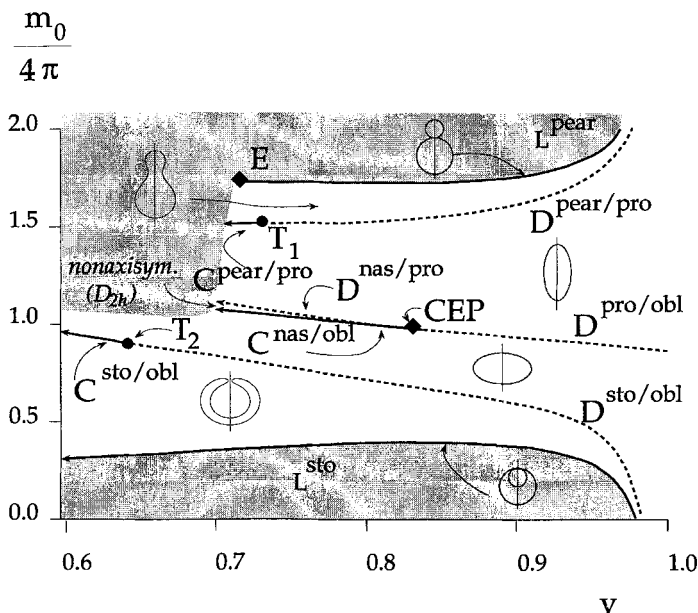


Figure 16. Phase diagram of the ADE model for  $\alpha = 1.4$ . This phase diagram shows the state of lowest energy as a function of the reduced equilibrium area difference  $m_0$  and of the reduced volume  $v$ . Between the limiting lines  $L^{pear}$  and  $L^{sto}$  and for reduced volumes  $v > 1/\sqrt{2}$ , the only equilibrium shapes which appear are pears, prolates, oblates, stomatocytes, and elliptical non-axisymmetric shapes (nas). Other phases occur outside the limiting lines and for  $v < 1/\sqrt{2}$ , i.e. in the shaded region. Characteristic equilibrium shapes are illustrated for each phase and for the two limiting lines. First-order, discontinuous transitions (D) are shown as dashed curves; second-order, continuous transitions are shown as full curves. At the special point E, the radii of the two spheres of the limiting pear shape become equal.  $T_1$  and  $T_2$  are tricritical points, CEP is a special critical endpoint. In the limit  $v \rightarrow \infty$ , the boundaries  $L^{pear}$  and  $D^{pear/pro}$  go to plus infinity and the boundaries  $L^{sto}$  and  $D^{sto/obl}$  go to minus infinity, as may be shown analytically (Seifert *et al.* 1991, Miao *et al.* 1994). Locations of the special points are ( $v = 1/\sqrt{2}$ ,  $T_1$  ( $v = 0.730$ ),  $T_2$  ( $v = 0.645$ ), and CEP ( $v = 0.827$ )). Note the narrow sector where the non-axisymmetric ellipsoids are stable, to the left of CEP between  $D^{nas/pro}$  and  $C^{nas/obl}$  (Jaric *et al.* 1995).

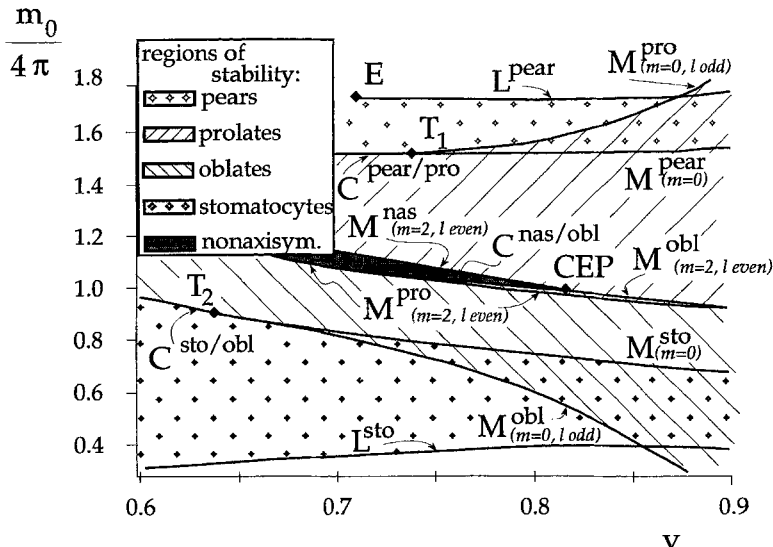


Figure 17. Stability diagram of the ADE model for  $\alpha = 1.4$  over the same region covered by figure 16. The textured areas identified by the key indicate the regions of local stability of the five phases shown. The limiting lines  $L$  and the continuous transitions  $C$  are the same as in figure 16. In addition, the spinodal lines  $M$  mark other limits of local stability (Jaric *et al.* 1995).

### 3.7. Spontaneous curvature model

The phase diagram for the spontaneous curvature model depends on the two parameters  $\nu$  and the scaled spontaneous curvature  $c_0$  as defined in equation (2.56). This phase diagram is shown in figure 18, as obtained by an analysis of the appropriate energy diagrams of the stationary shapes (Seifert *et al.* 1991). So far, there is no evidence that non-axisymmetric shapes could be relevant anywhere in the phase diagram.

In the region of moderate  $c_0$ , the phase diagram is dominated by four large regions of axisymmetric shapes. For positive  $c_0$ , these are the pears which are separated by a strong first-order transition from the prolates. With decreasing  $c_0$ , the prolates become oblates via another first-order transition, which becomes weak in the spherical limit where it hits the sphere at  $c_0 = -1.2$ . For negative  $c_0$ , the oblates undergo another strong first-order transition to the stomatocytes. In fact, all but one of the transitions found so far are discontinuous in this model.

There are significant parts of the phase diagram where either self-interaction of the membrane has to be taken into account, or where the analysis of the axisymmetric stationary shapes is still incomplete, which is particularly true in the vicinity of the point E where two spheres of equal size sit on top of each other. This shape does not cost energy in this model. For large positive  $c_0$ , a thorough investigation shows that a whole sequence of multiple vesiculated shapes appears since the energy now prefers spheres of radius  $2/C_0$  (Miao *et al.* 1991, Miao 1992).

### 3.8. Temperature trajectories

Any detailed comparison of the theoretical results with experimental data requires an understanding of how theoretical quantities such as the reduced volume

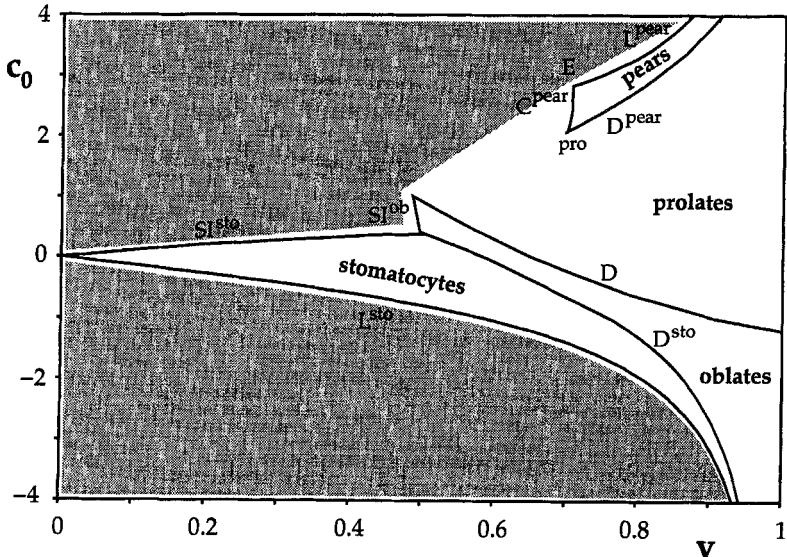


Figure 18. Phase diagram of the spontaneous curvature model. This phase diagram shows the shape of lowest bending energy as a function of the scaled spontaneous curvature  $c_0$  and of the reduced volume  $v$ . The regions where the prolate/dumb-bell, pear-shaped, oblate/discocyte and stomatocytes have lowest energy are separated by transition lines. The line  $C^{\text{pear}}$  denotes a continuous transition. All other transitions are discontinuous. At E, two spheres of equal size sit on top of each other. The lines  $L^{\text{sto}}$  and  $L^{\text{pear}}$  correspond to limit shapes with infinitesimal neck. Beyond the lines  $SI^{\text{ob}}$  and  $SI^{\text{sto}}$ , self-intersecting states occur. In the shaded area, the shape of lowest energy has still to be determined. (After Seifert *et al.* (1991).)

$v$  or the equilibrium area difference  $m_0$  depend on experimentally accessible parameters such as temperature or osmotic conditions (Berndl *et al.* 1990, Seifert *et al.* 1991).

An increase in temperature from an initial value  $T_0$  leads to thermal expansion of the area of the two monolayers. It will be necessary to admit a small asymmetry  $\gamma$  of the expansion coefficients of the two monolayers, and , defined as

$$\beta^{\text{in}} \equiv \frac{1}{A^{\text{in}}} \frac{\partial A^{\text{in}}}{\partial T} \equiv \beta \quad \text{and} \quad \beta^{\text{ex}} \equiv \frac{1}{A^{\text{ex}}} \frac{\partial A^{\text{ex}}}{\partial T} \equiv (1 + \gamma)\beta. \quad (3.23)$$

A typical value is  $\beta \simeq 6 \times 10^{-3} K^{-1}$  (Evans and Needham 1987), which is one order of magnitude larger than the expansion coefficient for the enclosed aqueous solution. The latter can therefore be neglected. For temperature-independent expansion coefficients, the temperature trajectory is given by

$$m_0 = \left[ \frac{v(T_0)}{v} \right]^r \left\{ m_0(T_0) + b \left[ \left( \frac{v(T_0)}{v} \right)^q - 1 \right] \right\}, \quad (3.24)$$

parametrized by an initial point with  $m_0 = m_0(T_0)$  and  $v = v(T_0)$  on the trajectory (Berndl *et al.* 1990, Seifert *et al.* 1991). The exponents are given by

$$q = (2 + \gamma)/3 \quad \text{and} \quad r = \frac{2 - \gamma - 4\beta_d/\beta}{3(2 + \gamma)}, \quad (3.25)$$

where  $\beta_d$  is the thermal expansion coefficient of the bilayer. The exponent  $r$  can be bounded theoretically by the following two limiting cases. (i) If the monolayer separation  $2d$  does not change with temperature, one has  $= 0$  which leads to  $r = 1/3$ . (ii) If  $d$  decreases with temperature in such a way that the bilayer volume as given by  $\sim Ad$  remains temperature independent, i.e.  $= -\beta$ , one has  $r = 1$ . Experiments using nuclear magnetic resonance indicate that the latter case is a good approximation (Nezil and Bloom 1992). Without asymmetry, i.e. for  $= 0$ , one obtains the simple expression

$$m_0(v) = m_0(T_0) \left[ \frac{v(T_0)}{v} \right]^r. \quad (3.26)$$

The dimensionless coefficient  $b$  in (3.24), which determines the effect of an asymmetric expansion, is given by

$$b \equiv \frac{A^{\text{ex}}(T_0)}{8d(T_0)\{\pi A^{\text{in}}(T_0)\}^{1/2}} \simeq \frac{1}{4} \frac{R_0(T_0)}{d(T_0)}. \quad (3.27)$$

For giant vesicles, this coefficient is of the order of  $10^3 - 10^4$ , which indicates that even a tiny asymmetry of the order of  $10^{-3}$  has an enormous influence on a temperature trajectory as demonstrated first within the BC model (Berndl *et al.* 1990). The physical basis for this surprising effect is the length-scale separation alluded to in section 2. The relevant scale for changes in the optimal area difference is  $dR_0$ , whereas the scale for the absolute change in area is  $R_0^2$ . Thus, small differences in the thermal expansion of the two layers get ‘magnified’ by a factor  $R_0/d$ . As a consequence, if the outer monolayer expands more than the inner one, the additional area accumulated in this outer layer will cause budding since the formation of buds increases the area difference. Likewise, a stronger increase of the area of the inner monolayer induces a transition to the discocytes and the stomatocytes.

This sensitive dependence of the thermal trajectory in the phase diagram indicates that it will be rather difficult in general to reproduce experiments on vesicle shape transformations. Presently, the available purity of the lipids does not exclude the presence of residual impurities which could result in an asymmetric expansion of the order of  $10^{-3}$ . It would be highly beneficial to investigate this effect systematically by deliberately adding traces of a second (miscible) component to one of the monolayers. However, one then has to be aware of additional effects arising from the mixture as discussed in section 8.

For a complete prediction of the temperature trajectory, the initial value ( $m_0(T_0)$ ,  $v(T_0)$ ) has to be known. For axisymmetric vesicles, the volume, as any other geometrical quantity such as the total mean curvature, can be inferred in principle from the mean contour of the vesicle, if the orientation of the symmetry axis is known. However, thermal fluctuations, as well as rotational diffusion of the vesicle, limit the resolution. The reduced volume has thus been obtained within one percent accuracy.

The optimal area difference  $m_0$  is not yet accessible to any non-invasive direct measurement. According to the present understanding, this quantity depends on the

number of molecules in the two monolayers as the vesicle is formed. If one assumes that the vesicles are relaxed with respect to the non-local bending energy right after they have been formed, i.e.  $m = m_0 > 0$ , the dimensionless equilibrium area difference  $m_0$  would depend on the specific shape the vesicle acquired after closure. The difference between, for example, a sphere and a capped cylinder leads to a difference of  $O(1)$  in  $m_0$  (Miao 1992), which then leads to different temperature trajectories even if the thermal expansion is symmetric. Recently, the optimal area difference  $m_0$  has been measured for vesicles aspirated in micropipettes from which thin tethers are extruded (Evans and Yeung 1994, Yeung 1994). The result shows a broad distribution of values around  $m_0 = 0$  which would indicate that the area difference does not adjust to the shape at the moment of closure. Whether such a distribution of  $m_0$  is specific to the set-up of that experiment or whether it holds generally remains to be seen.

An indirect way of measuring the equilibrium area difference has been attempted (Döbereiner 1995). Since the manifold of all shapes is one-dimensional for fixed reduced volume, measuring the volume and at least one quantity which depends on the contour allows us to map an experimental shape on a theoretical shape and thus measure the corresponding equilibrium area difference. Döbereiner has chosen to use a particular expansion coefficient when the contour of a prolate is expanded around a circle. At least two effects complicate such an approach. First, the prolates have to be filled with a slightly denser liquid so that they sink to the bottom of the chamber to prevent 3D rotational diffusion. Secondly, the measured mean contours deviate from the contours of lowest energy due to the effect of finite thermal fluctuations. Both effects should be included in the theoretical analysis, as discussed in sections 6.6 and 4.1.4, respectively.

### 3.9. Budding transition

The budding transition is the most thoroughly studied shape transformation. Its appeal originates not only in the close resemblance to biologically important phenomena such as exo-cytosis or budding of vesicles at the golgi apparatus, but also from conflicting experimental data described below. This discrepancy fostered intense theoretical and experimental efforts which finally seem to have reached a unifying coherent picture.

#### 3.9.1. Apparently conflicting experimental scenarios

Early studies of temperature-induced budding exhibited two apparently conflicting results. (i) For DMPC vesicles, a slow increase in temperature was reported to lead to a continuous transition from a prolate to a pear with weak up-down asymmetry which upon further temperature change jumps to a vesiculated shape with a narrow neck (Käs and Sackmann 1991). (ii) For SOPC vesicles in sucrose/glucose solutions, discontinuous budding was observed without the pear-shaped intermediates (Döbereiner 1995). A similar sequence has also been obtained for DMPC vesicles provided they are kept under some tension before the heating starts (Käs and Sackmann 1991). This second scenario is compatible with the theoretical prediction within the ADE model for a realistic value of  $\alpha$ .

An early theoretical explanation of the continuous transition in the first scenario has been given in the context of the BC model (Berndl *et al.* 1990). However, the apparent transition from a wide neck to a narrow neck is not even contained in any of the curvature models discussed so far. Further energy terms of the type

$q(m - m_0)^3$  could, in principle, provide such a scenario (Käs *et al.* 1993) but only with the *ad hoc* assumption of an amplitude  $q$  of the order of  $10^2$ . However, one expects any corrections to the area difference elasticity (2.50) arising from elastic interactions to be of the order of  $d/R_0 \simeq 10^{-3}$ . This magnitude is not sufficient to cause a discontinuous transition between two different neck sizes.

### 3.9.2. Spinodal fluctuations

A thorough experimental analysis in combination with a simple theoretical picture provides an attractive resolution to the apparently conflicting earlier measurements by interpreting the weak pears of scenario (i) above as long-lived spinodal fluctuations (Döbereiner *et al.* 1995). Pear-like fluctuations in the prolate phase thus get more pronounced and take longer to relax as the budding instability is approached. These slow fluctuations may have been mistaken as equilibrium shapes in the earlier study (Käs and Sackmann 1991).

Theoretically, the phase diagram of the ADE model (figure 16) predicts a discontinuous transition from the prolate to the pear for all values of the reduced volume and any reasonable value of  $\alpha$  for a single membrane. Thus, the details of the temperature trajectory do not matter as long as the trajectory hits the budding transition. With decreasing temperature, the prolate first enters the metastable regime where the lowest energy shape is pear-like but the prolate remains stable against local fluctuations. As the limit of stability at  $v = v_b(m_0)$ , denoted by  $M^{pro}$  in figure 17, is approached, the prolates become locally unstable to a pear mode, which eventually carries it over an energy barrier and down to the asymmetric minimum-energy shape, which is budded. At the Landau-theory level, one can characterize this sequence of events by an energy functional (Seifert 1995c, Döbereiner *et al.* 1995)

$$V(a) = \kappa \left( \frac{1}{r} a^2 - \frac{1}{g} a^4 + \frac{1}{u} a^6 \right), \quad (3.28)$$

where  $a$  is the amplitude of the mode which becomes soft at  $v_b$ , and the remaining parameters,  $r, g > 0$ , and  $u > 0$ , are dimensionless. The symmetrical (prolate) branch loses metastability as  $(v - v_b) \sim r \rightarrow 0^+$ . Amplitude fluctuations are given at the Gaussian level by  $\langle a^2 \rangle = k_B T / \kappa r$ , which is only expected to be valid when  $\langle a^2 \rangle \ll r/g$ , so the non-Gaussian terms may be neglected. Indeed, when this criterion is not satisfied, there is significant probability of escape over the barrier. It follows that there is a range of reduced volume,  $gk_B T / \kappa \ll r^2 \ll 1$ , near but not too near the budding instability, for which the static fluctuations are predicted to grow as  $(v - v_b)^{-1}$ .

Such a dramatic increase in the amplitude of pear-like fluctuations has indeed been observed experimentally (Döbereiner *et al.* 1995). Snapshots of the contour fluctuations of a prolate fixed to the bottom of a measuring chamber by gravity due to a slightly denser interior fluid have been recorded by video microscopy. The quantitative analysis is based on an expansion of the angle  $\psi(s)$  between the normal to the axis and the local tangent to the contour in suitable modes.

Discussion of the time dependence of the modes requires a dynamical theory, which will be introduced in section 7. Since the motion of these length-scales is determined by dissipation in the surrounding water, the soft mode should obey a dynamical equation of the purely dissipative type (Seifert 1995c, Döbereiner *et al.* 1995),

$$\partial a / \partial t = -\Gamma \partial V / \partial a + \zeta, \quad (3.29)$$

where  $\zeta$  is the usual noise term. (3.29) simplifies to  $\partial a / \partial t = -\Gamma \kappa r a + \zeta$  near  $a = 0$ , when the Gaussian term dominates. The kinetic coefficient  $\Gamma = c / \eta R^3$  is dominated by the solvent viscosity  $\eta = 10^{-2}$  erg s cm<sup>3</sup> for water; the appropriate length scale for the unstable mode is the size scale  $R \simeq 10$  μm of the vesicle. The numerical factor  $c$  is of order unity. In the Gaussian regime, (3.29) predicts

$$\langle a(t) a(0) \rangle = \langle a^2 \rangle \exp(-t/\tau), \quad (3.30)$$

with  $\tau = (\Gamma \kappa r)^{-1} \sim (\nu - \nu_b)^{-1}$ . Such a growing correlation time is consistent with observation (Döbereiner *et al.* 1995).

Behaviour near such a spinodal that describes the limit of stability of a metastable state is analogous to behaviour near a second-order phase transition. However, the analogy with phase transitions should be used carefully (Döbereiner *et al.* 1995). In a true thermodynamic second-order transition, both the characteristic fluctuation amplitude and the dominant relaxation time ultimately diverge at the transition but with exponents renormalized from their mean-field values by cooperative effects due to the many long-wavelength degrees of freedom. For a spinodal, on the other hand, this divergence is never achieved because the fluctuating state is globally unstable and decays when the fluctuations reach a finite size.

For a simple mechanical system like the vesicle, there is only one unstable mode, so no renormalization occurs. The attractive feature of this mechanical instability is to have a system in which the energy barrier in the metastable state is only a few times  $T$ , so that significant pretransitional fluctuations can occur, and in which the height of the barrier can be controlled delicately on the scale of  $T$ .

While the onset of the budding instability can thus be quantitatively understood, beyond a more qualitative discussion of the relevant time-scales (Fischer 1994) little can be said about the dynamics of the decay of the prolate towards the new pear-shaped minimum. Even though the deterministic dynamics of an axisymmetric contour, including the hydrodynamics of the surrounding liquid, can be formulated (Langer and Seifert 1996), the numerical solution of these equations is still plagued with spurious instabilities.

### 3.10. Other shape transformations

Even though the budding transition has been studied most intensively, there are further shape transformation which should also be related to the theory.

#### 3.10.1. Re-entrant trajectory

The re-entrant transition, as shown in figure 2, has been reported to show no hysteresis at all (Berndl *et al.* 1990, Käs and Sackmann 1991). This transition could be explained within the bilayer-couple model as demonstrated by the theoretical contours shown in figure 2 (Berndl *et al.* 1990). The character of this transition will also persist in the ADE model at large enough  $\alpha$ , but not for  $\alpha \simeq 1$ . Taking the experiment as well as the theory seriously, there are two possible explanations. (i) Vesicles for which this transition has been observed could be multi-lamellar, which would correspond to an effectively larger  $\alpha$  (Svetina and Zeks 1992). (ii) For small reduced volume and  $\alpha \simeq 1$ , the transition between the prolate and the pears is

predicted to be only weakly discontinuous. Experimentally, it may be difficult to distinguish such a weak transition from a continuous transition.

### 3.10.2. Discocyte–stomatocyte transition

The discocyte–stomatocyte transition as shown in figure 3, was first reported to be continuous (Berndl *et al.* 1990). However, closer inspection revealed a discontinuous character (Käs and Sackmann 1991). One could expect that the discrepancy can be attributed again to slow spinodal fluctuations as discussed above for the budding instability. Experimentally, this transition occurs more rarely than budding. This fact fits with the theoretical picture of the ADE model since one either needs a considerable negative asymmetric expansion coefficient  $\gamma$ , or an initial area difference  $m_0(\nu = 1)$  substantially smaller than the relaxed value  $4\pi$ , to reach this part of the phase diagram.

### 3.10.3. Equilibrium area difference as control parameter

There are two effects which indicate that  $m_0$  can be modified by other factors than temperature. Firstly, redistributing lipids from one monolayer to another by applying a transmembrane pH-gradient induces shape transformations similar to those predicted theoretically as one increases  $m_0$  (Farge and Devaux 1992, Mui *et al.* 1995). Secondly, the effect mentioned above, that precooling leads to budding can, somewhat speculatively, also be related to changes in  $m_0$ . It has been proposed that osmotically enforced flow of water through the membrane drags along lipid molecules (Boroski *et al.* 1981). Since precooling also forces liquid to flow through the membrane, one could wonder whether such a treatment also causes an increase in  $m_0$ . In the phase diagram, shown in figure 16, this would shift the initially spherical vesicle upwards. A temperature trajectory starting at the sphere would then reach the budding line for a smaller temperature increase, and the size of the buds should be smaller. So far, there are no systematic tests of such a hypothesis.

### 3.10.4. Starfish vesicles

Vesicle shapes at smaller reduced volume than described so far show surprising new features. These starfish shapes have first been found in multi-component membranes. In a quite comprehensive study (Hotani 1984), various starfish vesicles were found for a phospholipid–cholesterol *mixture* by osmotic deflation. In fact, in another study (Duwe 1989), the occurrence of such a shape has been speculated to derive from lateral phase segregation within the membrane. More recently, it has been shown both experimentally by using single component membranes and theoretically by minimizing the curvature energy on a triangulated surface that starfish are generic at small reduced volume even for *homogeneous* phospholipid bilayers (Wintz *et al.* 1996).

The most striking feature of these shapes, one of which is shown in figure 19 as experimentally observed and theoretically calculated, is their construction principle. All these shapes are built up using three structural elements. The centre consists of a quite flat, nearly axisymmetric core. Attached to this core are cylindrical arms which end in spherical caps. The radius of the caps is somewhat larger than the radius of the cylinder. The overall shape is quite flat.

The numerical work shows that the different starfish branches nearly overlap and that bifurcations take place in too narrow a region to be unambiguously resolved even with very fine triangulation and using substantial computer time (Wintz *et al.*

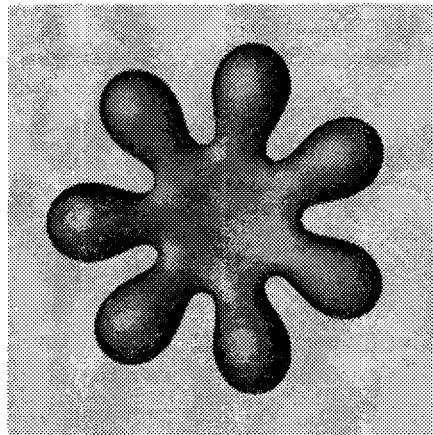
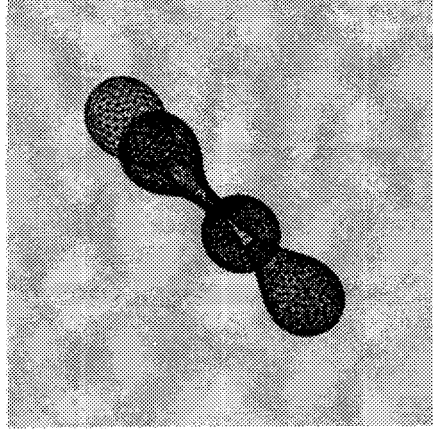
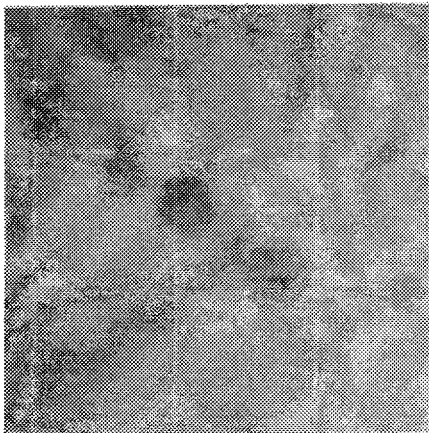
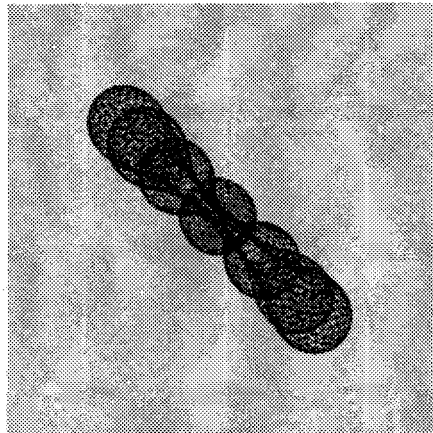


Figure 19. Seven-armed starfish vesicle. Three perpendicular views are shown of both an experimental and a theoretical shape (Wintz *et al.* 1996).

1996). The systematics of the respective transitions between the different starfish is thus too intricate to allow for as complete a picture as was obtained in the high-volume region. An experimental consequence of this theoretical finding is an extreme sensitivity of the shape transformations to the actual trajectory in the phase diagram, i.e. from minute details in the preparation.

### 3.10.5. Membranes in electric fields

Shape transformations can also be induced by the action of an electric field. Strong fields lead to electroporation of the membrane (Crowley 1973, Dimitrov 1984, Winterhalter and Helfrich 1987, Needham and Hochmuth 1989), and electrofusion of vesicles and cells (Zimmermann 1982, Neumann *et al.* 1989, Chang *et al.* 1992). Work on the geometrical aspects of vesicles in moderate fields is scarce. Small fields lead to deformations of vesicles (Bryant and Wolfe 1987, Kummrow and Helfrich 1991, Hyuga *et al.* 1991a, b, Peterson 1992, Niggemann *et al.* 1995). Electroosmosis can lead to self-propulsion of vesicles if a non-uniform distribution of ion pumps can be maintained (Lammert *et al.* 1996). Non-rigid vesicles will then suffer significant deformation.

### 3.11. Shape changes induced by optical tweezers

A very promising new technique used to induce and study shape transformations has recently been developed using optical tweezers. The action of a laser spot on a bilayer causes quite dramatic shape changes. Three different geometries have been studied so far. (i) Cylindrical vesicles, as shown in figure 7, develop a propagating peristaltic mode which may finally transform the cylinder into a string of pearls (Bar-Ziv and Moses 1994). (ii) Flaccid prolate vesicles become more round and may even rupture, thus expelling enclosed smaller vesicles (Bar-Ziv *et al.* 1995a). (iii) The separation profile of two parallel bilayers pinched together locally by the tweezer develops a characteristic bulge away from the trap (Bar-Ziv *et al.* 1995b).

The physical mechanism behind these phenomena is not yet completely understood. One effect of the laser seems to be the creation of a lateral tension in the membrane due to the dielectric effect. In the frequency range studied, lipid is optically denser than water. Thus it gets attracted to the region of higher fields. A typical lateral tension can be estimated to be of the order of  $10^{-3}$  erg cm<sup>2</sup> (Nelson *et al.* 1995).

The pearlizing instability can be quantitatively explained as a modified Rayleigh instability induced by such a tension as discussed in sect. 7.6. The rounding of vesicles can be understood qualitatively by recognizing that the laser decreases the area of the vesicle, thus increasing the reduced volume. A subtle role, however, is played by the area pulled out of thermal fluctuations for which a quantitative description will have to use the concept of effective tension, as developed in section 4.2. So far, rupture of the membrane cannot be understood quantitatively by using accepted values for the line tension of a hole (Bar-Ziv *et al.* 1995a). The local pinching of membranes can be related to focal adhesion, as discussed in section 6.7.

## 4. Fluctuations

The shape of lowest energy discussed so far does not include any effect from thermal fluctuations. For phospholipid membranes, these fluctuations, which reflect the remarkable softness of the membrane, are usually not large enough to invalidate the notion of a well-defined mean shape. Experimentally, these fluctuations can be

analysed by video microscopy. A severe restriction arises from the fact that only contour fluctuations in the focal plane are visible. Therefore, only fluctuations around a spherical mean shape from which the bending rigidity can be extracted are relatively easy to investigate.

Fluctuations around non-spherical shapes, however, are difficult to analyse because rotational diffusion of the shape leads to a drifting focal plane. Reconstruction of the 3D fluctuations from such a 2D fluctuating contour has not yet been feasible. Rotational diffusion can be prevented by weak adhesion. Thus, the fluctuations of adhering red blood cells modelled as discocytes with shear elasticity (Peterson *et al.* 1992, Strey *et al.* 1995) and prolates (Döbereiner 1995, Döbereiner *et al.* 1995) have been analysed.

Theoretically, thermal fluctuations around a non-spherical shape of lowest energy can be calculated by expanding the curvature energy about this shape. Due to the presence of the geometrical constraints, such an expansion is not entirely straightforward. Peterson in a series of studies addressed this problem first for the spontaneous curvature model (Peterson 1985a, b, c) and later for the bilayer coupling model (Peterson *et al.*, 1992, Peterson 1992) applying it in both cases to discocytes. Within an alternative scheme all variants of the curvature model can be treated on an equal footing (Seifert 1995a). This approach allows us to elucidate the crucial role of the constraints in a more transparent way.

The area constraint restricts fluctuations. This effect can be attributed somewhat phenomenologically to an ‘effective’ or ‘entropic’ tension (Helfrich and Servuss 1984, Milner and Safran 1987, David and Leibler 1991). The small-scale fluctuations create an entropic tension for the large-scale deformations since they all have to share the fixed total area of a vesicle. For quasi-spherical vesicles such a tension was measured by an ingenious experimental set-up using aspirated vesicles (Evans and Rawicz 1990). A precise quantification of this effective tension and a prescription for how to calculate it for a non-spherical mean shape has also been given (Seifert 1995a).

The discussion starts in section 4.1 with fluctuations around a non-spherical mean shape. The emphasis will be on the role of the constraints and on symmetry considerations which help us to understand some qualitative properties of fluctuations and the stability of axisymmetric shapes (Seifert 1995a). The basic expansion parameter for thermal fluctuations is the ratio  $T/\kappa$ , which is considered to be small. Such an expansion breaks down in two limits. If a bifurcation or instability is approached, one of the shape modes becomes soft. This case has (somewhat prematurely) been discussed in section 3.9.2 above for the budding instability. The expansion in  $T/\kappa$  also breaks down in the spherical limit, where with the quantity  $1 - \nu$  another small parameter enters. Section 4.2 is devoted to the spherical limit and gives a critical assessment of the current theoretical approaches.

For vesicles with a very small bending rigidity, the notion of Gaussian fluctuations around a well-defined mean shape breaks down. These strongly fluctuating objects can be investigated by Monte Carlo simulations as briefly reviewed in section 4.3.

#### 4.1. Gaussian fluctuations with constraints

##### 4.1.1. Mode expansion

Fluctuations around a locally stable shape  $\mathbf{R}_0(s_1, s_2)$  can be parametrized by

$$\mathbf{R}(s_1, s_2) = \mathbf{R}_0(s_1, s_2) + \epsilon(s_1, s_2)\mathbf{n}(s_1, s_2), \quad (4.1)$$

where  $\mathbf{n}(s_1, s_2)$  is the local normal vector. The quantities of interest are both the thermal shift of the mean shape  $\langle \epsilon(s_1, s_2) \rangle$ , which does not vanish because of the constraints, and correlation functions like  $\langle \epsilon(s_1, s_2) \epsilon(s'_1, s'_2) \rangle$ . The bracket  $\langle \dots \rangle$  denotes the appropriate thermal average defined below.

The local normal displacement  $\epsilon(s_1, s_2)$  is expanded in a set of basis functions  $\{\epsilon_i\}$  as

$$\epsilon(s_1, s_2) = \sum_i a_i \epsilon_i(s_1, s_2). \quad (4.2)$$

For axisymmetric vesicles, the spherical harmonics

$$\epsilon_i(s_1, s_2) \equiv Y_{l,m}(s\pi/s^*, \phi), \quad (4.3)$$

with  $a_{l,-m} = (-1)^m a_{l,m}^*$ , are a convenient basis (Peterson 1985a, b). Here,  $s^*$  is the length of the contour from north pole to south pole. The formal index  $i$  has thus become a double index  $(l, m)$  and the  $\sum_i$  runs to some cut-off  $l_{\max}$ . The expansion based on (4.2) and (4.3) can deal with any axisymmetric stationary shape, whether it is star-shaped or not. In particular, this expansion is not restricted to nearly spherical shapes.

We will first consider the fluctuations in the BC model, the other cases then becoming trivial modifications. The geometrical quantities area, volume, mean curvature, as well as the bending energy  $G$ , can be expanded in the set  $\{a_i\}$ . Formally, one thus obtains

$$G = G_0 + g_i a_i + (1/2) a_i G_{ij} a_j + O(a_i^3), \quad (4.4)$$

$$A = A_0 + R_0^2 [d_i^{(1)} a_i + (1/2) a_i D_{ij}^{(1)} a_j + O(a_i^3)], \quad (4.5)$$

$$V = V_0 + R_0^3 [d_i^{(2)} a_i + (1/2) a_i D_{ij}^{(2)} a_j + O(a_i^3)], \quad (4.6)$$

and

$$M = M_0 + R_0 [d_i^{(3)} a_i + (1/2) a_i D_{ij}^{(3)} a_j + O(a_i^3)], \quad (4.7)$$

with summation over double indices implied.

Specifically for axisymmetric vesicles, the quantities  $g_i$ ,  $G_{ij}$ ,  $d_i^\alpha$  and  $D_{ij}^\alpha$  can be expressed as integrals over the contour. The integrands are quantities such as the local curvature and Legendre polynomials and derivatives thereof.

Thermal expectation values  $\langle h\{a_i\} \rangle$  are now defined as

$$\langle h\{a_i\} \rangle \equiv \frac{1}{Z} \int \mathcal{D}\{a_i\} \delta\left(\frac{A - A_0}{R_0^2}\right) \delta\left(\frac{V - V_0}{R_0^3}\right) \delta\left(\frac{M - M_0}{R_0}\right) \exp\left[\frac{-\kappa(G - G_0)}{T}\right] h\{a_i\}, \quad (4.8)$$

where the partition function  $Z$  ensures proper normalization ( $\langle 1 \rangle = 1$ ).

The crucial issue is to define the measure  $\mathcal{D}\{a_i\}$ , which should physically correspond to an integration over all surfaces close to the stationary shape, not counting any surface twice and keeping the numbers of degrees of freedom constant.

Both non-trivial requirements can be satisfied by introducing a Fadeev–Popov and a Liouville factor, respectively (Nelson and Powers 1993, Cai *et al.* 1994). Fortunately, these subtleties are absent in lowest order  $T/\kappa$ , and one can use just a naive measure for calculating the correlation functions (Seifert 1995a). Moreover, one has to exclude also the Euclidean rotation and translation modes (Peterson 1985b).

#### 4.1.2. Correlation functions and effective tension

We discuss here the explicit expressions for the correlation function  $\langle a_i a_j \rangle$  because it provides an important conclusion about the similarities and differences of fluctuations and stability in the different variants of the curvature model, or for different values of  $\alpha$  within the ADE model.

After replacing the  $\delta$  functions in (4.8) by Fourier integrals, the correlation functions can be shown to read (Seifert 1995a)

$$\langle a_i a_j \rangle = \frac{T}{\kappa} \left( S_{ij}^{-1} - d_k^\alpha S_{ik}^{-1} W^{\alpha\beta} S_{jl}^{-1} d_l^\beta \right). \quad (4.9)$$

The matrix elements  $S_{ij}$  of the *stability matrix*

$$S_{ij} \equiv G_{ij} + \lambda^\alpha D_{ij}^\alpha \quad (4.10)$$

are obtained from the second variation of both the curvature energy and the geometrical constraints. The matrix elements

$$W^{\alpha\beta} \equiv d_i^\alpha S_{ij}^{-1} d_j^\beta \quad (4.11)$$

belong to a  $3 \times 3$  matrix with respect to the Greek indices.

General insight is gained by first classifying the set of modes  $\{\epsilon_i\}$  according to their symmetry properties. Modes that break a symmetry of the stationary shape are called *symmetry-breaking modes*. For an axisymmetric vesicle, all modes with index  $m \neq 0$  are symmetry-breaking. If, moreover, the stationary shape possesses reflection symmetry, the modes with  $m = 0$  and  $l$  uneven belong to this class, too. By symmetry, the first variation in the geometrical quantities and the bending energy vanishes identically for these modes, i.e.,  $d_i^\alpha = g_i = 0$ . The remaining *symmetry-preserving modes* do not change the symmetry of the mean shape and will thus, in general, have linear terms  $d_i^\alpha \neq 0$  and  $g_i \neq 0$ .

The stability matrix  $S_{ij}$  factors in these two classes and, moreover, within each class in different subclasses according to the symmetry of the respective modes. In particular, for an axisymmetric mean shape with reflection symmetry, the modes with different index  $|m|$  do not mix, and neither do those with different parity but the same  $|m|$ . Therefore, one can discuss the correlations of these two classes of modes separately.

For the *symmetry-breaking modes*, the simple result

$$\langle a_i a_j \rangle = \frac{T}{\kappa} S_{ij}^{-1} \quad (4.12)$$

for the correlation function is remarkable for the following reason. As pointed out in Seifert (1995a), the correlation function in the  $\Phi$  ensemble (3.1) in which the terms

$\Sigma A + PV + QM$  count as ‘real’ energy assuming that the ‘fields’  $\Sigma$ ,  $P$  and  $Q$  are external parameters, is the same as (4.12) since the stability matrix  $S_{ij}$  is simply the second variation of the energy  $\Phi$ , as follows from (4.10). Thus, the correlations of all symmetry-breaking modes do not depend on whether one imposes hard constraints or whether one considers the terms  $\Sigma A + PV + QM$  as contributing to the energy. For all symmetry-breaking fluctuations the Lagrange multiplier  $\Sigma$  thus acts exactly like a tension. This statement is non-trivial since the constraint on fluctuations has not been implemented by this Lagrange multiplier but rather by an exact  $\delta$  function. The equivalence of the fluctuations in the BC model and the  $\Phi$  ensemble is not complete since for all modes which preserve the symmetry, i.e. in particular, for fluctuations of the contour of an axisymmetric vesicle, the additional term in (4.9) shows that fluctuations in the constrained ensemble are different from those where the  $\Sigma A + PV + QM$  terms are treated as a real energy.

The correlation functions in the ADE model and SC model can be obtained similarly (Seifert 1995a). For the ADE model, the result (4.9) still holds after the replacement

$$S_{ij} \rightarrow S_{ij} + \alpha d_i^{(3)} d_j^{(3)}, \quad (4.13)$$

with Greek indices running only through 1 and 2. Since  $d_i^{(3)} = 0$  for all symmetry-breaking modes, the correlation functions for these modes are again identical to those in the BC model. The difference between the various ensembles shows up only in the correlations involving symmetry-preserving modes.

Numerical results of modes and fluctuation spectra are available only for discocyte-like shapes (Peterson *et al.* 1992). In this study, space-dependent thickness fluctuations of red blood cells were analysed using both the BC and the SC models taking into account shear elasticity as a further ingredient. Since thickness fluctuations do not break a symmetry, the results for the two cases are different. The experimental data were in between the two models thus supporting the interpolating ADE model.

#### 4.1.3. Stability

Any approach which yields fluctuations around a shape will also detect an instability of this shape. Peterson has used his scheme to investigate the stability of oblates in the spontaneous curvature model (Peterson 1985b, 1992). The scheme discussed above has been used to address the stability of prolates and oblates within the ADE model (Jaric *et al.* 1995). As a corollary to the above-discussed independence of symmetry-breaking fluctuations from  $\alpha$ , one should also note that an instability of a shape towards a deformation that breaks a symmetry of this shape does not depend on the variant of the curvature model or the value of  $\alpha$ . It is rather a property of the shape (Seifert 1995a). This statement does not hold for instabilities that preserve the symmetry. An example are the pears with the weak asymmetry, which are unstable for small  $\alpha$  and become stable for larger  $\alpha$ , as discussed in section 3.3.

#### 4.1.4. Thermal shift of the mean shape

The modes that do not break a symmetry of the stationary shape acquire a finite temperature shift to make up for the area—and, strictly speaking, also for the

volume and the mean curvature—stored in the fluctuating modes. This shift reads (Seifert 1995a)

$$\langle \mathbf{R}(s_1, s_2) \rangle = \mathbf{R}_0(s_1, s_2) + \sum_i \langle a_i \rangle \epsilon_i(s_1, s_2) \mathbf{n}(s_1, s_2). \quad (4.14)$$

with

$$\langle a_i \rangle = -\frac{1}{2} \frac{T}{\kappa} d_k^\alpha W^{-1}{}^{\alpha\beta} D_{mn}^\beta (2S_{kn}^{-1} C_{mi} + S_{ki}^{-1} C_{mn}). \quad (4.15)$$

The latter relation holds only if Liouville factors arising from measure corrections are irrelevant (Cai *et al.* 1994), which has not yet been proven.

For an axisymmetric vesicle, the thermal shift can be reduced to a shift of the mean contour, since  $\sum_i$  includes contributions from the ( $m = 0$ ) modes only. The thermal shift is of order  $T/\kappa$  and thus much smaller than a typical fluctuation, which scales as  $|a_i| \sim (T/\kappa)^{1/2}$ .

#### 4.1.5. Spherical limit

As the mean shape around which the expansion has been performed approaches the sphere, the fluctuations should become smaller since for a sphere as a  $T = 0$  shape, there is no area available for fluctuations at constant volume. In the approach outlined above, the modes with different  $l$  no longer mix in this limit. Therefore, the correlation matrix is given by the inverse of the stability matrix  $S_{ij}$ , which becomes in the spherical limit

$$\langle |a_{l,m}|^2 \rangle \approx \frac{T}{\kappa} \frac{1}{(l+2)(l-1)(l^2+l-6)} \quad (4.16)$$

for all variants of the curvature model.

This expression diverges for the  $l = 2$  mode, which points to an inconsistency. In fact, in the spherical limit another small parameter,  $1 - \nu$ , arises which invalidates the naive expansion in  $T/\kappa$ .

## 4.2. Quasi-spherical vesicles

### 4.2.1. Expansion around the sphere

The spherical limit has to be analysed using a different approach, which allows us to keep track of both small parameters,  $\nu$  and  $1 - \nu$ . The fluctuating shape is not expanded around the corresponding stationary shape but rather around a sphere with the same volume

$$V \equiv \frac{4\pi}{3} R_\nu^3, \quad (4.17)$$

which defines  $R_\nu$ . We consider a fixed area

$$A \equiv (4\pi + \Delta) R_\nu^2, \quad (4.18)$$

which defines the (dimensionless) excess area  $\Delta$  used traditionally as a small parameter instead of  $1 - \nu$ .

A quasi-spherical vesicle can be parametrized by spherical harmonics

$$R(\theta, \phi) = R_V \left[ 1 + \sum_{l \geq 2}^{l_{\max}} \sum_{m=-l}^l u_{l,m} Y_{lm}(\theta, \phi) \right], \quad (4.19)$$

where  $|m| \leq l$  and  $u_{l,-m} = (-1)^m u_{l,m}^*$ . Expanding the geometrical quantities as well as the bending energy around a sphere, one has (Helfrich 1986, Milner and Safran 1987, Ou-Yang and Helfrich 1989)

$$G = 8\pi + \frac{1}{2} \sum_{l \geq 1}^{l_{\max}} \sum_{m=-l}^l |u_{l,m}|^2 (l+2)(l+1)l(l-1) + O(|u_{l,m}|^3), \quad (4.20)$$

$$A = R_V^2 \left\{ 4\pi \left[ 1 + \frac{u_{0,0}}{(4\pi)^{1/2}} \right]^2 + \sum_{l \geq 1}^{l_{\max}} \sum_{m=-l}^l |u_{l,m}|^2 [1 + l(l+1)/2] + O(|u_{l,m}|^3) \right\}, \quad (4.21)$$

and

$$V = R_V^3 \left\{ \frac{4\pi}{3} \left[ 1 + \frac{u_{0,0}}{(4\pi)^{1/2}} \right]^3 + \sum_{l \geq 1}^{l_{\max}} \sum_{m=-l}^l |u_{l,m}|^2 + O(|u_{l,m}|^3) \right\}. \quad (4.22)$$

The volume constraint (4.17) fixes the amplitude  $u_{0,0}$  as a function of the other amplitudes

$$u_{0,0} = - \sum_{l \geq 1}^{l_{\max}} \sum_{m=-l}^l |u_{l,m}|^2 / (4\pi)^{1/2}, \quad (4.23)$$

where cubic terms have been truncated. If the relation (4.23) is inserted into (4.21), the area constraint (4.18) becomes

$$\sum_{l \geq 2}^{l_{\max}} \sum_{m=-l}^l |u_{l,m}|^2 \frac{(l+2)(l-1)}{2} = A \quad (4.24)$$

The sum starts with  $l = 2$  since the ( $l = 1$ ) modes correspond to translations.

#### 4.2.2. Exact treatment of the area constraint

The crucial problem is to incorporate the area constraint (4.24). In fact, one can calculate the correlation functions of the quasispherical modes treating the area constraint exactly by a  $\delta$  function (Seifert 1995a). The resulting 1D complex integral has to be analysed numerically. Two limiting cases, however, can be isolated analytically.

For  $T/\kappa \ll A$ , one obtains

$$\langle |u_{l,m}|^2 \rangle = \frac{T}{\kappa} \left[ \frac{1}{(l+2)(l-1)(l^2+l-6)} + O(\tau) \right] \quad (4.25)$$

for  $l \geq 3$ , and

$$\langle |u_{l,m}|^2 \rangle = \frac{4}{5} \left[ \frac{1}{2} - \tau \sum_{l \geq 3} \frac{2l+1}{(l+2)(l-1)(l^2+l-6)} + O(\tau^2) \right] \quad (4.26)$$

for  $l = 2$ . Here,

$$\tau \equiv \frac{T}{\kappa A} \quad (4.27)$$

is the expansion parameter.

The leading term for  $l \geq 3$  corresponds to the result found in section 4.1.5 in the spherical limit. Thus, the direct evaluation of the correlation functions in the spherical limit shows that the expansion performed in section 4.1 corresponds (for  $l \geq 3$ ) to the double limit  $A \rightarrow 0$  after  $\tau \rightarrow 0$ . As the leading term for the amplitude for the ( $l = 2$ ) modes shows, these modes pick up most of the excess area. Of course, the distribution of this area among the five ( $l = 2$ ) modes cannot be obtained in the quadratic approximation. Note also that the area constraint is obeyed exactly, as the second-order contribution in (4.26) shows.

In principle, one could continue the expansions (4.25) and (4.26) to higher order in  $\tau$ . However, this would lead to misleading results since the terms which have been omitted in the quadratic expansions (4.20)–(4.22) are more relevant than those higher-order terms (Seifert 1995a).

For  $A \ll T/\kappa$ , all modes shape the available excess area equally, which leads to (Milner and Safran 1987, Seifert 1995a)

$$\langle |u_{l,m}|^2 \rangle \approx \frac{2A}{N(l+2)(l-1)}. \quad (4.28)$$

In summary, an analytical calculation of the fluctuations of quasi-spherical vesicles taking into account the area constraint exactly is possible for large and small  $\tau$ . An expansion beyond the leading term for small  $\tau$  does not fail due to the absence of an analytical scheme but rather due to the relevance of the higher-order terms in the expansions (4.20)–(4.22).

#### 4.2.3. Conventional approach with effective tension

The conventional approach to fluctuations in the quasi-spherical limit (Schneider *et al.* 1984b, Milner and Safran 1987, Faucon *et al.* 1989) contains two approximations. First, in these works the relevance of the higher-order terms in the expansions (4.20)–(4.22) are tacitly neglected. Therefore, this approach inevitably suffers from the same deficiencies as the exact approach in this respect. Secondly, the area constraint is not treated exactly by a  $\delta$  function but rather by a Lagrange multiplier.

We discuss this approach here for the minimal model since the other variants lead to the same result. The mean-square amplitudes in this approach are calculated with the Boltzmann factor

$$\exp [-(\kappa G + \bar{\Sigma} A)/T], \quad (4.29)$$

where the ‘tension’  $\bar{\Sigma}$  is another, yet free, Lagrangian multiplier to be distinguished by the overbar from the Lagrange multiplier  $\Sigma$  used in calculating the stationary shape. After inserting the quadratic expansions (4.20)–(4.22) into energy and area, with  $u_{0,0}$  replaced by the volume constraint (4.23), one obtains

$$\kappa G + \bar{\Sigma} A \approx \text{const} + \frac{\kappa}{2} \sum_{l \geq 2}^{l_{\max}} \sum_{m=-l}^l |u_{l,m}|^2 (l+2)(l-1)[(l+1)l + \bar{\sigma}], \quad (4.30)$$

with the dimensionless effective tension

$$\bar{\sigma} \equiv \bar{\Sigma} R_V^2 / \kappa. \quad (4.31)$$

If this expression is used as a Boltzmann weight for the amplitudes  $\{u_{l,m}\}$ , one immediately obtains the mean square amplitudes (Milner and Safran 1987)

$$\langle |u_{l,m}|^2 \rangle = \frac{T}{\kappa} \frac{1}{(l+2)(l-1)[(l+1)l + \bar{\sigma}]}. \quad (4.32)$$

These expressions for the mean-square amplitudes have been used to determine experimentally the bending rigidity  $\kappa$  from the contour fluctuations of quasi-spherical vesicles using phase contrast microscopy combined with fast image processing (Schneider *et al.* 1984b, Engelhardt *et al.* 1985, Bivas *et al.* 1987, Faucon *et al.* 1989, Duwe *et al.* 1990, Meleard *et al.* 1992, Niggemann *et al.* 1995). In this approach,  $\bar{\sigma}$  is usually either set to 0 or treated as a fit parameter for which one typically obtains values in the range  $0 \lesssim \bar{\sigma} \lesssim 100$ .

Since the Lagrangian multiplier  $\bar{\Sigma}$  has been introduced only to enforce the area constraint, it should, in fact, be eliminated in favour of the excess area  $\Delta$  which is the physically meaningful quantity. Inserting the mean-square amplitudes (4.32) into the expansion of the area and comparing with the constraint (4.32) yields an implicit equation (Bivas *et al.* 1992, Seifert 1995a),

$$\sum_{l \geq 2}^{l_{\max}} \frac{2l+1}{l^2 + l + \bar{\sigma}(\Delta)} = \frac{2\Delta\kappa}{T} = \frac{2}{\tau}, \quad (4.33)$$

for  $\bar{\sigma}$ . An analogous relation was first derived for almost planar membranes (Helfrich and Servuss 1984). The relation (4.33) shows that  $\bar{\sigma}$  depends on the excess area only in the combination  $\Delta\kappa/T = 1/\tau$ . Thus, after elimination of the effective tension, the mean-square amplitudes as given by (4.32) depend only on the three quantities,  $T/\kappa$ ,  $\tau$  and the cut-off  $l_{\max}$ . The experimental study (Haeckl *et al.* 1995) shows the principal feasibility of replacing the tension in favour of the temperature-dependent excess area.

In general, (4.33) has to be inverted numerically to yield  $\bar{\sigma} = \bar{\sigma}(\tau, l_{\max})$ . It is instructive to discuss limit cases analytically. For small  $\tau$ , one finds

$$\bar{\sigma} \approx -6 + \frac{5}{2}\tau + O(\tau^2). \quad (4.34)$$

Inserting this value into (4.32), one recovers the exact limits (4.25) and (4.26). However, the next-to-leading-order terms in an expansion in  $\tau$  of either (4.32) or (4.25) do *not* coincide. This result shows that treating the area term by a  $\delta$  constraint is, in principle, different from including it by a Lagrange multiplier.

The fact that the effective tension is negative for small  $\tau$  may look strange at first sight, but becomes clear in view of the relation (3.3). In fact,  $\Sigma R_0^2 / \kappa = -6$  is also the spherical limit of the (dimensionless) Lagrangian multiplier for prolate and oblate

ellipsoids. The effective tension for fluctuations is negative, thus promoting fluctuations, because if area is taken up by the fluctuations with  $l \geq 3$ , the curvature energy stored in the ( $l = 2$ ) modes decreases. For  $l \geq 3$ , the fluctuations with area constraint are thus larger than those without an area constraint, which shows again that one should interpret the effective tension quite carefully.

For large  $\tau$ , one obtains from (4.33)

$$\bar{\sigma} \approx \frac{\tau}{2} l_{\max}^2, \quad (4.35)$$

which after insertion into the mean-square amplitudes again coincides with the exact limit (4.28).

If the inversion of (4.33) is performed analytically by replacing the sum with an integral, one obtains the exponential dependence of the tension on the excess area:

$$\bar{\sigma} \approx \frac{l_{\max}^2 + l_{\max} - 6 \exp(2/\tau)}{\exp(2/\tau) - 1}. \quad (4.36)$$

For intermediate values of  $\tau$  in the range  $2 \gg \tau \gg 1/\ln l_{\max}$ , one thus finds

$$\bar{\sigma} \approx l_{\max}^2 \exp(-2/\tau). \quad (4.37)$$

Such an exponential dependence of the effective tension from the excess area was first discussed for almost planar membranes (Helfrich and Servuss 1984). It has been verified experimentally by micropipette aspiration of vesicles (Evans and Rawicz 1990).

The consistency of this approach, where the area constraint is treated by a Lagrangian multiplier can be checked by calculating the fluctuations in the dimensionless excess area (Seifert 1995a). It turns out that only for small excess area, the fluctuations show the  $\sim 1/\sqrt{N}$  behaviour characteristic of large systems where  $N \sim l_{\max}^2$  (Seifert 1995a). The two approaches have also been compared by a Monte Carlo simulation in a quite narrow  $\tau$  range for  $l_{\max} = 20$  (Bivas *et al.* 1992). As important a comparison between the exact and the conventional approach may be, one should always keep in mind that neglecting higher-order terms in the expansions (4.20)–(4.22) adds additional errors of the order  $\tau$ . To include those effects would require an expansion in (4.20)–(4.22) beyond the quadratic order (Ou-Yang and Helfrich 1989).

#### 4.3. Monte Carlo simulations of very flexible vesicles

The concept of a mean vesicle shape with small fluctuations around it breaks down if the bending rigidity is so small that the persistence length (2.17) becomes comparable with the vesicle size. While for pure phospholipid vesicles only vesicles of astronomical size would meet this requirement, vesicles consisting of mixed membranes can have significantly smaller persistence length, thus exhibiting strong fluctuations (Duwe *et al.* 1990). Unfortunately, a small bending rigidity usually implies higher solubility and thus less integrity of the membrane so that one may question the experimental realizability of a strongly fluctuating vesicle of both fixed area and fixed topology.

Leaving these experimental reservations aside, it is a theoretically challenging problem to investigate the behaviour of vesicles in the limit of small bending rigidity. In this regime, analytical methods are replaced by Monte Carlo simulations augmented with scaling arguments.

#### 4.3.1. Two-dimensional ‘vesicles’

Fisher and co-workers in a series of papers (Leibler *et al.* 1987, Camacho and Fisher 1990, Maggs *et al.* 1990, Camacho and Fisher 1991) investigated 2D vesicles which would more appropriately be called stiff ring-polymers. In the limit of large bending rigidity, 2D vesicles show only one (elliptical) branch of shapes (Seifert 1991a). The two dimensions support neither a non-trivial spontaneous curvature nor budding since there is only one radius of curvature which necessarily leads to a diverging bending energy for necks. As Monte Carlo simulations for small bending rigidity show, a broken symmetry stomatocyte-like shape is stabilized by the self-avoidance of the membrane (Leibler *et al.* 1987). In the limit of zero bending rigidity, the shape becomes a closed self-avoiding random walk. A finite pressure difference between the inside and the outside pushes this shape either towards a collapsed branched polymer configuration (Camacho and Fisher 1990) or towards an extended shape (Maggs *et al.* 1990) whose circumference corresponds to a stretched polymer (Pincus 1976) depending on the sign of the pressure.

#### 4.3.2. Three-dimensional vesicles

Corresponding studies of 3D highly flexible vesicles require significantly larger conceptual and numerical effort. Firstly, one has to find a suitable representation of such a vesicle by a tethered surface consisting of beads with connecting bonds or tethers. Secondly, the fluidity of this membrane is ensured by a dynamical bond flip algorithm (Boulatov *et al.* 1986, Billoire and David 1986, Ho and Baumgärtner 1990). For vanishing bending rigidity, vesicle configurations correspond to those of branched polymers if the enclosed volume can fluctuate freely (Kroll and Gompper 1992, Boal and Rao 1992a). A finite pressure difference between interior and exterior leads through a phase transition to a more extended spherical shape whose surface consists of crumpled ‘blobs’ of membrane patches with non-trivial scaling properties (Gompper and Kroll 1992a, b).

For finite but small bending rigidity, simulations show the renormalization of the bending rigidity according to (2.18). (Gompper and Kroll 1994, 1995b). Contact with the shapes as calculated with shape equations has been made for larger bending rigidity which leads to prolates and stomatocytes. The transition between these shapes is fundamentally different from the transition at small bending rigidity. The latter one is a true thermodynamic phase transition with an activation barrier that grows with the size of the vesicle while the former is a transition between two shapes with a finite activation barrier.

Monte Carlo simulations have also been used to investigate the shape changes of vesicles in elongational flow (Gompper and Kroll 1993) and the forced flow of vesicles through narrow pipettes (Gompper and Kroll 1995a).

## 5. Vesicles of non-spherical topology

Topology has not yet played any role in this investigation since, as argued in the introduction, topological changes seem not to occur on the experimentally accessible

time scales. Still, vesicles of non-spherical topology do exist if the bilayer sheet closes in this topology during the poorly understood swelling process. In fact, shapes of vesicles of toroidal topology have been predicted theoretically (Ou-Yang 1990, Seifert 1990, 1991c) and, at the same time, toroidal vesicles have been found independently in experiments (Mutz and Bensimon 1991). While one may first suppose that the different topology does not play any significant role, quite the contrary is true. For vesicles with more than one handle or hole, i.e. for genus  $g \geq 2$ , the ground state can be degenerate. The reason for this degeneracy is the conformal invariance of the curvature energy, which has non-trivial consequences only for  $g \geq 2$ , even though this invariance is a general property that is not restricted to any topology. Based on this invariance, it was theoretically predicted (Jülicher *et al.* 1993a) that these vesicles should exhibit a novel diffusion process in shape-space called conformal diffusion, which has recently been found experimentally (Michalet 1994, Michalet and Bensimon 1995b).

The following three sections are devoted to the mathematical notions that are used for the theoretical description of these phenomena. In section 5.1, we discuss conformal invariance of the curvature energy. In section 5.2, Willmore surfaces and the Willmore problem are defined and discussed for each topological class. The role of the geometrical constraints under conformal transformations is derived in section 5.3. Based on these concepts, in sections 5.4, 5.5 and 5.6, the theoretical predictions for vesicles of genus 1, genus 2, and higher genus, respectively, are presented. Each of these sections contains a discussion of the experimental data available at present.

### 5.1. Conformal invariance of the local curvature energy

The central concept necessary for understanding the new features of vesicles of non-spherical topology is the conformal invariance of the local curvature energy  $G$  (2.51), which is a stronger property than the scale invariance referred to in section 3.1.2. While the conformal invariance of  $G$  has been known to mathematicians for a long time (Thomsen 1924), it has entered the physical literature on vesicles only recently (Duplantier 1990, Duplantier *et al.* 1990). Conformal transformations in three dimensions comprise a ten-parameter group, which consists of translations (three parameters), rotations (three parameters) and scale transformations (one parameter), all of which do not change the shape in any non-trivial fashion. The non-trivial conformal transformations are the inversions in a sphere which map  $\mathbf{R}$  to  $\mathbf{R}'$  with

$$\mathbf{R}' = \mathbf{R}_0 + (\mathbf{R} - \mathbf{R}_0)/(\mathbf{R} - \mathbf{R}_0)^2. \quad (5.1)$$

The centre  $\mathbf{R}_0$  of the sphere yields the remaining three parameters. The local quantity  $(H^2 - K) dA$  is invariant under conformal transformation in three dimensions as can be shown by inserting the mapping (5.1) (for  $\mathbf{R}_0 = \mathbf{0}$ ) into the expression given in section 2.1 for  $H$ ,  $K$  and  $dA$ , respectively. Since the topology of a closed surface and thus of  $\oint dA K$  does not change under a conformal transformation, the energy  $G$  is, in fact, a conformal invariant.

Rather than using inversions, it is more convenient for many applications to work with special conformal transformations. Such a transformation consists of an inversion in a unit sphere at the centre of origin  $\mathbf{R} \rightarrow \mathbf{R}/R^2$ , a translation by a vector  $\mathbf{a}$  and another inversion in a unit sphere at the centre of origin. Every point  $\mathbf{R}$  is thus transformed to  $\mathbf{R}'$ , with

$$\mathbf{R}' = \frac{\mathbf{R}/R^2 + \mathbf{a}}{(\mathbf{R}/R^2 + \mathbf{a})^2}. \quad (5.2)$$

Two successive special conformal transformations (5.2) with translation vectors  $\mathbf{a}_1$  and  $\mathbf{a}_2$  are equivalent to one special conformal transformation with  $\mathbf{a} = \mathbf{a}_1 + \mathbf{a}_2$ , i.e., the special conformal transformations form a commutative three-parameter subgroup. Since for  $\mathbf{a} \rightarrow 0$ , the special conformal transformation becomes the identity, an expansion in  $\mathbf{a}$  is feasible, which is the main advantage of using special conformal transformations.

### 5.2. Willmore surfaces and the Willmore problem

Willmore surfaces are defined as the stationary points of the curvature energy  $G$ , i.e. a shape is a Willmore surface if it obeys  $\delta^1 G = 0$  (Willmore 1982, Pinkall and Sterling 1987). If the surface is free of self intersections, it is called embedded. The Willmore problem consists of finding the embedded Willmore surface  $S_g$  of lowest energy  $G$  for any given genus  $g$  irrespective of any further constraints, i.e. in finding the absolute minimum of  $G$  for given topology (Willmore 1965, 1982). For any shape  $S_g$  that is a solution to this problem, all conformal transformations of  $S_g$  are solutions too.

#### 5.2.1. Genus 0

For spherical topology, one can prove that the sphere with  $G \equiv G_0 = 8\pi$  is the only embedded Willmore surface (Bryant 1984). Since spheres remain spheres under conformal transformations, the Willmore problem has a unique solution for spherical topology.

#### 5.2.2. Genus 1

For toroidal topology, there is as yet no definite answer to the Willmore problem. Willmore (1965, 1982) himself conjectured that the Clifford torus shown in figure 20 minimizes  $G$ . The Clifford torus is an axisymmetric torus, which can be parametrized by

$$\mathbf{R}(\theta, \phi) = \begin{pmatrix} (\sqrt{2} + \sin \theta) \cos \phi \\ (\sqrt{2} + \sin \theta) \sin \phi \\ \cos \theta \end{pmatrix}, \quad (5.3)$$

where  $0 \leq \theta, \phi \leq 2\pi$ . Its curvature energy is  $G = G_1 \equiv (\pi/2)8\pi$  and its reduced volume is  $\approx 0.71$ . Among the evidence for Willmore's conjecture is the fact that the Clifford torus is proven to be the shape of lowest  $G$  among all axisymmetric tori (Langer and Singer 1984).

Conformal transformations of the Clifford torus generate a one-parameter family of non-axisymmetric shapes. This can be seen by applying a special conformal transformation (5.2) to the Clifford torus as given by (5.3) (see figure 20 for an example). A special conformal transformation with vector  $\mathbf{a}(s) = (s \cos \phi, s \sin \phi, 0)$  generates a one-parameter family of non-axisymmetric shapes with varying reduced volume  $v_{cl} \leq v(s) < 1$ . This family of shapes can be described in a closed analytical form (Fourcade 1992). For  $s = 2^{1/4}\sqrt{\pi}/(\sqrt{2} + 1)$ , it ends up at a limit shape with  $v = 1$ , which consists of a sphere with an infinitesimal handle.

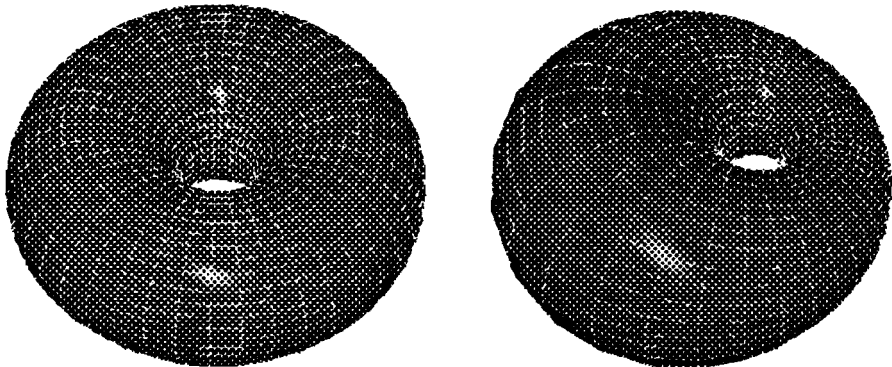


Figure 20. Clifford torus and a shape generated by a conformal transformation (Jülicher *et al.* 1993b).

A special conformal transformation with  $\mathbf{a} = (0, 0, a_Z)$  applied to the Clifford torus does not generate any new shape but is rather equivalent to a scale transformation due to the special ratio  $\sqrt{2}$  of the generating radii of the Clifford torus. In contrast, for a general axisymmetric toroidal shape with a reflection plane, a conformal transformation (5.2) with  $\mathbf{a} = (0, 0, a_Z)$  would generate a shape with broken up-down symmetry. Thus, even though the special conformal transformations involve the three parameters  $(a_X, a_Y, a_Z)$ , there is only a one-parameter family of special conformal transformations which produces new shapes when applied to the Clifford torus due to its special symmetry properties.

Apart from the Clifford torus, there are further embedded Willmore surfaces, but these turn out to be *unstable* stationary points of the functional  $G$  (Pinkall 1985, Kusner 1994).

### 5.2.3. Genus 2

For genus 2, the Willmore problem is solved tentatively by Kusner's (1989) conjecture, that the so-called Lawson surface shown in figure 21 is the shape of minimal curvature energy. The rationale behind Kusner's conjecture arises from a connection between minimal surfaces in  $S^3$ , which is the 3D unit sphere in  $R^4$ , and Willmore surfaces in  $R^3$ : any compact minimal surface in  $S^3$  becomes a Willmore surface when projected stereographically from  $S^3$  to  $R^3$ . The value of the curvature energy  $G$  is twice the respective area in  $S^3$  (Pinkall and Sterling 1987). The reverse does not hold: a Willmore surface in  $R^3$  does not need to be a minimal surface in  $S^3$ .

Lawson (1970) has found a whole family  $\xi_{m,k}$  (with  $m \geq k \geq 0$  and genus  $g = mk$ ) of minimal surfaces in  $S^3$  by first solving Plateau's problem for a certain geodesic quadrilateral in  $S^3$ . If the resulting surface is extended by reflections across its geodesic boundary arcs, a compact minimal surface  $\xi_{m,k}$  in  $S^3$  is obtained, which after projection to  $R^3$  yields a Willmore surface also called  $\xi_{m,k}$ . The Clifford torus is the particular member  $\xi_{1,1}$  while all  $\xi_{m,0}$  correspond to a sphere. The Lawson surface as shown in figure 21 is the member  $\xi_{2,1}$ , which has been shown to have a quite small area in  $S^3$  and which is thus a good candidate for Willmore's problem (Kusner 1989).

In general, there is no analytical description known for the minimal surfaces  $\xi_{m,k}$  in  $S^3$  and thus no explicit representation of the corresponding surface in  $R^3$ . However, there are surfaces  $\Xi_{m,k}$  in  $S^3$  which can be considered as approximations

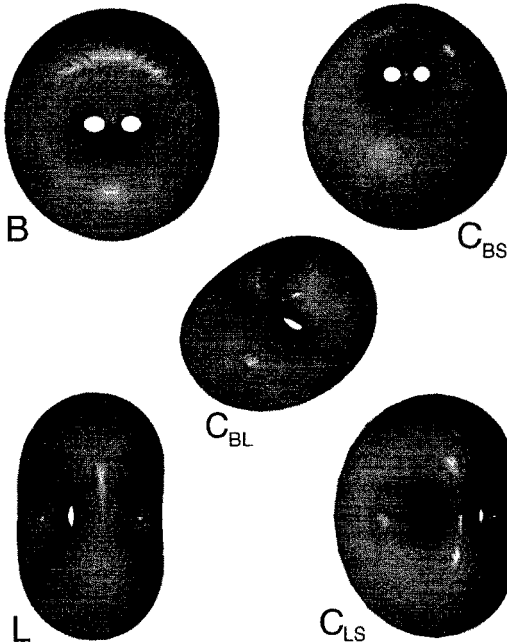


Figure 21. Lawson surface  $L$  and some shapes obtained by conformal transformations, including the 'button' surface  $B$ . The other labels refer to the phase diagram of figure 23 (Jülicher *et al.* 1993a).

to these minimal surfaces since they contain the same geodesic arcs. The surfaces  $\Xi_{m,k}$  are defined by (Lawson 1970)

$$\mathcal{I}(z^{m+1}) + |w|^{m-k} \mathcal{I}(w^{k+1}) = 0, \quad (5.4)$$

using the representation  $S^3 = \{(z, w), |z|^2 + |w|^2 = 1\}$  and  $z, w$  are complex numbers.

The Lawson surface as it is shown in figure 21 was obtained by first mapping the surface  $\Xi_{2,1}$  from  $S^3$  to  $R^3$  by a stereographic projection. The resulting shape was then triangulated and used as an initial shape for a further numerical minimization of  $G$  (Jülicher *et al.* 1993a). The shape thus obtained should be a close approximation to the Lawson surface. In fact, this algorithm yields the energy  $G = G_2 \simeq 1.75 \times 8\pi$  thus corroborating an earlier result (Hsu *et al.* 1992), for which a different algorithm (Brakke 1992) was used.

The Lawson surface has a threefold symmetry axis and a mirror symmetry plane perpendicular to this axis. Moreover, it is invariant under inversions at the centre. The conformal transformations of the Lawson surface comprise a three-parameter family of shapes. This family can be parametrized by the vector  $\mathbf{a}$  of the special conformal transformation which must be applied to the Lawson surface (centred at the origin) in order to generate this specific shape. The topology of this space  $\mathcal{W}$  of shapes is that of the Lawson surface itself, since whenever the vector  $\mathbf{a}$  approaches the Lawson surface the resulting shape becomes a sphere with two infinitesimal handles (Jülicher 1993). Whenever the vector  $\mathbf{a}$  of the special conformal

transformation applied to the Lawson surface points along an axis of high symmetry, the resulting shape has higher symmetry, too. Some of these shapes are shown in figure 21. In general, a conformal transformation of the Lawson surface has no obvious symmetry left. Again, there exist other embedded Willmore surfaces, but so far no stable ones are known (Kusner 1994).

#### 5.2.4. Genus $\geq 3$

For higher genus, little is known about the solution of Willmore's problem. Supported so far by limited numerical results (Hsu *et al.* 1992), Kusner's conjecture states that the global minimizer for  $G$  is given by the stereographic projection of the shape  $\xi_{g,1}$  from  $S^3$  to  $R^3$  (Kusner 1989).

As an exact result, a strict upper bound to the minimal energy,  $G_g < 16\pi$ , can be proven for any genus (Kusner 1989). An informal motivation for this result follows from considering two concentric spheres connected by narrow necks. The two spheres contribute an energy  $16\pi$  while the necks can be made of catenoids, which are minimal surfaces with no energy. The subtlety, of course, lies in the appropriate matching of the necks with the spheres in such a way that  $G_g < 16\pi$ .

For  $g \geq 3$ , further locally stable embedded Willmore surfaces are known besides  $\xi_{3,1}$  (Karcher *et al.* 1988, Hsu *et al.* 1992).

#### 5.2.5. Energy of handles

The solutions, or more precisely conjectures, on Willmore's problem can be used to comment on the energy of handles. In the limit  $\nu \rightarrow 1$ , the conformal transformation of the Clifford torus becomes a sphere with a small handle attached to it. One thus obtains the minimal energy of a handle  $G_h$  as  $G_h = G_1 - G_0 = (\pi/2 - 1)8\pi$  (Seifert 1991c).

Likewise, in the limit  $\nu \rightarrow 1$  which can be approached along various paths, the conformal transformation of the Lawson surface always becomes a sphere with two handles close together. The energy 'stored' in the two handles,  $G_2 - G_0 \simeq 0.75 \times 8\pi$ , is less than the energy  $2G_h$  of two independent handles. Thus, the two handles obtained in this way 'interact' and lower their energy. A similar statement holds for  $n$  handles whose energy can be bounded by  $G_n - 8\pi \leq 8\pi$  for optimal interaction.

### 5.3. Constraints and conformal invariance

The mathematical results described above cannot immediately be carried over to real vesicles since these are determined not only by the minimum of  $G$  but also by additional contributions to the energy, such as the area-difference elasticity, as well as by the geometrical constraints. Neither the area, nor the volume and the mean curvature are conformal invariants.

#### 5.3.1. Expansion for special conformal transformations

The effect of special conformal transformations on the geometrical quantities  $A$ ,  $V$  and  $M$  can be worked out analytically for small  $|\mathbf{a}| \ll 1$  (Seifert 1991b). A special conformal transformation acting on a surface  $\mathcal{S}$  with initial values  $V = V_1$ ,  $A = A_1$ , and  $M = M_1$  generates a new shape with

$$A(\mathbf{a}) = A_1[1 - 4\mathbf{R}^A \cdot \mathbf{a} + O(\mathbf{a}^2)], \quad (5.5)$$

$$V(\mathbf{a}) = V_1[1 - 6\mathbf{R}^V \cdot \mathbf{a} + O(\mathbf{a}^2)], \quad (5.6)$$

and

$$M(\mathbf{a}) = M_1[1 - 2\mathbf{R}^M \cdot \mathbf{a} + O(\mathbf{a}^2)]. \quad (5.7)$$

Here,  $\mathbf{R}^A \equiv (\oint dA \mathbf{R})/A$  is the centre of area,  $\mathbf{R}^V \equiv (\int dV \mathbf{R})/V$  is the center of volume and  $\mathbf{R}^M \equiv (\oint dA H \mathbf{R})/M$  is the centre of mean curvature.

From the expressions (5.5) to (5.7), one derives for the reduced variables the quite similar relations

$$\nu(\mathbf{a}) = \nu_1[1 + 6(\mathbf{R}^A - \mathbf{R}^V) \cdot \mathbf{a} + O(\mathbf{a}^2)] \quad (5.8)$$

and

$$m(\mathbf{a}) = \nu_1[1 + 2(\mathbf{R}^A - \mathbf{R}^M) \cdot \mathbf{a} + O(\mathbf{a}^2)]. \quad (5.9)$$

The terms of order  $\mathbf{a}^2$  are also known explicitly for axisymmetric shapes (Seifert 1991b).

### 5.3.2. Symmetry of stationary shapes

For small  $\mathbf{a}$ , a special conformal transformation induces a first variation of the shape under which the functional  $\Phi$  (3.1) should be invariant for any stationary shape. This condition together with the small  $\mathbf{a}$  expansion given above implies a surprising symmetry property of any stationary shape. If the linear terms from the expansions (5.5) to (5.7) are inserted as first variation into the general stationarity condition (3.2), one immediately obtains the relation

$$2\Sigma A \mathbf{R}^A + 3PV \mathbf{R}^V + QM \mathbf{R}^M = 0, \quad (5.10)$$

which has to hold for any stationary shape of the functional  $\Phi$ . This relation is the conformal equivalent of the homogeneity relation (3.10) derived from the scale invariance of  $G$ . The homogeneity relation can, in fact, be used to eliminate one Lagrangian multiplier in (5.10) in favour of the other two. One thus obtains (Seifert 1991b)

$$3PV(\mathbf{R}^V - \mathbf{R}^A) + QM(\mathbf{R}^M - \mathbf{R}^A) = 0, \quad (5.11)$$

which shows that one of the following two propositions holds true for any stationary shape of  $\Phi$ . (i) the end points of the three vectors  $\mathbf{R}^A$ ,  $\mathbf{R}^V$ , and  $\mathbf{R}^M$  are collinear, or (ii)  $\Sigma = P = Q = 0$ , i.e. the shape is a Willmore surface and thus a stationary shape of  $G$ .

Since there are no other Willmore surfaces of spherical topology besides the sphere, the first proposition has to hold for any other stationary shape of spherical topology. By symmetry, collinearity holds for all shapes which have at least an  $n$ -fold axis of symmetry and thus, in particular, for axisymmetric shapes and for ellipsoids. Consequently, one expects that the ground state for these cases in any of the curvature models has generically at least an  $n$ -fold axis and one can thus exclude whole classes of shapes as candidates for the ground state just by symmetry (Seifert 1991b). There is a caveat to this statement since it is conceivable that there are shapes without symmetry but which still have the property that the end points of the three vectors are collinear. Generically, however, shapes without this minimal symmetry

are not stationary and, in fact, no stationary shapes with less than a two-fold axis of symmetry have yet been found for spherical topology.

### 5.3.3. Stability with respect to special conformal transformations

Special conformal transformations can be used to derive a necessary (but, in general, not sufficient) criterion for stability of a stationary shape (Seifert 1991b). The idea is to apply a special conformal transformation to a stationary shape and then to compare the energy of the shape thus obtained with the energy of a stationary shape on the same branch at the same reduced volume and mean curvature  $m$  (or  $m_0$  in the ADE model). This criterion, which can be formulated in terms of the second-order expressions of (5.8) and (5.9), is easy to check for axisymmetric shapes by a simple numerical integration of geometrical quantities over the contour.

With this technique, the stability of the prolates and the oblates with respect to a symmetry-breaking deformation towards pears and stomatocytes, respectively, has been checked (Seifert 1991b). Surprisingly, within a large region of parameters, the instability obtained in this way is extremely close to the ‘true’ instability as found by solving the shape equations for the pears and the stomatocytes directly. This result indicates that the special conformal transformations are a very good approximation to the true unstable mode. This positive result encourages the use of special conformal transformations for an efficient approximate stability analysis with respect to breaking the axisymmetry. The implicit assumptions, however, are twofold. First, the symmetry of the instability has to be accessible by a special conformal transformation. An example for an instability which cannot be accessed by special conformal transformations is the breaking of the axisymmetry of prolates and oblates towards non-axisymmetric ellipsoids (Seifert 1991b). Secondly, the true instability and the one with respect to special conformal transformations have to be still close together for cases for which an independent check has not yet been performed.

## 5.4. Shapes and phase diagrams for genus 1

### 5.4.1. Phase diagrams

The phase diagrams for vesicles of toroidal topology have been investigated theoretically by a combination of two techniques. Firstly, the axisymmetric stationary shapes are determined by solving the appropriate shape equations (Seifert 1990, 1991c, Jülicher *et al.* 1993b). The solutions to these coupled nonlinear differential equations are a discrete set of sheets. Secondly, the stability of the axisymmetric shapes of lowest energy with respect to special conformal transformations is investigated.

Three different sheets of axisymmetric shapes can be distinguished: (i) the sheet of sickle-shaped tori, (ii) the sheet of discoid tori, and (iii) the sheet of toroidal stomatocytes, which do not have a symmetry plane perpendicular to the symmetry axis. Both the discoid tori and the sickle-shaped tori have reflection symmetry. They can be distinguished from each other as different sheets since they are separated, except for one shape which is that of the Clifford torus. Therefore, starting with the Clifford torus, which has an exactly circular cross-subsection, the two different ellipsoidal deformations of the contour lead to the sheets of discoid and sickle-shaped tori. The sheet of toroidal stomatocytes bifurcates from the sheet of sickle-shaped tori and from the sheet of discoid tori, thus connecting these two sheets.

Various types of limit shapes, where the sheets end and the shape becomes singular, can be distinguished. For all three sheets, one class of limit shapes occurs where the hole diameter vanishes. Formally, these shapes represent a connection to the spherical topology and are denoted by  $L_{\text{wick}}$ ,  $L_{\text{disc}}$  and  $L_{\text{sto}}$ . Other classes of limit shapes include tori with exactly circular cross subsection  $L_{\text{circ}}$  and shapes with diverging hole diameter. A detailed discussion of the limit shapes is given in Appendix B of (Jülicher *et al.* 1993b).

In a second step, the stability of these shapes with respect to special conformal transformations is checked (Jülicher *et al.* 1993b). If, for a given set of parameters, the axisymmetric shape of minimal energy is found to be unstable, the ground state must be non-axisymmetric for these parameters. Even though one cannot expect to obtain the region of the non-axisymmetric ground states exactly, this method gives at least a lower bound on the extension of this region. This lower bound should be a reasonable approximation since (i) it becomes exact in the neighbourhood of the Clifford torus, and (ii) the same approximation works excellently for the prolate/pear and oblate/stomatocyte bifurcation for vesicles of spherical topology as mentioned above. The phase diagram obtained in this way within the ADE model for  $\alpha = 1$  is shown in figure 22. The phase diagrams for the BC and the SC model can be found in (Jülicher *et al.* 1993b).

Typical for this phase diagram is the large region of non-axisymmetric shapes which are separated from the axisymmetric shapes by the instability line  $C^*$ . This large region is reminiscent of the degeneracy of the Willmore problem since in the BC model, in particular, the conformal transformations of the Clifford torus lie along a curve from the Clifford torus to the sphere. For  $m$  slightly above or below this curve, the ground state is, of course, still non-axisymmetric.

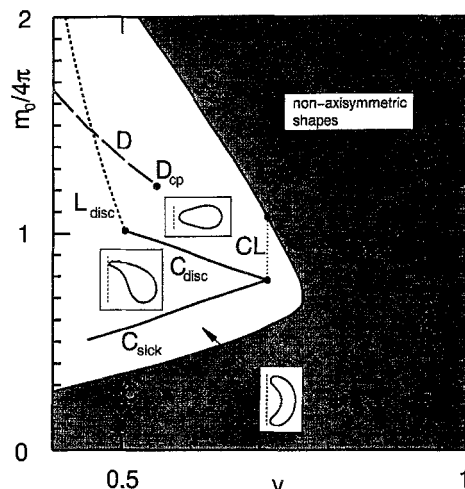


Figure 22. Phase diagram for toroidal vesicles in the ADE model with  $\alpha = 1$ . Three axisymmetric regions which are separated by continuous shape transformation lines  $C_{\text{stick}}$  and  $C_{\text{disc}}$  can be distinguished: (i) discoid tori, (ii) sickle-shaped tori and (iii) toroidal stomatocytes. The line  $L_{\text{disc}}$  represents limit shapes with vanishing hole diameter. The instability with respect to axisymmetry breaking conformal transformations is denoted by  $C^*$ . Within the region of axisymmetric shapes with reflection plane, discontinuous shape transformations from circular tori to discoid tori occur along the line  $D$ . This line ends up in a critical point  $D_{\text{cp}}$ . The Clifford torus is the shape of minimal energy along the dotted line (Jülicher *et al.* 1993b).

### 5.4.2. Experiments

All classes of shapes predicted by the theoretical work except for the sickle-shaped tori have been found in experiments. The first observations of toroidal shapes reported mainly Clifford tori (Mutz and Bensimon 1991). In this case, however, the membrane was partially polymerized, which should become a relevant perturbation of the fluid membrane considered here at least beyond the percolation threshold. In a subsequent study (Fourcade *et al.* 1992), shapes of quasi-circular cross-subsection, which theoretically belong to the discoid sheet, have been found, as well as non-axisymmetric shapes which resemble conformal transformations of the Clifford torus (see the experimental figure 4).

In a comprehensive work (Michalet and Bensimon 1995a), four types of tori have been found: (i) tori with quasi-circular cross-subsection for a volume range  $0.3 \lesssim v \lesssim v_{cl}$ , (ii) non-axisymmetric shapes resembling conformal transformations of the Clifford torus in the range  $v_{cl} \lesssim v \lesssim 0.92$ , (iii) discoid tori with and without axisymmetry and (iv) non-axisymmetric toroidal stomatocytes. All but the fourth observation are compatible with the phase diagram. The occurrence of non-axisymmetric toroidal stomatocytes is in discrepancy with theoretical work for two reasons. First, the axisymmetric toroidal shapes from which such a shape would have to bifurcate are all stable with respect to special conformal transformations. Secondly, as discussed in section 5.3.2, the occurrence of such shapes with only one symmetry plane as ground state (or even metastable state) can be expected to indicate, generically, that the corresponding shape is a Willmore surface for which there is neither theoretical nor experimental evidence.

## 5.5. Shapes and phase diagram for genus 2

### 5.5.1. Conformal diffusion

The threefold degeneracy for the Willmore problem for genus 2 has profound consequences for the phase diagram which becomes qualitatively different from the phase diagram for spherical or toroidal topology (Jülicher *et al.* 1993a). The new features are most easily described within the BC model.

The 3D space  $\mathcal{W}$  of conformal transformations of the Lawson surface can be projected onto the two-dimensional  $(v, m)$  plane. This leads to a region  $W$  in the phase diagram where the ground state is 1D degenerate, as shown in figure 23. A quantitative expression for the conformal mode which corresponds to this degeneracy can be obtained from the expressions (5.8) and (5.9) for special conformal transformations with small  $\mathbf{a}$ . Thus, the conformal mode that conserves both  $v$  and  $m$  can be identified as the special conformal transformation with  $\mathbf{a}$  obeying the differential equation (Jülicher *et al.* 1993a)

$$d\mathbf{a}/ds = (\mathbf{R}^A - \mathbf{R}^V) \times (\mathbf{R}^A - \mathbf{R}^M), \quad (5.12)$$

where  $s$  parametrizes the path in the space  $\mathcal{W}$ . In general, the conformal mode  $\mathbf{a}(s)$  that solves (5.12) destroys all symmetry planes of the shapes in the region  $W$ . However, along the path  $\mathbf{a}(s)$  which is a closed loop within  $\mathcal{W}$ , there are two different shapes which have one symmetry plane left. These shapes are shown in figure 24 for the conformal mode with  $(v, m) = (0.78, 1.027)$  as they have been obtained by numerical integration of (5.12) (Jülicher *et al.* 1993a).

The boundary of the region  $W$  in the phase diagram is obtained by mapping out the conformal transformations of the Lawson surface along the high symmetry

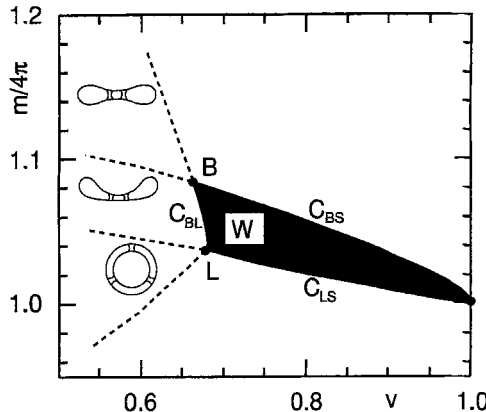


Figure 23. Phase diagram for genus 2 in the BC model. The letters along the boundary of the region of conformal degeneracy refer to the shapes shown in figure 21 (Jülicher *et al.* 1993a).



Figure 24. Shapes along a trajectory of conformal diffusion. All shapes have the same area, volume and integrated mean curvature (Jülicher *et al.* 1993a).

directions. There is one special shape with high symmetry on this boundary, which is called the Button surface, also shown in figure 21. It has three orthogonal mirror symmetry planes and inversion symmetry. The shapes along  $C_{BS}$ ,  $C_{BL}$ , and  $C_{LS}$  as shown in figure 21, constitute the boundary of the region  $W$  since these shapes have at least two mirror planes, which implies that  $R^A$ ,  $R^V$  and  $R^M$  are collinear and there is no conformal mode left, as can be seen from (5.12).

The existence of the phase  $W$  persists in the ADE model for arbitrary  $\alpha > 0$ . Whenever  $m_0$  lies in the range of  $m$  values which span the phase  $W$  at constant  $\nu$ , the area-difference elasticity is zero and the ground state in the ADE model also shows this one-fold conformal degeneracy.

The degeneracy of the ground state in the phase  $W$  has been predicted to have observable consequences whenever  $\nu$  and  $m_0$  of a vesicle belong to this phase. Because of thermal excitation its shape will permanently change within a diffusion process along the conformal trajectory. In analogy to rotational and translational diffusion, this phenomenon has been called conformal diffusion (Jülicher *et al.* 1993a).

Experimentally, conformal diffusion has indeed been found subsequently (Michalet 1994, Michalet and Bensimon 1995b). Very slow shape transformations

of shapes similar to those shown in figure 24 were recorded. The typical time scale  $t_{\text{cf}}$  of the order of a minute corresponds indeed to the typical diffusion time expected, since by dimensional analysis  $t_{\text{cf}} = \eta R_0^3/T = (\kappa/T)t_b \simeq 25t_b$  (Jülicher *et al.* 1993a). Here,  $t_b = \eta R_0^3/\kappa$  is the time scale for long-wavelength bending fluctuations, which is of the order of a second, and  $\eta$  is the solvent viscosity.

The experimental verification of conformal diffusion yields strong support for the energy  $G$  as the appropriate energy for vesicles. However, its manifestation does not directly confirm the ADE term since any energy  $B$  which can be written in the form (3.4) leads to this degeneracy for those parameters for which  $\partial g/\partial A = \partial g/\partial V = \partial g/\partial M = 0$ . Note that for the SC model  $\partial g/\partial M = -2C_0$  and, thus, there is no conformal diffusion in this variant for  $C_0 \neq 0$ . Strictly speaking, the observation of conformal diffusion rules out the spontaneous curvature model by this very general argument.

From a theoretical point of view, there are two subtleties related to conformal diffusion. First, there definitely will be correction terms to the energy  $W$  of the order of  $O(d/R)$ . These terms, however, are much smaller than the thermal energy and will therefore not be strong enough to prevent this phenomenon from happening. Secondly, conformal diffusion could be broken by thermal fluctuations analogous to the breaking of the scale invariance, which leads to a length-scale dependent renormalization of the bending rigidity (2.18). How relevant such an effect is compared with the thermal energy available for overcoming small perturbations remains to be investigated.

### 5.5.2. Phase diagram beyond the conformal phase

Outside of the degenerate conformal phase  $W$ , the shapes of minimal energy are no longer Willmore surfaces with constant energy  $G = G_2$ , but rather unique shapes with an energy  $G = G(v, m) > G_2$ , which can also be classified by their symmetry properties (Jülicher *et al.* 1993a). The topology of the phase diagram beyond  $W$  can be deduced by extending the symmetry of the shapes along the boundary of  $W$  as shown in figure 23. The phases thus obtained are in accordance with the rule of collinearity discussed in section 5.3.2. They can all be separated by continuous transitions according to the expectation that in the BC model all transitions are indeed continuous. The precise location of these transitions in the BC model is not known, nor do we know at present whether some of these transitions are pre-empted by first-order transitions for the ADE model as one could expect for small enough  $\alpha$ . The shapes and shape transitions outside of  $W$  could be calculated with a numerical minimization of triangulated surfaces taking into account the appropriate constraints, but this has not yet been done comprehensively.

The first experimental observation of genus 2 vesicles reported a shape very similar to the button surface shown in figure 21 (Fourcade *et al.* 1992). In the comprehensive study of Michalet and Bensimon (1995a), several button shapes have been found, one of which is shown in figure 5, as well as shapes which have the symmetry of the phases adjacent to the conformal phase  $W$ .

## 5.6. Vesicles of higher genus

The theoretical prediction of conformal diffusion holds for higher genus as well, since, for  $g \geq 2$ , the solution to the Willmore problem is threefold degenerate with respect to conformal transformations (Karcher *et al.* 1988, Hsu *et al.* 1992). In addition, for higher genus, there occur further locally stable embedded Willmore

surfaces which will give rise to degenerate local minima and even degenerate saddle points. In the  $(\nu, m)$  phase diagram, the resulting degenerate phases may overlap and be connected by ‘regular’ non-degenerate sheets. Obviously, a whole variety of interesting transitions can be expected in these systems, which as yet have only been rudimentarily investigated.

Experimentally, several shapes of higher genus have been found (Michalet *et al.* 1994a). A striking phenomenon is the occurrence of strong fluctuations of the position of the necks in shapes shown in figure 6, which correspond to those in the lower left corner of the phase diagram for genus 2. Even though these fluctuations do not correspond to conformal diffusion, their energy is quite small and, indeed, vanishes for  $\nu \rightarrow 0$ , which can be understood with a simple scaling estimate as follows (Seifert 1995b).

For two concentric spheres of distance  $d$  connected by  $N$  necks, the linear distance  $L$  between necks scales as  $L \sim R/\sqrt{N}$ . For a neck connecting two planar sheets a distance  $d$  apart, the curvature energy scales as  $\kappa(d/L)^2$ , where  $L$  is the ‘size’ of the circular patch where the neck is supposed to match the sheets (Michalet *et al.* 1994a). This power law anticipates a long-range interaction between necks. Displacing one neck a distance  $\epsilon L$  from its mean position in a lattice of necks costs an energy  $\kappa(d/L)^2 \epsilon^2$ . Thus, the mean square amplitude of the position of the neck in units of mean neck separation becomes  $\langle \epsilon^2 \rangle \sim (T/\kappa)(L/d)^2 \sim (T/\kappa)(R/d)^2/N$ . As a criterion for strong fluctuations, one can take that  $\langle \epsilon^2 \rangle \sim 1$ . Thus, one expects strong fluctuations whenever

$$N \lesssim (T/\kappa)(R/d)^2 \sim (T/\kappa)/\nu^2. \quad (5.13)$$

This result differs qualitatively from the one presented in (Michalet *et al.* 1994a) where it is argued that the necks behave like a gas of free particles with a hard core radius  $\sim (dL)^{1/2}$ . Such a description leads to a criterion for strong fluctuations,  $N \lesssim 1/\nu \sim R/d$ , that does not involve temperature.

A refined theory should include the interaction between many necks, which is certainly important in the same way as the energy of  $n$  interacting handles is different from  $n$  times the energy of one handle as pointed out in section 5.2.5. Likewise, for small  $d$ , one could include the interaction between the ‘spherical’ parts of the shape, as has been done for necks connecting planar bilayers (Goos and Gompper 1993). Finally, one may ask whether in the limit  $R, N \rightarrow \infty$ , with  $R^2/N$  fixed, a regular ‘lattice’ of necks exists. Such an ordered state would require an effective long-range curvature interaction in order to beat the Mermin–Wagner theorem, which rules out 2D ‘crystals’ for systems with short-range interactions (Mermin and Wagner 1966).

## 6. Adhesion

The previous sections dealt with the configurations of an isolated or free vesicle. Such a vesicle is a theoretical model system which is quite a challenge in terms of detailed quantitative studies from an experimental perspective. Except for the analysis of quasi-spherical fluctuations, the permanent rotation and (less so) the translation of the vesicle in a measuring chamber render a quantitative analysis of both the mean shape and the fluctuations difficult, as long as the experimental recording techniques are confined to a single focus plane. With the advent of more sophisticated equipment like confocal laser scanning microscopy, this restriction may become less severe.

Experimentalists, however, have designed various set-ups by which vesicles can be spatially confined and manipulated so that the Brownian rotation becomes less of a problem. Among these techniques are binding a vesicle to a substrate either through attractive forces or through gravitation by filling it with a slightly denser liquid than the surrounding solution. Such a vesicle no longer exhibits significant translational diffusion. Therefore, its shape fluctuations, in particular those of its bound part, are accessible to much more sensitive techniques such as reflection interference contrast microscopy (Zilker *et al.* 1987, Rädler 1993, Rädler *et al.* 1995).

In fact, adhesion or interaction of membranes is an important topic not only as a means of orienting a vesicle but rather for its ubiquitous occurrence in biological, biochemical and biophysical processes. In biology, adhesion of a vesicle represents an essential step for many processes such as endo- and exo-cytosis or fusion of cells (Alberts *et al.* 1989). Efficient drug delivery by small vesicles requires an understanding of the interaction of the liposomes with cell membranes (Lasic 1995). Biosensors are based on the binding of membranes to substrates.

Studying the adhesion of membranes and vesicles will thus lead to important insights into the interactions of these soft systems. This section deals with the theoretical approaches with an emphasis on the specific effects that arise for the adhesion of (finite closed) vesicles in contrast to the adhesion of (infinite open) planar membranes.

We begin with a list of the available experimental techniques in section 6.1, section 6.2 is devoted to a brief review of the adhesion of (infinite) almost planar membranes. Here the crucial role of steric repulsion due to thermal fluctuations is discussed (Helfrich 1978, Lipowsky and Leibler 1986). Vesicle adhesion is considered in section 6.3, where the microscopic potential is replaced by a phenomenological contact potential. The shape of a bound vesicle in such a potential is governed by the competition between adhesion and bending energies. As a central result, this competition leads to an adhesion transition (Seifert and Lipowsky 1990). The effect of the finite range of the potential is discussed in section 6.4, section 6.5 is devoted to a self-consistent theory for bound vesicles which treats the adhesion potential and the fluctuations on the same footing (Seifert 1995d). This theory allows us to address the question of whether or not genuine tension-induced adhesion (Servuss and Helfrich 1989) is possible for vesicles. In section 6.6, the effect of gravity on vesicle shape is discussed. Section 6.7 is devoted to a brief review of recent work on focal adhesion induced either by specific molecules or laser traps.

### *6.1. Experimental methods*

The interaction of membranes and vesicles has been studied by using different experimental techniques which will be very briefly reviewed in this section. More detailed descriptions can be found in recent reviews (Lipowsky 1995, Parsegian and Rand 1995, Helfrich 1995). Conceptually, one should distinguish the interaction of almost planar membranes, whose lateral extension is assumed to be infinite, from the study of vesicle adhesion for which the closure of the vesicle can lead to additional effects not present for planar membranes.

#### *6.1.1. Force apparatus*

Bare interaction between membranes can be studied with the surface force apparatus developed by Israelachvili and co-workers (Marra and Israelachvili 1985, Israelachvili 1991). In this technique bilayers are deposited on thin mica sheets

which are glued to glass cylinders. This technique can be used to measure the force versus distance relation. Since the membranes cannot fluctuate, one obtains information about the bare forces.

#### 6.1.2. Osmotic stress method

This technique (Parsegian *et al.* 1979, Rand and Parsegian 1989, Parsegian and Rand 1995) applies to lamellar membrane stacks which are separated by a water-permeable membrane from a polymer solution. By changing the concentration of the polymers one can vary the osmotic stress that affects the intermembrane distance between the bilayers. This distance is measured by X-ray or neutron scattering. The force versus separation relation includes the effect of membrane fluctuations.

#### 6.1.3. Optical microscopy

Optical studies of dilute membrane systems (Servuss and Helfrich 1989, Helfrich 1995) are conceptually in between experiments on planar membranes and on vesicles. These membranes are part of large vesicles whose topology, however, cannot be resolved. Studying the region of contact between different sheets, one obtains information on the interaction energy and lateral tensions in the membrane.

#### 6.1.4. Micropipette aspiration

Evans has perfected the use of micropipettes to manipulate vesicles (Evans and Metcalfe 1984, Evans 1990, 1995a). This set-up is particularly useful in studying the adhesion of two vesicles, each one of which is sucked into a pipette. By changing the suction pressure in one of the pipettes, one can change the area of adhesion between the two vesicles. Balancing the energy gained by a larger adhesion area with the cost paid in work against the pressure, a value for the effective contact energy can be extracted.

#### 6.1.5. Reflection interference contrast microscopy

This technique (Zilker *et al.* 1987, 1992, Rädler and Sackmann 1992, Rädler *et al.* 1995) can be used to measure distances from a coated substrate with a resolution of the order of a nanometre, whereas the lateral resolution is confined to an optical wavelength. If a vesicle is put on such a substrate, one can measure the fluctuations of its bound part as well as the rounding in the region where the vesicle is forced to detach from the substrate because of its topological closure constraint.

### 6.2. Bound planar membranes

Before we turn to bound vesicles, we have to review briefly in this section some of the extensive work on the adhesion of planar membranes in microscopic potentials for four reasons. (i) It is instructive to discuss an almost planar adhering membrane along the same lines as we discussed the fluctuations of an almost planar free membrane in sections 2.2 and 2.3. (ii) The contact potential approach discussed in section 6.3 leads to a curvature-driven adhesion transition from a bound to a free state for closed vesicles (Seifert and Lipowsky 1990). Since planar membranes can undergo a thermally driven unbinding transition (Lipowsky and Leibler 1986, Mutz and Helfrich 1989), it is important to discuss the interplay of these two mechanisms. (iii) A self-consistent theory of vesicles adhesion requires a knowledge of the adhesion of planar membranes under tension. (iv) In the next section, the dynamical fluctuations of a bound almost planar membrane are investigated. In order to

classify the various regimes, an understanding of the static equilibrium fluctuations is a prerequisite.

### 6.2.1. Direct interactions

The surface force apparatus and the osmotic stress method described above give, in principle, the interaction potential  $V(l)$  between two planar membranes a distance  $l$  apart. Likewise, one may consider a membrane at a distance  $l$  from a rigid substrate. Conceptually, it is helpful first to assume that the effect of fluctuations can be neglected. Thus, one deals with the so-called direct interaction  $V_d(l)$ , which comprises the following forces reviewed in detail with their  $l$  dependence elsewhere (Israelachvili 1991, Lipowsky 1995).

For charged membranes, the Coulomb interaction provides a long-range potential  $V_d(l) \sim 1/l$ . On length scales beyond the Debye length, which depends on the salt concentration, this interaction becomes exponentially screened. Even for an uncharged membrane, the fluctuating dipoles lead to the van der Waals interaction which decays like a power law with various regimes depending on the separation. If the membrane is impermeable to large molecules, these molecules can be used to build up an osmotic pressure which pushes a membrane towards a substrate, yielding a linear potential in  $l$ . Finally, there are short-range repulsive interactions. These include the ‘hydration forces’, which are supposed to arise from a local rearrangement of hydrogen bondings near the membrane (Rand and Parsegian 1989). More recently, the effect of local protrusions of the lipid molecules has also been shown to lead to a short-range potential (Israelachvili and Wennerström 1990, Lipowsky and Grotehans 1993).

If all these forces are summarized in a potential  $V_d(l)$ , the energy of an almost planar bilayer membrane at a local distance  $l(x, y)$  from a substrate is given by

$$F^a = \int dx dy \left[ \frac{\kappa}{2} (\nabla^2 l)^2 + \frac{\Sigma}{2} (\nabla l)^2 + V(l) \right], \quad (6.1)$$

where we drop the subscript  $d$  in  $V_d(l)$ . For an almost flat membrane, the tension  $\Sigma$  can be considered as externally given. For the bound part of a large vesicle, it will arise physically from the area constraint, as will be discussed in section 6.5. Using the energy (6.1), the membrane is described within the classical model. Including the bilayer aspect along the lines of section 2.3 leads to new effects for static problems only if a coupling between the separation  $l$  and the monolayer densities  $\phi^\pm$  is introduced. Such a coupling, which could arise from the van der Waals interaction, remains to be explored.

As a first step, the potential  $V(l)$  is replaced by its harmonic approximation around the minimum  $l_0$  with curvature

$$\Omega \equiv d^2 V / dl^2|_{l=l_0}. \quad (6.2)$$

For a small local displacement,

$$h(x, y) \equiv l(x, y) - l_0, \quad (6.3)$$

of the membrane from the minimum, the free energy  $F_0^a$  of an adhering bilayer membrane is given by

$$F_0^a \equiv \frac{1}{2} \int \frac{d^2 q}{(2\pi)^2} h_{\mathbf{q}} (\kappa q^4 + \Sigma q^2 + \Omega) h_{\mathbf{q}}^* \equiv \frac{1}{2} \int \frac{d^2 q}{(2\pi)^2} h_{\mathbf{q}} E_0^a(q) h_{\mathbf{q}}^*, \quad (6.4)$$

where the latter relation defines the ‘energy’  $E_0^a$ .

Depending on the strength of the tension  $\Sigma$ , two cases must be distinguished theoretically.

- (1) For *weak* tension ( $\Sigma \ll 2(\Omega\kappa)^{1/2}$ ), the tension term never dominates the energy  $E_0^a$  which thus exhibits only one cross-over length scale at

$$\xi \equiv (\kappa/\Omega)^{1/4}. \quad (6.5)$$

For  $q < 1/\xi$ , the fluctuations of such a membrane are dominated by the potential, while for  $q > 1/\xi$  they are governed by bending elasticity.

- (2) For *strong* tension ( $\Sigma \gg 2(\Omega\kappa)^{1/2}$ ), the tension dominates the energy in an intermediate range  $\xi_{\Sigma}^{-1} < q < \xi_{\kappa}^{-1}$ , with the two crossover length scales

$$\xi_{\Sigma} \equiv (\Sigma/\Omega)^{1/2} \quad \text{and} \quad \xi_{\kappa} \equiv (\kappa/\Sigma)^{1/2}. \quad (6.6)$$

The static height–height correlation functions are given in harmonic approximation as

$$\langle h_{\mathbf{q}} h_{\mathbf{q}'}^* \rangle = \frac{T}{\kappa q^4 + \Sigma q^2 + \Omega} (2\pi)^2 \delta(\mathbf{q} - \mathbf{q}'). \quad (6.7)$$

From this correlation function, one obtains the mean roughness of the membrane as

$$\langle h^2 \rangle \equiv \int \frac{d^2 q}{(2\pi)^2} \int \frac{d^2 q'}{(2\pi)^2} \langle h_{\mathbf{q}} h_{\mathbf{q}'}^* \rangle \approx \begin{cases} \frac{T}{8(\kappa\Omega)^{1/2}}, & \text{for } \kappa = 0, \\ \frac{T}{4\pi\Sigma} \ln(1 + \Sigma/\Omega a^2), & \text{for } \sigma = 0, \end{cases} \quad (6.8)$$

and a somewhat longer expression in between the two limiting cases (Lipowsky 1995). Here  $a$  is a short-distance cut-off.

### 6.2.2. Steric interaction in the presence of lateral tension

The Gaussian approximation described above ignores the presence of the hard-wall constraint,  $l(x, y) > 0$ , which can restrict the fluctuations of the membrane even further than the direct repulsive interaction. Two approaches have been invented to include this effect. In the *phenomenological superposition approach*, one adds the effect of the hard wall as a fluctuation potential  $V_f(l)$  to the direct interaction  $V_d(l)$ . Once  $V_f(l)$  is known, one proceeds as above and calculates the mean separation  $l_0$  and fluctuations  $\langle h^2 \rangle$  replacing  $V(l)$  with  $V_d(l) + V_f(l)$ . Within the *systematic renormalization group approach* (Lipowsky and Leibler 1986, Lipowsky 1995), fluctuations on short length scales are iteratively integrated out to yield an effective or renormalized potential on longer length scales. Depending on the details of the direct interaction, the renormalization group results either vindicate or falsify results

from the superposition approach. In this section, we discuss the superposition approach and comment on its failure.

The steric or fluctuation potential can be motivated or derived by slightly different methods in various geometries. One may consider either one membrane between two rigid walls, one membrane pushed by a linear potential, i.e. a pressure, towards a rigid substrate or a membrane stack pushed towards a wall. The basic idea is to replace the hard constraints imposed by the walls or a non-crossing condition among the membranes by a soft potential whose form or value is determined self-consistently (Helfrich 1978).

The derivation presented here (Seifert 1995d) applies to a membrane subject to a pressure pushing it towards a rigid substrate. It starts by expressing the increase in free energy due to the confinement of fluctuations as (Helfrich 1978, Lipowsky 1990)

$$V_f(l) = bT/\xi(l)^2, \quad (6.9)$$

where  $T$  is the temperature in units of energy,  $b$  is a numerical factor to be determined later and  $\xi(l)$  is the lateral correlation length that depends on the separation  $l$ . The correlation length is defined by the condition that beyond this length fluctuations are no longer determined by the membrane elasticity but rather by the effective potential  $V_f(l)$ , which mimics the effect of the hard wall. Equivalently, membrane patches of linear size  $\xi(l)$  can be regarded as essentially uncorrelated fluctuating units each of which carries a free energy  $T$ . Using (6.2) and the correlation function (6.7), a sensible definition of  $\xi(l)$  is

$$\kappa/\xi(l)^4 + \Sigma/\xi(l)^2 = V_f''(l). \quad (6.10)$$

Replacing  $1/\xi(l)^2$  from (6.9) by  $V_f(l)/bT$ , a nonlinear differential equation for the fluctuation potential is obtained:

$$\kappa V_f(l)^2/(bT)^2 + \Sigma V_f(l)/bT = V_f''(l). \quad (6.11)$$

If  $V_f(l)$  is required to vanish at infinity and diverge for  $l \rightarrow 0$ , the unique solution is given by (Seifert 1995d)

$$V_f(l) = \frac{6b^2 T^2}{\kappa l^2} \frac{y^2}{\sinh^2(y)}, \quad (6.12)$$

with

$$y \equiv (\Sigma/bT)^{1/2} l/2. \quad (6.13)$$

In the tensionless case,  $\Sigma \rightarrow 0$ , or for small separations  $l_0 \rightarrow 0$ , the scaling variable  $y$  goes to 0. One then recovers with  $V_f(l) = 6b^2 T^2 / \kappa l^2$ , the famous Helfrich potential (Helfrich 1978) of a tensionless membrane. The numerical prefactor has been determined by Monte Carlo methods as  $b = b_1 \simeq 0.1$  for a single membrane (Lipowsky and Zielinska 1989, Netz, 1995) or from membrane stacks (Janke and Kleinert 1987, Gompper and Kroll 1989, Netz and Lipowsky 1993, 1995).

For  $l \rightarrow \infty$ , the effective potential derived above leads to an exponential decay. The decay length agrees with renormalization group results (Lipowsky 1995) if the numerical factor  $b$  is chosen as  $b = b_2 \equiv 1/2\pi$ .

The above derivation of the effective potential in the presence of lateral tension seems to be the simplest one which agrees with more systematic renormalization group results in both limits  $y \rightarrow 0, \infty$ . An alternative derivation of the steric potential in the *tensionless* case starts from assuming a form  $V_f(l) = A/l^\tau$  with yet unknown  $A$  and  $\tau$ . Adding the pressure term  $pl$  to this potential yields the minimum at  $l_0 = (A\tau/p)^{1/\tau}$ . Expanding the effective potential around this minimum at  $l_0$  leads to  $\Omega = \tau(\tau+1)A/l_0^{\tau+2}$  from which one obtains the roughness

$$\langle h^2 \rangle = \frac{T}{8\kappa} \left( \frac{\kappa l_0^{\tau+2}}{A\tau(\tau+1)} \right)^{1/2}. \quad (6.14)$$

The self-consistency requirement  $\langle h^2 \rangle \sim l_0^2$  fixes the exponent  $\tau = 2$  and the amplitude  $A = T^2/\kappa$  up to a numerical prefactor. The rationale behind this self-consistency requirement is the idea that if  $\langle h^2 \rangle \ll l_0^2$ , one has overestimated the effect of the hard wall, while for  $\langle h^2 \rangle \gg l_0^2$ , one has underestimated it. As attractive as such a reasoning may look, it fails in the presence of tension where  $h^2$  and  $l_0^2$  scale differently since  $\langle h^2 \rangle \sim l_0(T/\Sigma)^{1/2}$  according to renormalization group results (Lipowsky 1995). Consequently, attempts to derive the effective potential which do not recognize this different scaling fail to predict the correct exponential asymptotic decay of the fluctuation potential for large  $l$  and rather yield a Gaussian decay (Evans 1991).

### 6.2.3. Unbinding transition

The most important qualitative feature of a membrane interacting with a substrate or with other membranes is whether or not the membrane is bound. Clearly, the direct potential  $V_d(l)$  should have a minimum with finite depth as a necessary condition for such a bound state. Within the superposition approach the sufficient condition is that such a minimum at  $l_0$  with  $V(l_0) < 0$  is still present after the fluctuation potential (6.12) has been added to the direct potential. As a physical parameter, e.g. temperature, is changed, the depth of this minimum can decrease. Two possibilities arise theoretically as sketched in figure 25. (i) The position  $l_0$  of the minimum remains finite even when  $V(l_0) = 0$ . In this case, one expects a discontinuous transition from a bound state to the unbound state as temperature increases. (ii) As the minimum gets more shallow, its position may approach infinity. In this case, the unbinding transition is discontinuous.

Prediction of the order of the unbinding transition based on the superposition approach is vindicated by the more systematic renormalization group in the following cases (Lipowsky 1990). For tensionless membranes, the attractive part of the direct interaction should decay slower than  $1/l^2$ . If the attractive part decays faster than  $1/l^2$  for large  $l$ , the effect of the hard wall is non-trivial, and superposition of direct interaction and fluctuation potential fails. In this regime, either renormalization group methods or Monte Carlo simulations are required to determine the effective fluctuations properly (Lipowsky 1990, Lipowsky and Zielinska 1989).

The effect of a non-zero tension on the membrane is to suppress fluctuations (Helfrich and Servuss 1984). Therefore, superposition is valid for a larger class of potentials. In fact, it turns out that all direct potentials whose attractive and repulsive parts decay like power laws can be treated by superposition. For

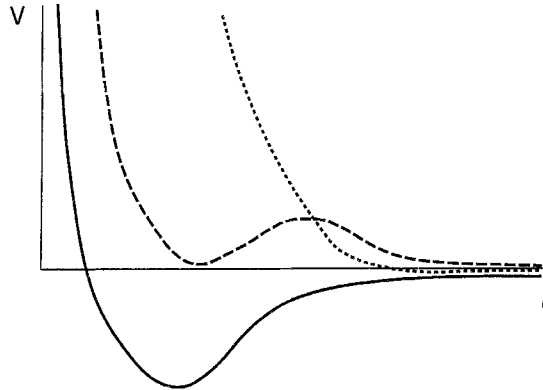


Figure 25. Adhesion potential  $V(l)$  at the unbinding transition within the superposition approach. The full curve sketches a potential in which the membrane is bound. If as the temperature is increased the potential assumes the dashed form, the unbinding transition is discontinuous. If the potential deforms towards the dotted form, unbinding takes place continuously.

exponential direct interactions, the effect of the hard wall is extremely subtle and details of the direct interaction become crucial (Lipowsky 1990).

However, even in cases where superposition fails to predict the correct order of the unbinding transition, it may still give a reasonable quantitative estimate for the effective potential of a bound state where fluctuations are not yet as pronounced as they are close to the unbinding transition.

Experimental evidence for a thermally driven unbinding transition in bunches of membranes has been found by optical microscopy (Mutz and Helfrich 1989). Since the perspective of this article is on vesicle adhesion, we will not discuss the theoretical subtleties which can arise when stacks of membranes unbind. This phenomenon has been studied by mean field theories (Milner and Roux 1992, Helfrich 1993), extensive Monte Carlo work (Cook-Röder and Lipowsky 1992, Netz and Lipowsky 1993) and various scaling pictures (Lipowsky 1995).

### 6.3. Adhesion in a contact potential

#### 6.3.1. Contact potential and contact curvature

After the discussion of infinite bound membranes we turn to the focus of this section, which is the adhesion of closed vesicles. For such a vesicle one may, as a first step, take advantage of the effective length-scale separation between the size of the vesicle and the range of the interactions which is of the order of several nanometres. Thus, one replaces the total potential  $V(l)$  by an effective contact energy  $W = -V(l_0) > 0$ , which can be identified by the value of the effective interaction potential at the mean separation  $l_0$  of the membrane from the substrate. If the vesicle and the wall have contact area  $A^*$ , the vesicle gains the adhesion energy (Seifert and Lipowsky 1990)

$$F_a = -WA^*, \quad (6.15)$$

which must be added to the curvature energy.

Such a contact potential does not alter the shape equations found for free vesicles. It rather enters the boundary condition at the point of contact. First, the contact angle is necessarily  $\pi$  since any sharp bend would have an infinite curvature energy. This implies that the membrane is curved only in one direction, and  $1/R_2^* = 0$  along the line of contact. Second, the contact curvature  $1/R_1^*$  is determined by (Seifert and Lipowsky 1990)

$$1/R_1^* = (2W/\kappa)^{1/2}, \quad (6.16)$$

which follows from minimizing with respect to the area of contact. This boundary condition, which does not depend on the area of the vesicle, holds for all variants of the curvature model.

The different experimental methods described in section 6.1 give, in general, different values for the effective contact potential  $W$ , which are in the range  $10^{-4}$ – $1\text{ mJ m}^{-2}$ . For rough estimates in this section, we will use the value of  $1\text{ mJ m}^{-2}$  for *strong* adhesion, and the value of  $10^{-4}\text{ mJ m}^{-2}$  for *weak* adhesion. The contact curvature  $1/R_1^*$  expected from these estimates span  $1/R_1^* \simeq 1/(10\text{ nm})$  for strong adhesion (using  $\kappa = 10^{-19}\text{ J}$ ) and  $1/R_1^* \simeq 1\text{ }\mu\text{m}^{-1}$  for weak adhesion. The latter value is clearly accessible by light microscopy. In fact, Rädler *et al.* (1995) using reflection interference contrast microscopy (Zilker *et al.* 1987, 1992) measured distances from a coated substrate with a resolution of the order of a nanometre, whereas the lateral resolution is confined to an optical wavelength. With this technique, a contact curvature of the order of  $1/(10\text{ }\mu\text{m})$  has been reported, from which the contact energy has then been determined. Similar values have also been found in dilute membrane systems (Servuss and Helfrich 1989).

### 6.3.2. Curvature-driven adhesion transition

Solving the shape equations for axisymmetric shapes with the boundary condition (6.16) leads to a variety of bound shapes which can be arranged in a phase diagram, as in the case of free vesicles. The basic physics behind the competition between adhesion and curvature energy already becomes evident in a minimal model, which contains only the local bending energy  $G$  (2.51), the adhesion energy  $F_a$  (6.15), a constraint on the total area  $A = 4\pi R_0^2$ , and no volume constraint. Such a model depends only on the reduced potential strength

$$w \equiv WR_0^2/. \quad (6.17)$$

Several shapes for different  $w$  are shown in figure 26. With decreasing strength of the contact potential  $w$ , the area of contact  $A^*$  also decreases and vanishes for  $w = w_a = 2$ . For the unscaled potential strength  $W$ , the area of contact vanishes at the size-dependent value

$$W_a = 2\kappa/R_0^2. \quad (6.18)$$

For  $W = W_a$ , the bound shape resembles the free shape corresponding to the same constraint, which is a sphere except for the fact that the contact curvature  $1/R_1^* = 2/R_0$  is *twice* the curvature of the sphere. However, the contact *mean* curvature  $H^* \equiv (1/R_1^* + 1/R_2^*)/2 = 1/R_0$  is equal to the mean curvature of the sphere. For  $W < W_a$ , an attractive potential does not lead to a bound shape with

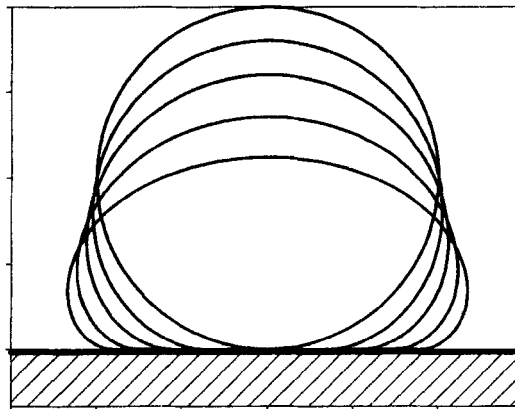


Figure 26. Shapes of bound vesicles which all have the same area for reduced adhesion energy,  $w = 2.0, 2.9, 4.1, 6.4$  and  $10.2$  (Seifert and Lipowsky 1990).

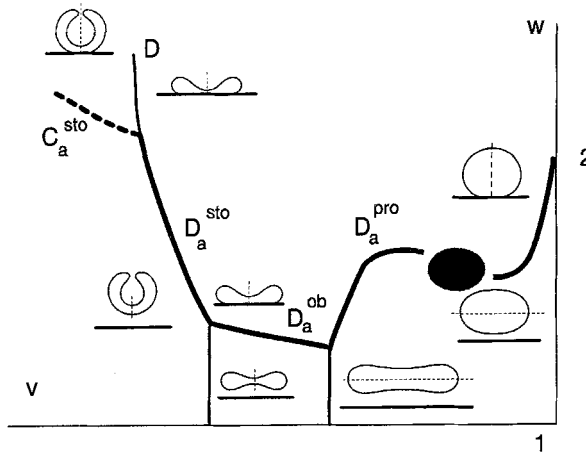


Figure 27. Schematic phase diagram with free and bound shapes at constant area and volume. The bold curves show the adhesion transition at  $w = x_a(v)$ , which can be discontinuous ( $D_a^{pro}$ ,  $D_a^{ob}$  and  $D_a^{sto}$ ) or continuous ( $C_a^{sto}$ ). In the dashed region, non-axisymmetric bound shapes are relevant. The dashed straight lines across the shapes denote the axis of symmetry (Seifert and Lipowsky 1993).

finite area of contact. Thus, the vesicle undergoes a continuous adhesion transition at  $W = W_a$  (Seifert and Lipowsky 1990).

A somewhat more complex situation arises when, in addition to the area, the enclosed volume is also kept constant. The phase diagram becomes two-dimensional, and depends on  $v$  and  $w$ . This phase diagram is shown in figure 27, together with some bound shapes (Seifert and Lipowsky 1993, Lipowsky and Seifert 1991b, Lipowsky and Seifert 1991a). Its main characteristic is the line of adhesion transitions  $w_a(v)$  which separates bound from free states. The transition can be continuous or discontinuous depending on the reduced volume. The energy minimization yields a numerical relation

$$\bar{\Sigma}(W) = W/\gamma(v, w) \quad (6.19)$$

between the Lagrange multiplier  $\bar{\Sigma}$  used to implement the area constraint and the contact potential  $W$  which will be needed below.

The character of the adhesion transition depends on the ensemble. If the area is subject to a constant surface tension, a discontinuous curvature-driven adhesion transition has been found in a model for adhesion and rolling of leucocytes (Bruinsma 1995).

The 4D phase diagram for adhesion with explicit inclusion of the area-difference-elasticity energy has not yet been studied. In analogy to the free case, one expects that the non-local energy favours continuous adhesion transitions and the occurrence of non-axisymmetric shapes. Non-axisymmetric shapes are more relevant than in the case of free vesicles, since the axisymmetry of free prolates is broken if these shapes adhere with their long axis parallel to the substrate. Such a bound shape can no longer be obtained by solving the axisymmetric shape equations, but it is accessible by direct minimization, as described below.

Experimentally, there has not yet been any direct evidence for a curvature-driven adhesion transition for vesicles. Two different approaches are conceivable in order to observe this transition. (i) Changing the temperature will affect both the reduced volume and the scaled adhesion potential  $w = WR_0^2$  via the area expansion. A temperature decrease also decreases  $w$  and increases  $v$ . Therefore, a bound vesicle may become free upon cooling provided its initial state at the higher temperature is already sufficiently close to the adhesion transition. Likewise, osmotic deflation or inflation, which does not affect  $w$ , can induce a crossing of the adhesion transition in the phase diagram (figure 27). (ii) A more indirect but quite elegant confirmation of the theory described above could make use of the characteristic size dependence of the adhesion transition as expressed in (6.18). This relation implies that, for fixed  $W$ , in an ensemble of vesicles, only those with  $R_0 > R_a \equiv (2/W_a)^{1/2}$  are bound to the substrate.

### 6.3.3. Strong adhesion: effective contact angle

For strong adhesion, or, equivalently, for large vesicles, a simplification occurs because the scale-invariant curvature energy becomes irrelevant compared with the gain in contact energy. In this limit,  $R_0 \gg R_a$ , or  $W \gg W_a$ , the shape of the bound vesicle approaches a spherical cap configuration. If only the area is constrained, this limit shape is a flat pancake with an energy

$$\kappa G + F_a \approx -2\pi WR_0^2 + 2\pi g(2W)^{1/2}R_0, \quad (6.20)$$

with the numerical coefficient  $g \simeq 2.8$  (Lipowsky and Seifert 1991b). If in addition the volume is constrained, the vesicle becomes a spherical cap for strong adhesion, as shown in figure 28. In both cases, an *effective contact angle*  $\Psi_{\text{eff}}$ , which obeys a Young–Dupré equation, can be defined (Seifert and Lipowsky 1990) as

$$W = \bar{\Sigma}(1 + \cos \Psi_{\text{eff}}), \quad (6.21)$$

with  $\Psi_{\text{eff}} = 0$  for the pancake. In (6.21), the quantity  $\bar{\Sigma}$  is the (numerical) value of the Lagrange multiplier for the area constraint. It also obeys the Laplace equation  $2\bar{\Sigma} + P/R_0 = 0$ , where  $P$  is the Lagrangian multiplier used to implement the volume constraint. Thus, in this limit the scaling function  $\gamma(w, v)$  introduced in (6.19) becomes

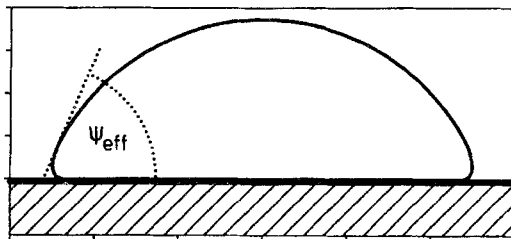


Figure 28. Spherical cap conformation for strong adhesion,  $w = 375$ , and effective contact angle  $\Psi_{\text{eff}} = 65.5^\circ$  (Seifert and Lipowsky 1990).

$$\gamma(w \rightarrow \infty, v) = 1 - \cos \Psi_{\text{eff}}(v). \quad (6.22)$$

The spherical cap geometry determines the relation between the effective contact angle  $\Psi_{\text{eff}}$  and the reduced volume as

$$v = \frac{9 \cos(\Psi_{\text{eff}})/2 - \cos(3\Psi_{\text{eff}})/2 + 4}{[2 + 2 \cos(\Psi_{\text{eff}}) + \sin^2(\Psi_{\text{eff}})]^{3/2}}, \quad (6.23)$$

with  $v \approx 1 - (3/32)\Psi_{\text{eff}}^4$  for small  $\Psi_{\text{eff}}$ .

It is meaningless to define an effective contact angle if the condition  $R_0 \gg R_a$ , i.e.  $W > \kappa/R_0^2$ , does not hold. The curvature energy becomes irrelevant only if it holds, and then adhesion of the vesicle resembles wetting by liquid droplets.

Spherical cap-like configurations are clearly seen in micro-pipette experiments (Evans and Rawicz 1990) as well as in freeze-fracture electron microscopy for smaller vesicles (Bailey *et al.* 1990). Pancakes for strong adhesion have also been found by reflection interference microscopy (Rädler 1993).

#### 6.3.4. Strong adhesion: adhesion-induced rupture and fusion

For strong adhesion, elastic stretching of the membrane becomes relevant. In fact, the energetic competition which determines the configuration does not involve the balance between curvature energy the adhesion energy, but rather the balance between adhesion energy and elastic energy:

$$F_k \equiv (k/2)(A - A_0)^2/A_0. \quad (6.24)$$

Here,  $k$  is the area compressibility modulus of the order of  $10^2 \text{ mJ m}^{-2}$ . Such an extended model leads to the same shape equations as the model with a hard-area constraint. Even the boundary condition (6.16) remains unchanged. The phase diagram, however, changes due to the additional energy. Balancing the adhesion energy with the stretching term leads to the adhesion-induced stretching of the order of

$$(A - A_0)/A_0 \simeq W/k. \quad (6.25)$$

Identifying  $k(A - A_0)/A_0$  with an elastic tension  $\Sigma_{\text{el}}$ , we find the relation  $\Sigma_{\text{el}} \sim W$  for strong adhesion. The bound vesicle ruptures, as soon as  $\Sigma_{\text{el}}$  exceeds the lysis tension, which is known experimentally to happen at about  $(A - A_0)/A_0 \simeq 0.03$  (Evans and

Needham 1987). From (6.25) one then derives that any adhesion potential stronger than  $0.03k$  induces rupture.

After the bound vesicle has ruptured, its configuration becomes an open disc. Such a bound disc has an energy (Lipowsky and Seifert 1991b)

$$F_{bd} = -4\pi WR_0^2 + 4\pi\Sigma_e R_0, \quad (6.26)$$

where  $\Sigma_e$  is the edge tension along the circumference of the bound disc. A comparison of the energy (6.26) with the energy (6.20) of a pancake shows that for  $R_0 \gg R_{bd} \equiv \Sigma_e/W$  the bound disc always has lower energy.

The limit of strong adhesion can also be reached from a different route even if the original adhesion energy was not ‘strong’. If more and more bound vesicles cover the substrate, they will come into contact and may fuse. For free vesicles, fusion of two vesicles with equal area  $A \equiv 4\pi R_0^2$  (but no constraint on the volume) leads to a gain in energy  $\Delta F_{fv} = 8\pi + 4\pi_G$ . If two bound vesicles fuse, the gain in energy  $\Delta F_{bv}$  is always larger than  $\Delta F_{fv}$  and satisfies  $\Delta F_{bv} \geq \tilde{g}\pi + 4\pi_G$  with  $\tilde{g} \approx 8.3$  (Lipowsky and Seifert 1991b). For large  $R_0$ , this energy gain behaves as  $\Delta F_{bv} \approx 4\pi g(\sqrt{2}-1)(W)^{1/2}R_0$ , where (6.20) has been used. Thus, adhesion favours fusion. As the size of the fused vesicle increases, its shape becomes more like a pancake. If the elastic tension exceeds the threshold for lysis, the pancake ruptures and becomes an open bound disc.

These crude energetic considerations lead to a scenario where vesicles adhere to the wall, fuse at the wall and rupture. Finally, the open discs will also fuse, thus forming a bilayer parallel to the wall. Experimental evidence for such a scenario came from X-ray scattering of a vesicle suspension which revealed a lamellar structure at the air-water interface (Cevc *et al.* 1990, Fenzl *et al.* 1995). The strong temperature dependence of the dynamics of formation of the lamella that was found experimentally demonstrates that the kinetics of this process is quite subtle.

#### 6.4. Adhesion in a potential with finite range: the pinned state

The contact potential is well suited for studying the mean shape of bound vesicles, but is less convenient for a discussion of the effect of thermal fluctuations. In such a potential, a membrane segment is either subject to the full adhesion energy if bound, or does not feel the substrate at all, if free.

In this section, we therefore consider adhesion of vesicles in a potential with non-zero range (Evans 1985) (not only) as a prerequisite for the discussion of fluctuations in the next section. On the level of minimization of the energy, a potential with non-zero range can easily be introduced by replacing the contact term  $-WA^*$  by the energy

$$F_a \equiv \oint ds_1 ds_2 \sqrt{g}V(l), \quad (6.27)$$

where  $l = Z(s_1, s_2)$  is the local distance of the membrane segment with coordinates  $(s_1, s_2)$  from the wall. Here we assume that the interaction couples only to the membrane rather than to the enclosed liquid.

The shape equations and the boundary conditions get modified by this energy. So far, there has been no explicit calculation for 3D axisymmetric vesicles in such a potential even though this poses no principal problem. However, a closely related

system, the adhesion of 2D vesicles (Maggs and Leibler 1990) in such a potential with finite range has been investigated in considerable detail (Seifert 1991a). The essential results of this study can be understood by simple scaling considerations which have the virtue of being easily transferable to the 3D case (Seifert and Lipowsky 1993).

In this section, these scaling arguments for the 3D case are presented. Since these arguments do not depend on the details of the potential  $V(l)$ , we characterize such a potential by just two quantities, the range  $l_0$ , which also characterizes the location of the minimum, and the depth

$$V_0 \equiv -V(l_0) < 0 \quad (6.28)$$

at the minimum. The shape of minimal energy of a vesicle in such a potential can be classified into two cases depending on the range  $l_0$  and on the size of the vesicle  $R_0$ .

(1) For  $R_0 \lesssim l_0$ , i.e., for *small* vesicles or *long-range* potentials, the whole bound vesicle is exposed to the adhesion potential  $V(l)$ . The deviations from the free shape (with the same constraints) are significant, if the variation of the potential along the contour of the vesicle becomes comparable to the bending energy which scales as  $\sim$ . This happens at the potential strength  $V^0 = V_f^0$ , where

$$V_f^0 \sim l_0^2/R_0^4, \quad (6.29)$$

as can be estimated by expanding the potential around its minimum. Thus, for  $V^0 \ll V_f^0$ , the bound vesicle keeps more or less its free shape and gains an energy

$$\Delta F \sim -V^0 R_0^2, \quad (6.30)$$

compared to the energy of a free vesicle under the same constraints, while for  $V^0 \gtrsim V_f^0$  the adhesion potential deforms the free shape. A calculation of this specific shape would require solving the shape equations.

(2) For  $l_0 \ll R_0$ , i.e. for *large* vesicles or *short-range* potentials, only the adjacent part of the vesicle is exposed to the potential and one should recover the results for the contact potential case. In fact, the limiting behaviour for small  $l_0/R_0$  depends on the potential strength. (i) If  $V^0 > W_a$ , where  $W_a$  is the critical value for the adhesion transition found in the contact potential, the vesicle in the smooth potential  $V(Z)$  approaches, in the limit of small  $l_0/R_0$ , the same shape obtained for adhesion in a contact potential with strength  $W = V^0$ . In particular, the boundary condition (6.16) also evolves in this limit without being imposed. This limit has been considered explicitly for 2D vesicles (Seifert 1991a). (ii) For  $V^0 < W_a$ , the vesicle approaches, in the limit of small  $l_0/R_0$ , the free shape which satisfies the same constraints. It remains, however, *pinned* in the (narrow) potential minimum up to the limit  $l_0 = 0$  where, formally, it becomes pinned in only one point (Seifert 1991a). Indeed, the area which is actually exposed to the potential well vanishes as  $l_0 R_0$ . This yields the energy gain

$$\Delta F \sim -V^0 l_0 R_0, \quad (6.31)$$

for small  $l_0/R_0$  in the pinned state. If the adhesion transition found in a contact potential has been *discontinuous*, the finite range  $l_0$  leads to a transition between the bound and the pinned state at

$$V^0 = V_a^0(l_0, R_0), \quad \text{with } \lim_{l_0 \rightarrow 0} V_a^0(l_0, R_0) = W_a. \quad (6.32)$$

With increasing  $l_0$  (or decreasing  $R_0$ ), this discontinuous transition terminates in a critical point (Seifert 1991a). If the adhesion transition in the contact potential has been *continuous* the finite range  $l_0$  leads to a smooth crossover between the bound and the pinned state. The pinned state thus replaces the free state found for adhesion in a contact potential.

Since vesicles are finite systems, any bond state will eventually unbind through thermal activation. The concept of a bound mean shape is meaningful only if the energy difference  $\Delta F$  between the free and the bound state is large compared with the thermal energy  $T$ , i.e. for  $|\Delta F| \gg T$ . If this relation holds true, the bound state remains bound for exponentially long time scales.

As a criterion for a characteristic depth  $V^0 = V_u^0$  at which thermal activation sets in, we take the relation  $|\Delta F(V_u^0)| \simeq T$ . With the estimates (6.30) and (6.31), one obtains (Seifert and Lipowsky 1993)

$$V_u^0 \sim \begin{cases} T/R_0^2, & \text{for } R_0 \lesssim l_0, \\ T/(R_0 l_0), & \text{for } l_0 \ll R_0 \lesssim R_c \equiv (\kappa/T)l_0. \end{cases} \quad (6.33)$$

The length scale  $R_c$  arises from the consistency requirement that  $V^0 < V_a^0 \simeq W_a$ , which was assumed when using the estimate (6.31) for  $\Delta F$ . The breakdown of this relation for  $R_0 > R_c$  indicates that large vesicles will not enter the pinned regime because the energy gain  $\Delta F$  of such a pinned state would be smaller than the thermal energy  $T$ . Therefore, these large vesicles unbind at values of the potential depth  $V^0$  for which the analysis at  $T = 0$  would predict bound vesicles with finite contact area. The unbinding of these large vesicles due to thermal fluctuations of their bound part is described next.

### 6.5. Self-consistent theory

Within the macroscopic description with the contact potential of section 6.3 it is assumed that the strength of the adhesion potential is given. Likewise, if the shape is calculated in a potential of finite range as discussed in section 6.4, the potential has to be known. However, as discussed in section 6.2 above, fluctuations contribute to the repulsive part of such a potential. Intuitively, it is clear that the weaker the direct attraction becomes, the weaker the effective tension is on this part and the more it fluctuates, thus further contributing to steric repulsion. In a consistent theory the binding potential and the fluctuations of a bound vesicle have to be treated on the same level.

The key idea consists of matching the description of a bound vesicle on a macroscopic and a mesoscopic length scale (Seifert 1995d). On the macroscopic scale, a bound vesicle is described as in section 6.3. This description yields the relation (6.19) between the Lagrange multiplier  $\bar{\Sigma}$  and the strength of the contact potential  $W$ .

On a *mesoscopic* level, the bound part of the vesicle is subject both to direct interactions and steric repulsion which create an effective potential as described in section 6.2. For a bound state to occur, this potential  $V(\Sigma; l)$  has to have a minimum at a separation  $l_0$  where

$$V'(l_0) \equiv dV(\Sigma; l)/dl|_{l=l_0} = 0. \quad (6.34)$$

The depth of this minimum,  $V_0 \equiv -V(l_0) > 0$ , becomes a function of the tension or, vice versa, the tension is a function of the depth  $\Sigma = \Sigma(V_0)$ .

The self-consistency requirement is simply that

$$\bar{\Sigma}(W = V_0) = \Sigma(V_0). \quad (6.35)$$

For this tension, the tension caused by the adhesion (in connection with the area constraint) equals the lateral tension for a planar membrane required to create an effective potential that has the correct depth to yield this adhering shape. The formal justification for this apparently obvious condition rests on two facts. (i) The Lagrange multiplier terms introduced into the *first* variation to ensure the constraints, act like a real energy for Gaussian fluctuations (calculated from the *second* variation), as discussed for free vesicles in section 4.1. (ii) In the limit where the range of the mesoscopic potential becomes much smaller than the size of the vesicle, the macroscopic shape calculated in such a potential with depth  $-V(l_0)$  approaches the shape calculated in a contact potential of strength  $W = -V(l_0) > 0$ , as discussed in section 6.4.

The self-consistent solution for a bound vesicle has been illustrated (Seifert 1995d) for a class of direct attractive potentials

$$V_d(l) \equiv -\frac{A/l_1^2}{(l/l_1 + 1)^n}. \quad (6.36)$$

The amplitude  $A$  is a generalized Hamaker constant and the length scale  $l_1$  is of the order of the bilayer thickness. This parametrization covers the classical van der Waals case in half-space approximation for  $n = 2$ , but also the asymptotic behaviour of a membrane in the vicinity of a semi-infinite substrate for large  $l$  where  $n = 3$  (or 4 if retardation effects are included). It is convenient to introduce the scaled amplitude  $H \equiv A\kappa/6b^2T^2$  and the scaled length scale  $z \equiv l/l_1$  with  $z_0 \equiv l_0/l_1$ . For a tensionless membrane in the potential (6.36), superposition with the Helfrich potential yields an unbinding transition at  $H = H_u \equiv (n/2)^n(n/2 - 1)^{2-n}$ , which is first order for  $n > 2$  and second order for  $n = 2$ . For  $H > H_u$ , the membrane is bound at  $z = z_0(H)$ . For any non-zero tension, a membrane in this potential is bound for all  $H > 0$ .

For a bound vesicle, the three equations (6.19), (6.34) and (6.35) have to be solved with  $V = V_f + V_d$ , where  $V_d$  is the direct potential. For the model potential (6.36), this solution follows in parametric form as

$$H(y) = y^2 \frac{1 + a \sinh^2(y)}{g^2(y)[1 - g(y)]^{n-2} \sinh^2(y)}, \quad (6.37)$$

and  $z_0(y) = g(y)/[1 - g(y)]$ , where  $g(y) \equiv 2y/\{n \tanh(y)[1 + a \sinh^2(y)]\}$ . Eliminating the scaling variable  $y$  which contains the unknown tension, yields  $z_0(H)$ . Two regimes must be distinguished depending on the value of the parameter

$$a \equiv 2\gamma(w, v)\kappa/3bT. \quad (6.38)$$

The function  $\gamma(w, v)$  has been introduced generally in (6.19) and becomes  $1 - \cos \Psi_{\text{eff}}(v)$  for large  $w \gg 1$ .

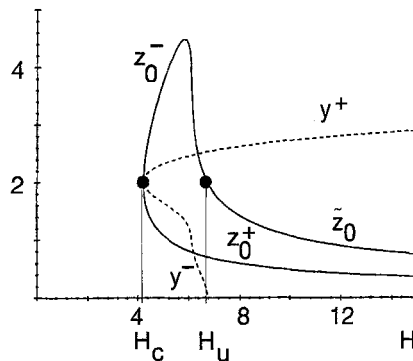


Figure 29. Separation  $z_0$  and scaling variable  $y$  (dashed curve) of a bound vesicle as a function of the scaled potential strength  $H$  for  $n = 3$  and  $\alpha = 0.08$ . Tension-induced adhesion occurs for  $H_c < H < H_u$ , where two solutions ( $z_0^\pm, y^\pm$ ) are found. For  $H > H_u$ , only the  $^+$  solution survives. In this range, the separation  $\tilde{z}_0$  of a tensionless membrane is given for comparison (Seifert 1995d).

(1) *Regular adhesion* ( $\alpha > 1/3$ ). For  $\alpha > 1/3$ , one finds a solution for a bound vesicle provided the amplitude obeys  $H > H_u$ . Thus, whenever  $\alpha > 1/3$ , adhesion of a vesicle is not qualitatively different from adhesion of a tensionless membrane even though the position of the minimum  $z_0(H)$  deviates somewhat from the value  $\tilde{z}_0(H)$  of a tensionless membrane.

(2) *Tension-induced adhesion* ( $\alpha < 1/3$ ). For  $\alpha < 1/3$ , genuine tension-induced adhesion becomes possible. One now finds (at least) two solutions for a bound vesicle in the range  $H_u > H > H_c(\alpha, n)$ , where a tensionless membrane would be unbound. As shown in figure 29 for  $n = 3$ , these solutions merge at  $H_c$  below which no solutions can be found. Thus, with decreasing amplitude  $H$ , the vesicle will unbind at  $H = H_c$  since for even smaller amplitudes the adhesion cannot create a tension large enough to bind the vesicle. Since the tension is still finite at the adhesion transition  $H = H_c$ , the first-order character of the transition should hold beyond the superposition approach. For regular adhesion, however, the tension vanishes for  $H \rightarrow H_u$ . In analogy to the unbinding of a tensionless membrane (Lipowsky and Leibler 1986, Lipowsky and Zielinska 1989), one would then expect that the adhesion transition becomes continuous if fluctuations are treated beyond superposition.

It turns out that the conditions under which the crucial parameter  $\alpha$  is smaller than the dividing value  $1/3$  are very restrictive (Seifert 1995d). Using both  $b = 1/2\pi$ , as appropriate in the tension-dominated regime, and a typical value for phospholipids  $\kappa/T = 25$ , one gets  $\alpha \approx 100 \gamma$ . Genuine tension-induced adhesion then requires  $\gamma \lesssim 0.003$ , which corresponds to a reduced volume of  $1 - v \lesssim 3 \times 10^{-6}$ , extremely close to the spherical limit. Thus, only vesicles with minute excess area can undergo tension-induced adhesion. The maximal contact angle to be expected for tension-induced adhesion is  $\Psi_{\text{eff},\text{max}} \approx 0.1$ . If a bound vesicle exhibits any larger contact angle, one must conclude that its adhesion is not induced by tension but rather that a tensionless membrane subject to the same potential would also be bound, albeit at a somewhat different separation  $\tilde{z}_0(H)$ .

This result can be related to the observation that in dilute samples the approximately constant effective contact angle  $\Psi_{\text{eff}} \approx 2\pi/3$  cannot be consistently explained assuming tension-induced adhesion in a direct van der Waals potential

( $n = 2$ ) (Servuss and Helfrich 1989). While in this geometry the origin of the lateral tension is somewhat obscure, one obtains a quite similar result for the well-defined geometry of a closed vesicle. If one insists on the assumption that these membranes are unbound in the absence of a tension, there is a serious discrepancy (Helfrich 1995).

The self-consistent theory should also be applicable to experiment (Rädler *et al.* 1995). Vesicles were filled with a slightly denser fluid so that they sank to the bottom of the chamber. Both the macroscopic shape and the fluctuations of the bound part of the vesicles were recorded. From the latter, a tension in the range  $5 \times 10^{-3}$ – $10^{-1}$  erg cm $^{-2}$  was derived. On the other hand, van der Waals attraction at the measured separation  $l_0 \simeq 40$  nm was estimated to be about 10 $^{-6}$  erg cm $^{-2}$ . While this should be an upper estimate on the adhesion energy, data derived from the Young–Dupré relation led to adhesion energies up to the order of  $5 \times 10^{-5}$  erg cm $^{-2}$ . Thus, tension is at least 2 (if not 3 or 4) orders of magnitude larger than adhesion energy. Within the theory discussed above, an inevitable consequence of such an enormous ratio would be a tiny area of contact with  $R^*/R_0 \approx \Psi_{\text{eff}} \approx (2W/\Sigma)^{1/2} \simeq 0.1$ – $0.01$ , contrary to the reported value of  $R^*/R_0 \gtrsim 1/4$ . Thus, the results of this experiment are (as yet) incompatible with the theory, even if gravity is taken into account (Seifert 1995d).

### 6.6. Adhesion under gravity

Gravity can have a significant but so far somewhat neglected effect on vesicle shapes. Its effect arises from the frequently employed experimental technique to stabilize the vesicle at the bottom of the measurement chamber by a difference in density between the fluids inside and outside the vesicle. Mostly, this is done by solution of different sugars with equal osmolarity, but different specific weights (Döbereiner 1995).

A simple scaling argument reveals the relevance of gravitational energy even for the small density differences usually employed (Kraus *et al.* 1995). Whereas the curvature energy is scale invariant, adhesion energies behave as  $F_{\text{adh}} \propto R_0^2$ . However, the gravitational energy scales as  $F_{\text{grav}} \propto R_0^4$ , because it is proportional to the volume multiplied by the height of the centre of mass of the vesicle above the substrate. The dimensionless gravity parameter

$$g \equiv \frac{g_0 \Delta \rho R_0^4}{\kappa}, \quad (6.39)$$

measures this effect. Here,  $g_0 \simeq 9.81$  m s $^{-2}$  is the acceleration due to gravity and  $\Delta \rho$  denotes the density difference between the fluids inside and outside the vesicle. Typical values for the latter are around 0.01–0.1 g cm $^{-3}$ , i.e. a few percent of the density of water. Giant vesicles can reach a size of  $R_0 \simeq 5$ – $50$   $\mu\text{m}$ . With  $\kappa \simeq 10^{-19}$  J  $\simeq 25k_B T$ , one obtains values of 0.5–50 000 for  $g$ . Thus, for giant vesicles, the gravitational energy can be varied over a large range.

For a theoretical description, one adds

$$F_g - WA^* \equiv g \int dV Z - WA^*, \quad (6.40)$$

to the curvature energy. The coordinate  $Z$  denotes the height of a volume element above the substrate.

The behaviour for very small and very large gravitational energies may be understood by simple arguments (Kraus *et al.* 1995). A vesicle filled with a fluid that is only slightly denser than the surrounding fluid, i.e. for small  $g$ , will always touch the bottom of the measurement chamber but will not necessarily form a finite contact area but rather a pinned state, in which the vesicle touches the wall only at a single point. A contact area of finite size will be formed, as soon as the cost in bending energy which is necessary in order to form this area is balanced by a gain in gravitational energy. The criterion for the transition from the pinned state to a bound state then follows from the boundary condition (6.16), which is still valid in the presence of gravity. For vanishing adhesion energy, i.e.  $w = 0$ , this condition becomes  $1/R_1^* = 0$ . The continuous adhesion transition between the pinned state and a bound state with finite contact area occurs when  $g$  reaches a critical value where the vesicle is deformed into a shape which has vanishing mean curvature at the contact point. Varying  $w$  yields a whole line of adhesion transitions at  $g = g_{\text{adh}}(w)$ . Numerically, one finds  $g_{\text{adh}}(w=0) \simeq 0.45$  for  $C_0 = 0$  without volume constraint. For  $g = 0$ , adhesion happens at  $w = 2$  induced just by the contact potential.

The behaviour for large  $g$  is different from the large- $w$  limit in which a spherical cap is obtained. In the limit of high gravitational energy, bending is also irrelevant, but now—given that the volume is fixed—the shape of least energy is that of a flat disc.

For general  $g$ , the corresponding shape equations must be solved. Since non-axisymmetric shapes can also become relevant, they have been included in the study (Kraus *et al.* 1995) by numerically minimizing curvature energy and gravity with the surface evolver program (Brakke 1992). The phase diagram thus obtained is shown in figure 30. It contains a ‘tricritical’ point at  $v = v_{\text{tr}} \simeq 0.88$  that separates a

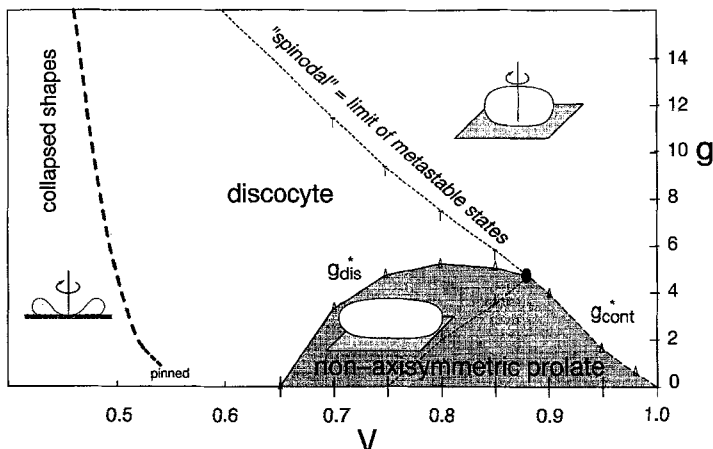


Figure 30. Phase diagram for adhering vesicles as a function of the gravitational parameter  $g$  and the reduced volume  $v$ . Non-axisymmetric shapes and the large-volume transition are computed using the surface evolver program, while axisymmetric shapes are solutions of the Euler-Lagrange equations with  $w = 0$ . The transition  $g^*(v)$  between the non-axisymmetric prolates and the discocytes is discontinuous for  $v < v_{\text{tr}} \simeq 0.88$  (full line) and continuous for  $v > v_{\text{tr}}$  (dashed line) separated by a tricritical point (black dot). For the discontinuous transition, the limit curves of metastable states or spinodals are shown in the figure by dashed lines. On the small- $v$  side of the phase diagram, collapsed shaped become relevant (Kraus *et al.* 1995).

discontinuous transition for  $\nu < \nu_{tr}$  from a continuous transition for  $\nu > \nu_{tr}$ . This transition separates axisymmetric shapes for large  $g$  from non-axisymmetric prolates for small  $g$ . For small volume  $\nu$  and intermediate  $g$ , self-adhesion, or cohesion, must be included with an additional energy  $W'A'$  where  $A'$  is the area of contact. This energy leads to ‘collapsed’ states with finite area of self-adhesion.

### 6.7. Focal adhesion

So far, we have been assuming a laterally homogeneous adhesion energy or binding potential. There are at least two experimental set-ups where adhesion or binding is induced only on one (or several distinct) points. In the laser pinching experiment, two originally almost parallel membrane sheets are ‘pinched’ together by a laser trap (Bar-Ziv *et al.* 1995b). In biological systems, adhesion is often induced by adhesion molecules which bind two membranes together locally (Chiruvolu *et al.* 1994, Moy *et al.* 1994, Evans 1995a).

Theoretically, one focal adhesion point can be modelled as follows. Let  $l(x, y)$  be the separation of two membranes in a Monge representation. An appropriate energy for small displacements from the parallel configurations is

$$F^a = \int dx dy \left[ \frac{\kappa}{2} (\nabla^2 l)^2 + V(l) \right]. \quad (6.41)$$

Two regimes can be distinguished (Bruinsma *et al.* 1994). In the so-called van der Waals regime, the potential  $V(l)$  is expanded harmonically around a minimum at  $l = l_0$ . By minimizing the energy for boundary condition  $h(0) = 0$  and  $h(r \rightarrow \infty) = l_0$  the axisymmetric distance profile  $h(r)$  can be expressed by a Kelvin function. In the so-called Helfrich regime,  $V(l) \sim T^2/\kappa l^2$  is used in an attempt to include fluctuations self-consistently. Beyond a core, one then finds a self-similar cone profile  $h(r) \sim (T^2/\kappa)^{1/2} r$ .

In order to keep the membranes asymptotically at finite distance even in the presence of Helfrich repulsion, a linear pressure term  $\sim pl$  can be added to (6.41). Characteristic for the numerical solution for the separation profile (Bar-Ziv *et al.* 1995b) is an over-shooting which arises from the fourth order of the corresponding Euler-Lagrange equations.

A collection of focal adhesion points can exhibit cooperative behaviour (Bruinsma *et al.* 1994). In both the van der Waals and the Helfrich regimes focal points experience an effective attraction because of membrane rigidity and membrane fluctuations. For a membrane under tension, thermal fluctuations can assist adhesion in the presence of reversible focal adhesion points which model reversible binding molecules (Zuckerman and Bruinsma 1995). Whether this property persists if steric membrane repulsion is included remains to be investigated.

## 7. Dynamics

Configurational changes of vesicles comprise two conceptually different aspects. First, thermal agitation generates dynamical equilibrium fluctuations around the shape of lowest energy. Since the typical time scale for large wavelength fluctuations of micron-size vesicles is of the order of seconds, these fluctuations can be seen with video microscopy. Second, in any discontinuous shape transformation an unstable shape decays towards the new minimum by an essentially deterministic motion. In both cases, the presence of the surrounding liquid in which the membrane is

embedded determines the dynamics in an important non-trivial way, since it generates an effective long-range dynamical interaction along the membrane.

In this section, basic aspects of the collective dynamics of the bilayer and the embedding liquid are discussed within linearized theories for various geometries. The full nonlinear formulation of membrane dynamics for arbitrary geometry has just recently been worked out formally (Cai and Lubensky 1995), but has not yet been applied to fluctuations of non-trivial shape or instabilities. In section 7.1, the hydrodynamic equations for the coupled system comprising membrane and surrounding fluid are introduced. Eliminating the viscous liquid leads to a non-local equation of motion for the membrane. In section 7.2, we use this equation to recall the dynamical fluctuations of an almost planar membrane in the classical model where dissipation arises from the viscous damping in the liquid alone (Kramer 1971, Brochard and Lennon 1975).

A second source of dissipation has been appreciated just recently (Evans *et al.* 1992, Seifert and Langer 1993). This process arises from the dynamical counterpart of the area-difference elasticity introduced in section 2.3: local inhomogeneities of the lipid density in the neutral surface of each monolayer caused by sudden bending of the bilayer can relax laterally, if the two leaflets slide over each other. In section 7.3 it is shown that friction in the tail region of the hydrocarbon chains between the leaflets fundamentally alters the relaxation spectrum or the shape fluctuations below a mesoscopic length scale (Seifert and Langer 1993). Section 7.4 is devoted to dynamical shape fluctuations of quasi-spherical vesicles. The dynamical fluctuations of the bound part of an adhering vesicle (Seifert 1994) are discussed in section 7.5; in this geometry, quantitative measurements of collective dynamical processes have become feasible just recently (Rädler 1993). The dynamics of a shape transformation will be discussed for the laser-induced pearling instability of cylindrical vesicles (Bar-Ziv and Moses 1994) in section 7.6.

### 7.1. Equations of motion

An equation of motion for the membrane can be derived by starting from the Navier–Stokes equations for the surrounding viscous liquid and introducing the membrane later. The Navier–Stokes equations for the velocity field  $\mathbf{v}(\mathbf{r})$  of the solvent with density  $\rho_f$  and viscosity  $\eta$  are given by

$$\frac{d}{dt}(\rho_f \mathbf{v}) + \nabla p - \eta \nabla^2 \mathbf{v} = \mathbf{K}(\mathbf{r}), \quad (7.1)$$

where  $p(\mathbf{r})$  denotes the pressure, and  $\mathbf{K}(\mathbf{r})$  are the external forces acting on the liquid. These include both forces exerted from the membrane and forces due to confining boundaries, such as the presence of a substrate in the case of adhesion.

To a very good approximation, the inertial term in the Navier–Stokes equation can be neglected for the range of phenomena in which we are interested. As can be checked *a posteriori*, the corresponding Reynolds numbers are small compared with 1. In the so-called Stokes approximation, one then has to solve the force balance

$$\nabla p - \eta \nabla^2 \mathbf{v} = \mathbf{K}(\mathbf{r}). \quad (7.2)$$

Moreover, for these phenomena, the liquid can be considered as incompressible, i.e.

$$\nabla \cdot \mathbf{v} = 0, \quad (7.3)$$

which can be used to eliminate the pressure in (7.2) in favour of the forces.

These equations are solved formally by introducing the Fourier transformation as

$$\mathbf{v}_\mathbf{k} = \int \exp(-i\mathbf{k} \cdot \mathbf{r}) \mathbf{v}(\mathbf{r}) d^3 r \quad (7.4)$$

and

$$\mathbf{K}_\mathbf{k} = \int \exp(-i\mathbf{k} \cdot \mathbf{r}) \mathbf{K}(\mathbf{r}) d^3 r. \quad (7.5)$$

The solution to (7.2) and (7.3) then becomes a linear relationship

$$v_{ki} = \frac{1}{\eta k^2} \left( \delta_{ij} - \frac{k_i k_j}{k^2} \right) K_{kj} \quad (7.6)$$

between the velocity field and the external forces, where  $i, j$  denote Cartesian components. ( $v_{ki}$  is short for  $(\mathbf{v}_\mathbf{k})_i$  to keep the notation simple). In real space, relation (7.6) reads

$$\mathbf{v}(\mathbf{r}) = \int d^3 r' \mathcal{O}(\mathbf{r}, \mathbf{r}') \mathbf{K}(\mathbf{r}'), \quad (7.7)$$

where the Oseen tensor  $\mathcal{O}(\mathbf{r}, \mathbf{r}')$  has matrix elements (Doi and Edwards 1986)

$$O_{ij}(\mathbf{r}, \mathbf{r}') \equiv \frac{1}{8\pi\eta|\mathbf{r} - \mathbf{r}'|} \left[ \delta_{ij} + \frac{(r_i - r'_i)(r_j - r'_j)}{|\mathbf{r} - \mathbf{r}'|^2} \right]. \quad (7.8)$$

Thus, the hydrodynamics generates a long-range interaction ( $\sim 1/|\mathbf{r} - \mathbf{r}'|$ ) through the velocity field.

Since essentially no liquid penetrates the membrane, as discussed in section 1.3, we can identify the normal velocity of the liquid,  $\mathbf{v}[\mathbf{R}(s_1, s_2)] \cdot \mathbf{n}(s_1, s_2)$ , at any point  $\mathbf{R}(s_1, s_2)$  of the membrane with a configurational change of the membrane. Thus, we obtain a dynamical equation of motion for the membrane as

$$\partial_t \mathbf{R}(s_1, s_2, t) \cdot \mathbf{n}(s_1, s_2, t) = \mathbf{n}(s_1, s_2, t) \cdot \int d^3 r' \mathcal{O}(\mathbf{r}, \mathbf{r}') \mathbf{K}(\mathbf{r}'). \quad (7.9)$$

The crucial quantity is the force density  $\mathbf{K}(\mathbf{r})$  exerted from the membrane (and container walls in confined geometries) upon the liquid. In general, this force density has normal and tangential components. Both curvature energy and tension contribute to the normal component while the tangential components are dominated by forces within the membrane, such as lateral tension gradients. Such an inhomogeneous tension can arise from the local incompressibility of the membrane. For a compressible membrane, the density as an additional variable has its own equations of motion. The tangential forces have to be determined self-consistently from no-slip boundary conditions between membrane and embedding liquid.

For an arbitrary membrane configuration, geometry complicates the problem even further. A fluid membrane has to obey reparametrization invariance. Stochastic forces have to be introduced to describe the thermal fluctuations. The correlator of these forces has to be chosen properly to ensure that such a dynamics obeys the correct equilibrium. A general formulation of membrane hydrodynamics which takes care of all these subtleties has recently been given by (Cai and Lubensky 1995). In this paper, the formalism was applied to show that incompressible membranes become effectively compressible on longer scales because of thermal fluctuations. The dynamical viscosity of the liquid, however, was shown not to be renormalized.

In polymer dynamics (Doi and Edwards 1986), the model just described would be called a Zimm model since the main dissipation arises in the embedding liquid where back flow effects are relevant. For membranes, a Rouse model for which the dissipation is local is physically not very meaningful. Many formal issues, however, can also be studied for such a simpler Rouse dynamics (Foltin 1994, Cai and Lubensky 1994).

Membrane hydrodynamics becomes much simpler if only small configurational changes around a simple mean shape are considered, as we now do in the following. From a practical point of view, such a narrower focus is still sufficient to discuss basically all available quantitative experiments on membrane dynamics.

### 7.2. Almost planar membrane: classical model

As an instructive example, we first recall the relaxation of small displacements  $h(x, y, t)$  of an almost planar membrane around its equilibrium position at  $z = 0$  within the classical model, which will be derived here in a somewhat different approach than given in the original work (Brochard and Lennon 1975).

In a planar geometry, it is convenient to apply a Fourier transformation parallel to the membrane plane according to

$$\mathbf{v}_q(z) = \int \exp(-iq \cdot \mathbf{x}) \mathbf{v}(\mathbf{r}) d\mathbf{x} \quad (7.10)$$

and

$$\mathbf{K}_q(z) = \int \exp(-iq \cdot \mathbf{x}) \mathbf{K}(\mathbf{r}) d\mathbf{x}, \quad (7.11)$$

where  $\mathbf{r} = (\mathbf{x}, z) = (x, y, z)$ . Moreover, one can decompose the velocity and the force fields into their  $z$ , longitudinal and transverse components as

$$\mathbf{v}_q(z) \equiv v_{qz}(z) \hat{\mathbf{z}} + v_{ql}(z) \hat{\mathbf{q}} + v_{qt}(z) \hat{\mathbf{t}}, \quad (7.12)$$

and

$$\mathbf{K}_q(z) \equiv K_{qz}(z) \hat{\mathbf{z}} + K_{ql}(z) \hat{\mathbf{q}} + K_{qt}(z) \hat{\mathbf{t}}, \quad (7.13)$$

where  $\hat{\mathbf{q}}$  is the unit vector parallel to  $\mathbf{q}$ , and  $\hat{\mathbf{t}}$  is the in-plane vector perpendicular to  $\mathbf{q}$  and  $\hat{\mathbf{z}}$ .

Inserting these expressions for the Fourier-transformed quantities into the relation (7.6) yields, with little algebra, the relationship between velocity and force components as

$$v_{\mathbf{q}z}(z) = \frac{1}{4\eta q} \int_{-\infty}^{\infty} dz' \exp(-q|z-z'|)[(1+q|z-z'|)K_{\mathbf{q}z}(z') + iq(z'-z)K_{\mathbf{q}l}(z')], \quad (7.14)$$

$$v_{\mathbf{q}l}(z) = \frac{1}{4\eta q} \int_{-\infty}^{\infty} dz' \exp(-q|z-z'|)[(1-q|z-z'|)K_{\mathbf{q}l}(z') + iq(z'-z)K_{\mathbf{q}z}(z')], \quad (7.15)$$

and

$$v_{\mathbf{q}l}(z) = \frac{1}{4\eta q} \int_{-\infty}^{\infty} dz' \exp(-q|z-z'|)2K_{\mathbf{q}l}(z'). \quad (7.16)$$

Since the transverse components do not couple to the normal displacements in this geometry, they can be ignored in the following.

For small displacements around the almost planar membrane the restoring forces are small and proportional to  $h$ . Therefore, they can be assumed to act only in the plane  $z = 0$ , since the fact that they act at the local position  $h(x, y, t)$  of the membrane is an effect of higher order. For such a force density,

$$K_{\mathbf{q}z}(z) \equiv \delta(z)[K_{\mathbf{q}z}\hat{\mathbf{z}} + K_{\mathbf{q}l}\hat{\mathbf{q}}], \quad (7.17)$$

and the relations (7.14) and (7.15) immediately yield a decoupling of the  $z$  and the longitudinal components according to

$$v_{\mathbf{q}r}(0) = \frac{1}{4\eta q} K_{\mathbf{q}r}, \quad \text{with } r = z \text{ or } l. \quad (7.18)$$

For the classical model, the normal force  $K_{\mathbf{q}z}$  is given by the derivative of the bending energy  $F_0$  (as introduced in (13)) as

$$K_{\mathbf{q}z} = -\frac{\partial F_0}{\partial h_{\mathbf{q}}^*} = -E_0(q)h_{\mathbf{q}} = -\kappa q^4 h_{\mathbf{q}}. \quad (7.19)$$

If the normal velocity at the membrane is identified with the time derivative of  $h$ , i.e.

$$\partial_t h_{\mathbf{q}} = v_{\mathbf{q}z}(0), \quad (7.20)$$

one obtains from relation (7.18) the equation of motion for the membrane in the form

$$\partial_t h_{\mathbf{q}} = -\Gamma_0(q)E_0(q)h_{\mathbf{q}}. \quad (7.21)$$

The ‘kinetic coefficient’

$$\Gamma_0(q) = 1/4\eta q \quad (7.22)$$

reflects the long-range character of the hydrodynamic damping. In the solution to this equation of motion,

$$h_{\mathbf{q}}(t) = h_{\mathbf{q}}(0) \exp[-\gamma_0(q)t], \quad (7.23)$$

the damping rate  $\gamma_0(q)$  is easily identified as

$$\gamma_0(q) = \Gamma_0(q)E_0(q) = \kappa q^3 / 4\eta. \quad (7.24)$$

The form (7.24) of the damping rate as a product (Marathe and Ramaswamy 1989) of a kinetic coefficient which contains the dissipation, and an energy which contains the driving force, is characteristic of the low Reynolds number viscous dynamics. It persists if we take the bilayer aspect of the membrane into account, as well as for a bound or cylindrical membrane.

So far, the dynamics has been strictly deterministic. In order to obtain dynamical equilibrium functions one should first add stochastic forces to the equation of motion (7.1) and then average over an appropriate ensemble. Within a linear theory, however, the usual short-cut works. Multiplying the solution (7.23) with  $h_{\mathbf{q}'}^*(0)$  and averaging with the Boltzmann weight  $\exp(-F_0/T)$  yields the dynamical equilibrium fluctuations as

$$\langle h_{\mathbf{q}}(t)h_{\mathbf{q}'}^*(0) \rangle = \frac{T}{\kappa q^4} \exp[-\gamma_0(q)t] (2\pi)^2 \delta(\mathbf{q} - \mathbf{q}'). \quad (7.25)$$

### 7.3. Almost planar membrane: bilayer dynamics

#### 7.3.1. Force balance

If the membrane is described in the refined bilayer model introduced in section 2.3, the normal force is given by

$$K_{\mathbf{q}z} = -\frac{\partial F}{\partial h_{\mathbf{q}}^*} = -[\tilde{\kappa}q^4 h_{\mathbf{q}} - 2kdq^2 \rho_{\mathbf{q}}], \quad (7.26)$$

where the bilayer energy  $F$  was defined in (2.28). If this force density is inserted into (7.18), one obtains with (7.20) the equation of motion for the height variable

$$\partial_t h_{\mathbf{q}} = -\Gamma_0(q)[\tilde{\kappa}q^4 h_{\mathbf{q}} - 2kdq^2 \rho_{\mathbf{q}}], \quad (7.27)$$

which involves the local density difference  $\rho$ . To obtain a closed system of equations, we need a dynamical equation for this density difference.

Such an equation of motion can be obtained from the in-plane force balance within each monolayer (Seifert and Langer 1993),

$$-\tilde{\nabla}\sigma^{\pm} \pm T_{xz}^{\pm} \mp b(\tilde{\mathbf{v}}^+ - \tilde{\mathbf{v}}^-) + \mu\tilde{\nabla}^2\tilde{\mathbf{v}}^{\pm} = 0, \quad (7.28)$$

where the tilde refers to 2D quantities. The four force densities in (7.28) are as follows.

(1) The (in-plane) gradient of the surface pressure

$$-\tilde{\nabla}\sigma^{\pm} = -\tilde{\nabla} \frac{\delta F}{\delta \rho^{\pm*}}, \quad (7.29)$$

which arises from the elastic stretching or compression within each monolayer.

(2) The tractions  $T_{xz}^\pm$  of the surrounding fluid, which have the same magnitude as, but different sign from the (as yet unknown) tangential forces  $K_{ql}^\pm = 4\eta q v_{ql}^\pm(0)$  exerted by the membrane on the liquid.

(3) The friction between the two monolayers with the phenomenological friction coefficient  $b$  (Evans *et al.* 1992, Yeung 1994). The justification for describing this friction as viscous arises from the fast motion of the dangling ends of the hydrocarbon-chains, which dynamically interdigitate slightly on a relatively fast time scale, of the order of  $10^{-9}$  s, as shown by molecular dynamics simulations (de Loof *et al.* 1991). This fast molecular motion of the dangling ends should give rise to an effectively viscous friction on the much slower time scale of typical shape changes (Yeung 1994).

(4) A viscous shear damping within each monolayer where  $\mu$  is the monolayer shear viscosity and  $\tilde{\mathbf{v}}^\pm$  is the velocity of the lipid flow within each monolayer. For simplicity, and since this damping mechanism will turn out to be irrelevant except on very small length scales, any dilational viscosity can be ignored. For the insoluble phospholipids, dilational viscosity can be expected to be of the same order as the shear viscosity, whereas for soluble monolayers the dilational viscosity can be two orders of magnitude larger (Langevin 1992).

The densities  $\rho^\pm$  obey equations of continuity

$$\partial_t \rho^\pm \approx -\tilde{\nabla} \cdot \tilde{\mathbf{v}}^\pm \quad (7.30)$$

to lowest order in the small quantities  $\rho^\pm$  and  $\tilde{\mathbf{v}}^\pm$ .

Assuming conventional non-slip boundary conditions between liquid and membrane flow, i.e.  $\tilde{\mathbf{v}}^\pm = v_{ql}^\pm(0)\hat{\mathbf{q}}$ , the equation of continuity (7.30) can be used to replace the velocities in the force balance (7.28). The difference of the two equations (7.28) then leads, after Fourier transformation, to the equation of motion for the density difference  $\rho_q$ . This equation and the corresponding one for  $h_q$  can be written in the form (Seifert and Langer 1994)

$$\frac{\partial}{\partial t} \begin{pmatrix} h_q \\ \rho_q \end{pmatrix} = -\Gamma(q)\mathbf{E}(q) \begin{pmatrix} h_q \\ \rho_q \end{pmatrix}. \quad (7.31)$$

Here,  $\mathbf{E}(q)$  is the upper left  $(2 \times 2)$  submatrix of  $\mathbf{E}(q)$  as defined in (2.29) for which we will not introduce a new notation. The matrix of kinetic coefficients

$$\Gamma(q) \equiv \begin{pmatrix} 1/4\eta q & 0 \\ 0 & \frac{q^2}{2(2b + 2\eta q + \mu q^2)} \end{pmatrix} \quad (7.32)$$

shows that, for small  $q$ , the dissipation for the density difference mode is dominated by the inter-monolayer friction with coefficient  $b$ . It has a  $q^2$ -dependence because the densities are conserved and the friction is local.

The dynamical equation for the average density  $\bar{\rho}_q$ , which also follows from this procedure should not be taken seriously since for this quantity the inertial terms are crucial to the dynamics. Including the inertial terms within the membrane leads to propagating sound-waves in  $\bar{\rho}_q$  (Seifert and Langer 1993).

### 7.3.2. Dispersion relation and height–height correlation function

The formal solution to the relaxational dynamics (7.31) is

$$\begin{pmatrix} h_{\mathbf{q}}(t) \\ \rho_{\mathbf{q}}(t) \end{pmatrix} = \exp(-\Gamma \cdot \mathbf{E} t) \begin{pmatrix} h_{\mathbf{q}}(0) \\ \rho_{\mathbf{q}}(0) \end{pmatrix}. \quad (7.33)$$

After diagonalization, the relaxation times of the various modes follow as the inverse values of the eigenvalues  $\gamma_i$  of  $\Gamma \cdot \mathbf{E}$ , while the time-dependent correlation functions can be obtained from the corresponding eigenvectors.

The dispersion relation of the two eigenvalues  $\gamma_{1,2}(q)$  is shown in figure 31. There are three regimes (Seifert and Langer 1993) separated by the crossover wave-vectors  $q_1 \equiv 2\eta k/b\tilde{\kappa}$  and  $q_2 \equiv (2b/\mu)^{1/2}$

$$\gamma_1 \approx \begin{cases} \frac{\kappa}{4\eta} q^3, & q \ll q_1, \\ \frac{k}{2b} \frac{\kappa}{\tilde{\kappa}} q^2, & q_1 \ll q \ll q_2, \\ \frac{k}{\mu} \frac{\kappa}{\tilde{\kappa}}, & q_2 \ll q. \end{cases} \quad \gamma_2 \approx \begin{cases} \frac{k}{2b} q^2, & q \ll q_1, \\ \frac{\tilde{\kappa}}{4\eta} q^3, & q_1 \ll q. \end{cases} \quad (7.34)$$

For the dynamical height–height correlation function, one finds

$$\langle h_{\mathbf{q}}(t) h_{\mathbf{q}'}^*(0) \rangle = \frac{T}{\kappa q^4} \{ A_1^h(q) \exp[-\gamma_1(q)t] + A_2^h(q) \exp[-\gamma_2(q)t] \} (2\pi)^2 \delta(\mathbf{q} - \mathbf{q}'). \quad (7.35)$$

Likewise, the density–density correlations become

$$\langle \rho_{\mathbf{q}}(t) \rho_{\mathbf{q}'}^*(0) \rangle = \frac{T\tilde{\kappa}}{2k\kappa} \{ A_1^\rho(q) \exp[-\gamma_1(q)t] + A_2^\rho(q) \exp[-\gamma_2(q)t] \} (2\pi)^2 \delta(\mathbf{q} - \mathbf{q}'). \quad (7.36)$$

The fluctuation–dissipation theorem enforces  $A_2^{h,\rho}(q) = 1 - A_1^{h,\rho}(q)$ . These amplitudes are also shown in figure 31.

The asymptotic behaviour of the damping rates and the correlation function can be understood as follows. For small  $q$ ,  $\gamma_1$  corresponds to the classical hydrodynamically damped bending mode  $\gamma_0$  (7.24) and  $\gamma_2$  is the damping rate of a new ‘slipping’ mode, a density difference fluctuation damped by the inter-monolayer friction. In this regime, undulations relax only by the slow mode, so  $A_1^h \approx 1$ , and  $A_2^h$  is negligibly small, since the height variable is too slow to follow the fast density fluctuations. A similar consideration applies to  $A_1^\rho$ ,  $A_2^\rho$  (Kraus and Seifert 1994).

For  $q \gg q_1$ ,  $\gamma_2$  becomes the damping rate of a bending mode, with an effective bending rigidity  $\tilde{\kappa}$  identified already in section 2.3 as the bending rigidity for ‘frozen’ lipid molecules (2.33). This effective high frequency rigidity differs from the low frequency rigidity  $\kappa$  because the densities cannot respond quickly to changes in shape. On time scales longer than  $1/\gamma_2$ , the height can relax so as to minimize the free energy for a given density fluctuation. This condition  $\partial F / \partial h_{\mathbf{q}}^*|_{\rho_{\mathbf{q}}} = 0$  implies  $h_{\mathbf{q}} = 2kd\rho_{\mathbf{q}}/\tilde{\kappa}q^2$ , and therefore

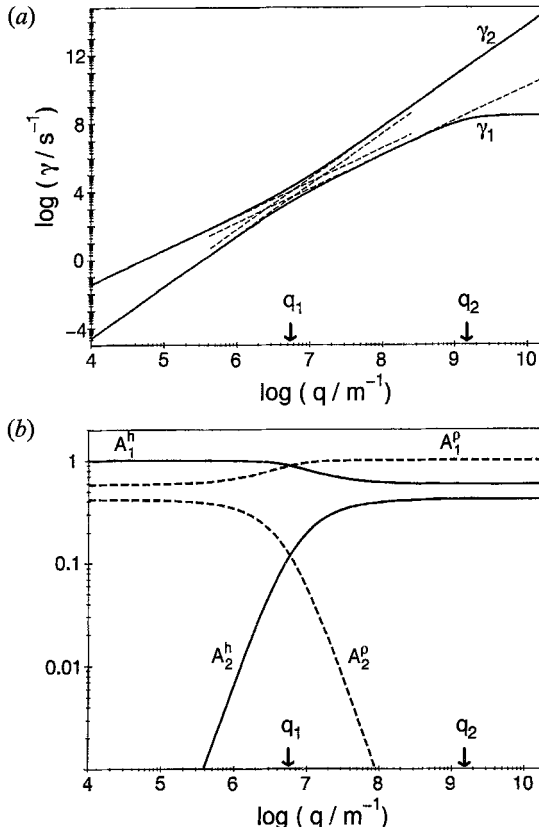


Figure 31. Dispersion relation (a) and amplitudes (b) for a free bilayer for  $\kappa = 10^{-19} \text{ J}$ ,  $\kappa = 0.07 \text{ J m}^{-2}$ ,  $d = 1 \text{ nm}$ ,  $\eta = 10^{-3} \text{ J s m}^{-3}$ ,  $\mu = 10^{-10} \text{ J s m}^{-2}$ , and  $b = 10^8 \text{ J s m}^{-4}$ ; the thin dashed lines in (a) indicate the asymptotic behaviour  $\gamma_1 \approx kq^3/4\eta$  and  $\gamma_2 \approx kq^2/2b$  for small  $q'$ , and  $\gamma_2 \approx \tilde{\kappa}q^3/4\eta$  and  $\gamma_1 \approx \tilde{\kappa}q^2\kappa/2b\tilde{\kappa}$  for large  $q$ , respectively. The ratio  $\kappa/\tilde{\kappa} \simeq 0.417$  determines the asymptotic behaviour of both the amplitudes  $A_2^p$  for small  $q$  and  $A_2^h$  for large  $q$  (Kraus and Seifert 1994).

$$\begin{aligned} \langle h_{\mathbf{q}}(t)h_{\mathbf{q}'}^*(0) \rangle \mathcal{N} &\approx \frac{4k^2 d^2}{\tilde{\kappa}^2 q^4} \langle \rho_{\mathbf{q}}(t)\rho_{\mathbf{q}'}^*(0) \rangle \mathcal{N} \approx \frac{4k^2 d^2}{\tilde{\kappa}^2 q^4} \frac{T\tilde{\kappa}}{2k\kappa} \exp(-\gamma_1 t) \\ &= \langle h_{\mathbf{q}} h_{\mathbf{q}'}^* \rangle_0 \mathcal{N} \frac{2kd^2}{\tilde{\kappa}} \exp(-\gamma_1 t), \end{aligned} \quad (7.37)$$

with  $\mathcal{N} \equiv (2\pi)^2 \delta(\mathbf{q} - \mathbf{q}')$ . Thus, the coefficient  $A_1^h(q)$  in the correlation function (7.35) is given by  $A_1^h \approx 2kd^2/\tilde{\kappa}$ , for  $q \gg q_1$ .

Finally, the slow mode  $\gamma_1$  exhibits a second crossover at  $q_2 \equiv (2b/\mu)^{1/2}$ , where the main dissipative mechanism changes from inter-monolayer friction to monolayer surface viscosity.

### 7.3.3. Experimental aspects

An important consequence of the results of the bilayer dynamics is that any experiment measuring  $\langle h_{\mathbf{q}}(t)h_{\mathbf{q}}(0) \rangle$  should also pick up a contribution from the slow

mode for  $q > q_1$ , provided it is sensitive to the time scale  $1/\gamma_1$ . In particular, the slowest time scale for shape fluctuations in this regime scales as  $q^{-2}$ , which differs from the  $q^{-3}$  behaviour of the classical model (7.24).

To estimate the crossover wavelengths  $q_1$  below which the monolayer friction becomes relevant, we need a value for the friction coefficient  $b$ . This quantity, or more precisely the combination  $4bd^2$  in our notation, has recently been measured by a nano-tether extrusion experiment for various lipids at different temperatures (Yeung 1994, Evans and Yeung 1994). From the typical value  $4bd^2 \simeq 2 \times 10^{-9} \text{ J s m}^{-2}$ , one derives  $b \simeq 5 \times 10^8 \text{ J s m}^{-4}$  with  $d = 1 \text{ nm}$ . Using this value, one finds with  $\kappa = 10^{-19} \text{ J}$ ,  $\eta = 10^{-3} \text{ J s m}^{-3}$ , and  $k = 10^2 \text{ mJ m}^{-2}$ , the crossover  $q_1 \simeq 10^6 \text{ m}^{-1}$ , corresponding to a wavelength of several microns, below which bilayer corrections to the dispersion relation for the bending mode should become important. For the second crossover, relevant only to the slower mode, we find  $q_2 \simeq 1-3 \times 10^7 \text{ cm}^{-1}$ , i.e. a wavelength somewhat above the membrane thickness using  $\mu \simeq 10^{-10} - 10^{-9} \text{ J s m}^{-2}$  derived from experiments using microfluorescence techniques (Merkel *et al.* 1989).

So far, the only experimental hint on the relevance of the second dissipative process for equilibrium fluctuations arises from neutron reflection spin echo measurement of the undulations of swollen phospholipid multi-layers (Pfeiffer *et al.* 1993). For a stack of swollen membranes and a wave-vector parallel to the sheets, the calculation of the dispersion relation for the collective undulation mode using the same force balance and boundary conditions at every membrane in a stack with repeat distance  $2l$  leads to two modes. For small  $q$ , both modes have a quadratic dispersion (Seifert and Langer 1993),

$$\gamma_1 \approx \frac{k \kappa}{2b\bar{\kappa}} q^2, \quad \text{and} \quad \gamma_2 \approx \frac{\bar{\kappa}}{2\eta l} q^2. \quad (7.38)$$

Here,  $\gamma_2$  corresponds to the undulation mode of a two-component smectic (Brochard and de Gennes 1975), which crosses over into the single-layer result for  $q \sim 1/l$ . The damping rate of the second slow mode  $\gamma_1$  has the same dispersion as the single bilayer in the intermediate  $q$  regime. At relatively large  $q \simeq 10^6-10^7 \text{ cm}^{-1}$ , the relaxation frequencies measured in the experiment fit well with this second mode. However, more work will clearly be needed to prove that in this measurement the dissipation is due to the bilayer aspect. For a crucial experimental test, the damping rate as a function of the repeat distance  $2l$  should be investigated. If the measured dispersion is indeed that of the frictional mode, the damping rate should be independent of the repeat distance, since the main dissipation for this mode occurs within the bilayer rather than in the liquid.

#### 7.4. Relaxation of quasi-spherical modes

Measurements of dynamical correlation functions in lipid bilayers have been performed for quasi-spherical vesicles (Engelhardt *et al.* 1985, Bivas *et al.* 1987, Duwe *et al.* 1990). For a theoretical analysis of these data, the dispersion relation has to be calculated for a spherical geometry. Within the classical model, the dynamical correlation functions for the flicker amplitudes as defined in (4.19) can be written as (Schneider *et al.* 1984b, Milner and Safran 1987)

$$\langle u_{l,m}^*(t) u_{l,m}(0) \rangle = \langle u_{l,m}^*(0) u_{l,m}(0) \rangle \exp[-\gamma(l)t]. \quad (7.39)$$

The relaxation rate

$$\gamma(l) \equiv \Gamma(l) E_0(l) \equiv \left[ \frac{1}{\eta R_0^3} \frac{l(l+1)}{(2l+1)(2l^2+2l-1)} \right] \{\kappa(l+2)(l-1)[(l+1)l + \bar{\sigma}]\} \quad (7.40)$$

is again a product of a kinetic factor and the energy known already from (4.30).

Since only the first few modes can be analysed experimentally, the effective tension cannot as yet be extracted from the correlation times. Likewise, these experiments are not accurate enough to find the ramification arising from the bilayer model of quasispherical vesicles (Yeung and Evans 1995). In this model, the correlation function decays with two exponential factors analogous to the correlation function of the almost planar membrane discussed in section 7.3. Qualitatively, the same crossover holds, i.e. short-wavelength bending fluctuations with  $q \sim l/R \gtrsim q_1$  show the effectively higher bending rigidity and a relaxation frequency  $\gamma \sim l^2$ . This result should have the important consequence that for scattering studies of vesicles that are smaller than the crossover length, the smallest relaxation times are due to the bilayer friction rather than to the dissipation in the surrounding liquid.

### 7.5. Dynamics of a bound fluid membrane

We now turn to the dynamics of a membrane interacting with a substrate through a potential  $V(l)$  introduced in section 6.2, to which we refer for definitions. For simplicity, we first describe the membrane within the classical model as an incompressible sheet. Modifications due to the bilayer structure will become important only beyond a crossover vector  $q_1^a$ , to be determined later.

#### 7.5.1. Hydrodynamics near a substrate

The hydrodynamics of the liquid surrounding the membrane is strongly affected by the presence of the wall. Since a membrane displacement with parallel wave-vector  $\mathbf{q}$  distorts the liquid flow field along a distance  $1/q$  perpendicular to the membrane, the kinetic coefficient will deviate from its free value  $\Gamma_0(q)$  whenever  $q < 1/l_0$ , where  $l_0$  is the distance of the membrane from the wall. For optical measurements, the criterion  $q < 1/l_0$  will typically be met.

The kinetic coefficient in this geometry can be obtained from the expression for the Oseen tensor (7.14) and (7.15). The components of the total force density arising from the membrane and the wall are located at  $z = l_0$  and  $z = 0$ , respectively. After a Fourier transformation parallel to the substrate, the total force density can thus be written as

$$\mathbf{K}_{\mathbf{q},z} \equiv \delta(z - l_0) \left[ -\frac{\partial F_0^a}{\partial h_{\mathbf{q}}^*} \hat{\mathbf{z}} + K_{\mathbf{q}/\hat{\mathbf{q}}} \right] + \delta(z) [K_{\mathbf{q}z}^s \hat{\mathbf{z}} + K_{\mathbf{q}/\hat{\mathbf{q}}}^s \hat{\mathbf{q}}]. \quad (7.41)$$

The first term is the normal force exerted by bending the membrane, where  $F_0^a$  has been defined in (6.4). The latter three terms are the (as yet unknown) force exerted by the membrane parallel to the plane, and the normal and the longitudinal force exerted by the substrate. If this force density is inserted into (7.14) and (7.15), the

liquid flow field everywhere is obtained. The three unknown forces are determined through the following boundary conditions. First, both the normal and the longitudinal component of the velocity at the substrate have to vanish. Second, in the classical model, the membrane is incompressible, which implies that the in-plane divergence of the liquid flow at  $z = l_0$  vanishes, i.e.  $\nu_{qz}(l_0) = 0$ . The relationship between  $\nu_{qz}(l_0) = \partial_t h_q$  and the normal force  $-\partial F_0/\partial h_q$  can then be written in the form

$$\partial_t h_q = -\Gamma^a(q, l_0) E_0^a(q) h_q, \quad (7.42)$$

where the energy  $E_0^a(q)$  is given by (6.4).

The kinetic coefficient obeys the scaling form (Seifert 1994)

$$\Gamma^a(q, l_0) = \Gamma_0(q) G(ql_0), \quad (7.43)$$

with the free kinetic coefficient  $\Gamma_0(q)$  as defined in (7.22) and the scaling function

$$G(x) \equiv 2 \frac{\sinh^2 x - x^2}{\sinh^2 x - x^2 + \sinh x \cosh x + x} \rightarrow \begin{cases} x^3/3, & x \ll 1, \\ 1, & x \gg 1. \end{cases} \quad (7.44)$$

For  $q \gg 1/l_0$ , the asymptotic behaviour of  $\Gamma^a(q, l_0)$  deviates from its free value displaying the usual  $q^2$  behaviour for conserved quantities, the conserved quantity here being the volume of liquid between the membrane and the substrate.

### 7.5.2. Damping rate and correlation function

The  $q$  dependence of the damping rate,

$$\gamma_0^a(q) \equiv \Gamma^a(q, l_0) E_0^a(q), \quad (7.45)$$

depends on several crossover length scales arising from either the kinetic coefficient  $\Gamma^a$  or the energy  $E_0^a$ . In the low- $q$  limit, one finds (Seifert 1994)

$$\gamma_0^a(q) \approx \Omega l_0^3 q^2 / (12\eta), \quad q \ll \min[1/l_0, 1/\xi, 1/\xi_\Sigma], \quad (7.46)$$

independent of the tension and the rigidity of the membrane. With increasing  $q$ , the sequence of crossovers depends on the strength of the tension. We discuss explicitly only the case of weak tension,  $\Sigma \ll 2(\kappa\Omega)^{1/2}$ , where the energy exhibits only one crossover length scale at  $\xi$  defined in (6.5). Two cases must be distinguished, as follows.

(1) (*Monotonic damping*) For  $l_0 < \xi$ , the intermediate behaviour is given by

$$\gamma_0^a(q) \approx \kappa l_0^3 q^6 / (12\eta), \quad 1/\xi \ll q \ll 1/l_0. \quad (7.47)$$

Such a  $q^6$  behaviour was first found by Brochard and Lennon (1975) as the low- $q$  limit of the bending fluctuations of two parallel membranes used as a crude model for fluctuations of red blood cells.

(2) (*Non-monotonic damping*) For  $\xi < l_0$ , the  $q$  dependence becomes

$$\gamma_0^a(q) \approx \kappa / (4\eta\xi^4 q), \quad 1/l_0 \ll q \ll 1/\xi. \quad (7.48)$$

In this case, the damping rate *decreases* with increasing wave-vector (Seifert 1994). This unusual feature arises from the fact that the potential confines the mean-square amplitudes  $\langle h_{\mathbf{q}} h_{\mathbf{q}'}^* \rangle$  to the value  $(T\xi^4/\kappa)(2\pi)^2\delta(\mathbf{q} - \mathbf{q}')$  independently of  $q$ , while the hydrodynamic damping becomes less effective with increasing  $q$ .

Finally, for large  $q \gg \max[1/l_0, 1/\xi]$ , the damping rate of the free membrane is recovered. Illustrative examples for the various regimes and, in particular, the dynamics of the unbinding transitions are discussed elsewhere (Seifert 1994).

### 7.5.3. Effect of bilayer architecture

We now discuss the modifications which arise if the bound membrane is treated as a bilayer consisting of compressible monolayers (Kraus and Seifert 1994). In the harmonic approximation, the energy for the bound bilayer is given, in analogy to the free membrane, by

$$F^a \equiv \frac{1}{2} \int \frac{d^2 q}{(2\pi)^2} (h_{\mathbf{q}}, \rho_{\mathbf{q}}, \bar{\rho}_{\mathbf{q}}) \begin{pmatrix} \tilde{\kappa}q^4 + \Sigma q^2 + \Omega & -2kdq^2 & 0 \\ -2kdq^2 & 2k & 0 \\ 0 & 0 & 2k \end{pmatrix} \begin{pmatrix} h_{\mathbf{q}} \\ \rho_{\mathbf{q}} \\ \bar{\rho}_{\mathbf{q}} \end{pmatrix}^*. \quad (7.49)$$

No coupling between the lateral densities and the distance from the substrate is assumed here. If such a coupling arises from a more careful treatment of van der Waals interaction, it could be incorporated easily on the harmonic level.

The force density that enters the expressions (7.14) and (7.15) for the velocity field is now given by

$$\mathbf{K}_{\mathbf{q},z} \equiv \delta(z - l_0) \left[ -\frac{\partial F^a}{\partial h_{\mathbf{q}}^*} \hat{\mathbf{z}} + (K_{\mathbf{q}l}^+ + K_{\mathbf{q}l}^-) \hat{\mathbf{q}} \right] + \delta(z) [K_{\mathbf{q}z}^s \hat{\mathbf{z}} + K_{\mathbf{q}l}^s \hat{\mathbf{q}}], \quad (7.50)$$

where the tangential force at the membrane is split into two parts. While the boundary condition for the velocity field at the substrate remains the same as above, the tangential velocities at the membrane have to match with the force balance within each monolayer, which is still given by (7.28). Solving these equations leads to the relaxational dynamics of the form

$$\frac{d}{dt} \begin{pmatrix} h_{\mathbf{q}} \\ \rho_{\mathbf{q}} \\ \bar{\rho}_{\mathbf{q}} \end{pmatrix} = -\Gamma^a(q, l_0) \mathbf{E}^a(q) \begin{pmatrix} h_{\mathbf{q}} \\ \rho_{\mathbf{q}} \\ \bar{\rho}_{\mathbf{q}} \end{pmatrix}. \quad (7.51)$$

The explicit expression for the matrix of kinetic coefficients  $\Gamma^a(q, l_0)$  is quite lengthy (Kraus and Seifert 1994). In this geometry, the average density  $\bar{\rho}$  couples to both the shape and density-difference variable due to the broken symmetry between the upper and lower layer. In practice, however, the corresponding off-diagonal elements in  $\Gamma^a(q, l_0)$  are negligible and the physics can still be understood by considering only the variables  $h$  and  $\rho$ .

The detailed discussion of the dispersion relation and correlation functions given in Kraus and Seifert (1994) can be summarized as follows. The dispersion relation is made up of two modes with relaxation rates  $\gamma_1^a$  and  $\gamma_2^a$ . Their values are given by  $\gamma_1^a(q) \simeq \gamma_0^a(q)$  (as defined in (7.45)) and  $\gamma_2^a(q) \simeq (k/2b)q^2$ , except for  $q > q_1^a$ . The

crossover vector  $q_1^a$  is defined through the conditions that for all  $q > q_1^a$ , both of the following two conditions are met: (i)

$$\gamma_0^a(q) > \frac{kq^2}{2b}. \quad (7.52)$$

If this inequality holds, the height fluctuations are faster than the lateral density relaxation. Therefore, the bending rigidity  $\kappa$  in  $\gamma_0^a(q)$  gets renormalized to  $\tilde{\kappa}$ . This effect is relevant only if the height fluctuations are indeed governed by bending energy (rather than by the potential or the tension), i.e. only if (ii)

$$q > \max [1/\xi, 1/\xi_\kappa]. \quad (7.53)$$

If this inequality holds, the height can adjust to density fluctuations which renormalizes the effective compressibility  $k$  for density-difference fluctuations from  $k$  to  $k\kappa/\tilde{\kappa}$ .

In particular, these results imply that the height-height correlation function for long times behaves as

$$\langle h_{\mathbf{q}}(t)h_{\mathbf{q}'}^*(0) \rangle \approx (2\pi)^2 \delta(\mathbf{q} - \mathbf{q}') \begin{cases} \frac{T}{E_0^a(q)} \exp[-\gamma_0^a(q)t], & q \ll \max[1/\xi, 1/\xi_\kappa], \\ \frac{2Tkd^2}{\tilde{\kappa}\kappa q^4} \exp\left(-\frac{k\kappa q^2}{2b\tilde{\kappa}} t\right), & q \gg \max[1/\xi, 1/\xi_\kappa], \end{cases} \quad (7.54)$$

where the prefactor of the large  $q$  regime follows from a calculation analogous to the one displayed in (7.37) for the free case.

For practical applications, the various crossovers of the full dispersion relation may be close together, and asymptotic expressions based on a single  $q$  behaviour may be of little value for describing the data, as a representative example shows (Kraus and Seifert 1994). The full dispersion relation, however, should provide the basis for analysis of experimental measurements of the fluctuations of bound membranes. Even though at present the experimental data are not yet comprehensive enough for a detailed comparison, the potential of such measurements for a quantitative analysis of membrane interaction and dynamics is evident.

## 7.6. Pearlring instability of cylindrical vesicles

### 7.6.1. Experimental facts

Despite its only very recent discovery, the laser-induced pearlring instability of cylindrical vesicles is by now the best-studied case of a dynamical shape transformation (Bar-Ziv and Moses 1994). Initial preparation of the system yields stable, nearly straight single bilayer cylinders up to hundreds of microns long, anchored at both ends by large globules of lipid. The tubules are polydisperse, with initial radii  $R_0$  between 0.3–5 μm. Initially the system is somewhat flaccid, as seen from visible thermal undulations and the fact that the tubes are not quite straight.

Application of a laser spot localized to ~0.3 μm produces a dramatic transformation to a stationary ‘peristaltic’ figure, i.e. a cylindrical shape with radius at first varying roughly sinusoidally with distance  $z$  from the trap (see figure 7). Greater

laser power is required for larger-radius tubules, but nothing seems to depend on the length of the tube, so long as the trap is initially many radii from the ends. The shape transformation propagates outward from the laser trap, with a well-defined velocity  $v_f$  typically about  $30 \mu\text{m s}^{-1}$ . Remarkably, after a very short illumination the shape transformation continues to propagate after the laser is shut off, leading to a uniform, small-amplitude peristaltic shape. Longer excitation leads to a pearly state.

Once formed, the peristaltic shape has a well-defined initial wavelength which is uniform over many microns. Whatever the initial radius  $R_0$ , this wavelength is found to be  $\lambda = 2\pi R_0/k_0$ , where the dimensionless initial wave number  $k_0$  is always in the range 0.64–1.0, and typically about 0.8. As the modulation grows more pronounced,  $k$  grows from  $k_0$  to become slightly greater than 1 and deviations from a simple sinusoidal profile become pronounced. The modulated state is tense: visible thermal fluctuations are suppressed and the tube draws itself straighter than initially.

### 7.6.2. Theoretical modelling

The theoretical modelling (Bar-Ziv and Moses 1994, Nelson *et al.* 1995, Goldstein *et al.* 1996, Granek and Olami 1995) exploits the phenomenological resemblance with the classical Plateau-Rayleigh instability of cylindrical fluid jets subject to surface tension. For a volume-preserving deformation of a cylinder under tension, the area decreases for any axisymmetric deformation with a wave-number  $k_0 < 1$ . Therefore, a cylindrical shape under tension is unstable. In the presence of bending rigidity  $\kappa$ , one needs a finite tension  $\Sigma \geq 3\kappa/2R_0^2$  to initiate this static instability (Nelson *et al.* 1995).

The laser indeed creates a local lateral tension of the order of  $10^{-3} \text{ erg cm}^{-2}$  by sucking lipid into the trap (Nelson *et al.* 1995, Goldstein *et al.* 1996). This tension spreads rapidly along the cylinder since the membrane is nearly incompressible. After this very brief initial period the cylinder is unstable towards all deformations with a wavenumber smaller than 1 just as in Rayleigh's case. The wavelength selection, however, depends crucially on the dynamics and, in particular, the boundary conditions at the cylinder. In the pearly instability, a material object, the bilayer membrane separates the interior from the exterior fluid. Solving the corresponding hydrodynamical equations in the overdamped case along the lines discussed above for the planar geometry, one finds a fastest growing mode of wave-vector  $k_0 = 0.65$  (Nelson *et al.* 1995). Even though this value depends somewhat on the bending rigidity and the bilayer dynamics, it is mostly determined by the balance between the tension and the dissipation in the interior water for realistic parameters. Since the experiment shows that the instability propagates from the centre, the fastest growing mode is not the best candidate for the actual pattern.

The propagating character of the instability is captured (Goldstein *et al.* 1996) by using the concept of marginal stability (Dee and Langer 1983, van Saarloos 1988). This criterion, which applies to many propagating instabilities, is a theory of how an unstable state (here the plain cylinder after spread of the tension) starting from a localized excitation (here the laser spot) decays into a new stable minimum (here the pearly state) via front propagation. Since the marginal stability criterion only requires knowledge of the linearized dynamics around the unstable state, it can be worked out completely for the pearly instability. In fact, it leads to a much better value for the wave-number of the pattern of  $k_0 \simeq 0.8$  in presumably somewhat fortuitous agreement with experiment. A general shortcoming of the marginal

stability criterion is that it cannot prove front propagation but rather assumes it. However, a numerical solution of the full nonlinear elastic energy using a lubrication approximation for the hydrodynamics also shows front propagation with roughly the same values as the marginal stability criterion (Goldstein *et al.* 1996). The late-stage dynamics where the pearls move along the tether is not yet understood. It could be caused by lateral gradients of tension.

A different type of a dynamic instability of cylinders caused by strong van der Waals attraction has been suggested (Bruinsma 1991) to explain the sometimes observed pearlizing of aspirated vesicles after thermal expansion (Evans and Rawicz 1990).

## 8. More complex membranes

### 8.1. Mixed and inhomogeneous membranes

Single-component membranes have been the topic of the previous sections. The lipid bilayer of biomembranes, however, is composed of different types of molecules which may differ in their head groups, in the length of their hydrocarbon chains, or in the number of unsaturated bonds within these chains. In such a multi-component system, the composition can become laterally inhomogeneous within each monolayer and can be different across the two monolayers. As a result, an inhomogeneous spontaneous curvature is created which leads to a coupling between the composition and the shape (Gruler 1975, Gebhardt *et al.* 1977, Markin 1981, Leibler 1986, Leibler and Andelman 1987). Moreover, there are energies associated with composition variables such as the entropy of mixing and the cost of an inhomogeneous composition profile.

Quite generally, one can distinguish two cases for the phase behaviour of such a membrane: (i) a homogeneous one-phase region at high temperature, and (ii) a two-phase coexistence region at lower temperatures for a certain range of compositions.

Experimental investigations of the phase diagram have shown that a two-component membrane in the fluid state often exhibits a homogeneous phase. By decreasing the temperature, before reaching a critical point, the gel state intervenes which then coexists with a homogeneous fluid phase. Genuine fluid-fluid coexistence, however, has been found for a few examples. An especially important one is provided by mixtures of phospholipids and cholesterol, as has been established quite recently (Needham *et al.* 1988, Vist and Davis 1990, Bloom *et al.* 1991). Fluid-fluid coexistence also occurs in the binary mixture of DEPC and DPPE (Wu and McConnell 1975) and in mixtures with partially unsaturated alkyl chains (Bloom 1992).

#### 8.1.1. Curvature-induced phase separation

In the one-phase region, the ground state in the absence of a spontaneous curvature is a flat and laterally homogeneous membrane. However, any inhomogeneity in the composition, either laterally within a monolayer or between the two monolayers, induces a local spontaneous curvature if the two lipid species have a different molecular geometry. For an almost planar membrane, this leads to a coupling between bending fluctuations and composition fluctuations which decreases the bending rigidity (Leibler 1986, Leibler and Andelman 1987). Within the complementary 'hat' model, the reduced rigidity of a mixed membrane is attributed to local curvature fluctuations of individual molecules, lateral diffusion of the

different species and an attractive interaction between unequal molecules across the bilayer (Helfrich and Kozlov 1994).

For a non-spherical vesicle, the coupling between shape and composition causes curvature-induced lateral phase segregation (Seifert 1993). Such a phase segregation can occur if for an initially spherical vesicle a temperature increase leads to deviations from the spherical shape and, thus, to a position-dependent curvature that induces a position-dependent composition. For a quantitative description, the composition (area fractions) of lipid A in the individual monolayers  $x_A^i (= 1 - x_B^i)$  ( $i = \text{in}, \text{out}$ ) and deviations,  $\delta x_A^i(s_1, s_2) \equiv x_A^i(s_1, s_2) - \bar{x}_A$ , from the mean value  $\bar{x}_A$  are introduced. If the local deviation is different in the two monolayers, a local spontaneous curvature is induced according to

$$C_0(s_1, s_2) = \lambda[\delta x_A^{\text{out}}(s_1, s_2) - \delta x_A^{\text{in}}(s_1, s_2)] + \bar{C}_0 \equiv \lambda\phi(s_1, s_2) + \bar{C}_0, \quad (8.1)$$

where the phenomenological coupling constant  $\lambda$  has the dimensions of an inverse length (Leibler 1986). A systematic spontaneous curvature  $\bar{C}_0$  arises if the mean compositions  $\bar{x}_A^i$  are different in the two monolayers, as applies to the spontaneous formation of small vesicles in mixtures of oppositely charged surfactants where phase separation occurs across the membrane (Kaler *et al.* 1989, Safran *et al.* 1990, 1991, Kaler *et al.* 1992). A different cause of spontaneous vesiculation can be the large negative contribution of the electric double layer to the Gaussian bending rigidity of symmetrically charged membranes (Winterhalter and Helfrich 1992).

The bending energy  $F_1$  of the two-component vesicle is then chosen as a generalization of the bending energy of a single-component vesicle, as given by (2.50). This leads to (Seifert 1993)

$$F_1 = \kappa \left\{ \oint dA \frac{1}{2} [(2H(s_1, s_2) - C_0(\phi(s_1, s_2))]^2 + \frac{\alpha\pi}{8Ad^2} (\Delta A - \Delta A_0)^2 \right\}. \quad (8.2)$$

For simplicity, it is assumed that neither the bending rigidities  $\kappa$  and  $\alpha\kappa$  nor the area of the vesicle  $A$ , and area difference  $\Delta A_0$  depend on the composition.

Since the membrane does not show genuine phase separation, there is a free energy associated with the deviation of the composition from its mean value. For small deviations, this energy can be written in the form

$$F_2 = \frac{\kappa}{2} \epsilon \oint dA [\phi^2 + (\xi_c \nabla \phi)^2]. \quad (8.3)$$

Here,  $\xi_c$  is the correlation length for composition fluctuations,  $\nabla$  is the covariant gradient operator, and  $\epsilon$  is a molecular energy divided by the bending rigidity.

Since the typical length scale for shape variations of large vesicles is in the micrometre range, while the typical correlation length  $\xi_c$  will be of the order of nanometres, the gradient term in  $F_2$  will be, in general, much smaller than the  $\phi^2$  term, and thus can be ignored. If the exchange of molecules between the two layers is forbidden, the total energy

$$F \equiv F_1 + F_2 \quad (8.4)$$

has to be minimized under the constraint  $\oint dA \phi = 0$ . The composition profile  $\phi(s_1, s_2)$  then becomes

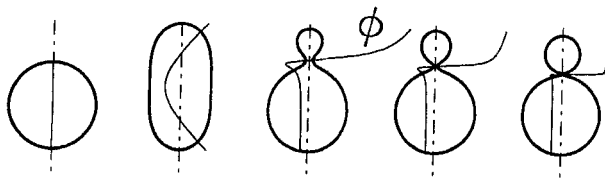


Figure 32. Curvature-induced lateral phase segregation. The spherical vesicle changes its shape as the reduced volume  $v$  decreases due to an increase in temperature. The light curves show the composition  $\phi$ . The reduced volume is given by  $v = 1.0, 0.89, 0.89, 0.86$  and  $0.82$  from left to right. At  $v = 0.89$ , the symmetric and the asymmetric shapes have the same energy, indicating a discontinuous budding transition. The vesiculation line is reached with the last shape (Seifert 1993).

$$\phi(s_1, s_2) = \frac{2\lambda}{\lambda^2 + \epsilon} \left[ H(s_1, s_2) - \frac{\Delta A}{4dA} \right], \quad (8.5)$$

which shows that the local composition follows the deviation of the mean curvature  $H(s_1, s_2)$  from its average value  $\Delta A/(4dA)$ . After inserting (8.5) into  $F$ , the total energy can be cast in the standard form of the bending energy of a single-component vesicle in the ADE model (2.50) in which the bending rigidity, the parameter  $\alpha$ , and the equilibrium area difference  $\Delta A_0$  have been renormalized (Seifert 1993).

Once this mapping has been obtained, both the knowledge of the phase diagram of the area-difference-elasticity model and shape calculations within this model can be used to obtain results for the two-component system. As an illustrative example, consider the thermal evolution of an initially spherical vesicle (with a homogeneous composition profile  $\phi(s) = 0$ ) with increasing temperature as shown in figure 32. It is assumed that the thermal trajectory is still given by (3.26) with  $r = 1$ . With increasing temperature, the reduced volume decreases and the shape becomes more prolate. The inhomogeneous curvature then induces a non-trivial composition profile along the contour. In the outer monolayer, the A molecules are enriched at the poles (if their enhancement in the outer layer leads to a positive spontaneous curvature, i.e. if  $\lambda > 0$ ) while the B lipids are enriched along the equatorial region of the vesicle. For smaller  $v$ , the up/down asymmetric shapes have lower energy leading to a discontinuous budding transition. These shapes finally end up at the vesiculation point. In the vesiculated state, the composition within each sphere becomes homogeneous again with all the variation of the composition occurring in the neck. Thus, the shape change, i.e. in this case budding and vesiculation, leads to phase segregation. Moreover, the formation of smaller buds is more favourable in the two-component system than in the pure system under the same conditions (Seifert 1993).

Even though a few experiments have been performed on shape transformations of multi-component vesicles (Farge and Devaux 1992), the interaction between local composition and the shape transformation has not yet been systematically studied. For such a comparison between theory and experiment, one should, for example, analyse the composition of the bud and compare it with the composition of the mother vesicle. The experimental observation that budding can be followed by fission in a multicomponent membrane (Döbereiner *et al.* 1993) may help to achieve this challenging task.

In the vicinity of the demixing point, the correlation length  $\xi_c$  for compositional fluctuations increases and the gradient term in (8.3) becomes relevant. In this case,

the mapping from the two-component system to an effective one-component system is no longer possible and one rather has to solve more complicated shape equations. Andelman and co-workers have investigated this regime in detail for 2D and 3D vesicles (Taniguchi *et al.* 1994). They found a renormalization of the demixing temperature and below that temperature various non-trivial shapes. Depending on the pressure difference, one can reach shapes characterized by higher spherical harmonics ( $l \geq 3$ ), which were unstable in the homogeneous case.

### 8.1.2. Domain-induced budding

In the two-phase region, domains of one phase in the surrounding matrix of the other phase are formed. The edges of these domains are characterized by an edge or line tension. Since the length of the domain boundary decreases if the domain buds, the competition between this edge tension and the curvature energy leads to domain-induced budding as soon as the domain reaches a critical size (Lipowsky 1992, 1993, Jülicher and Lipowsky 1993).

If a membrane that is initially prepared in a homogeneous state within the one-phase region is quenched deep into the  $(\alpha\beta)$  spinodal decomposition two-phase region, phase separation within the membrane is initiated. In such a situation, many small domains will be formed initially. The edge of an intramembrane domain has an energy which is proportional to the edge length. Therefore, the domain has a tendency to attain a circular shape in order to minimize its edge energy.

A flat domain will form a circular disk in order to attain a state with minimal edge length. For a circular domain with radius  $L$ , the edge energy  $F_e$ , is given by

$$F_e \equiv 2\pi L \Sigma_e. \quad (8.6)$$

The line tension,  $\Sigma_e$ , is equal to the edge energy per unit length. As far as the edge energy is concerned, a flat circular disk does not represent the state of lowest energy since the length of the edge can be further reduced if the domain forms a bud. This budding process is governed by the competition between the bending rigidity  $\kappa$  of the domain and the line tension  $\Sigma_e$  of the domain edge. This competition leads to the characteristic invagination length  $\xi \equiv \kappa / \Sigma_e$  (Lipowsky 1992). For phospholipid–cholesterol mixtures, the bending rigidity  $\kappa$  was experimentally estimated to have the relatively large value  $\kappa \simeq 4 \times 10^{-19} \text{ J}$  (Duwe *et al.* 1990). The line tension, on the other hand, seems to have the relatively small value  $\Sigma_e \simeq 10^{-18} \text{ J } \mu\text{m}^{-1}$  (Benvegnù and McConnell 1992). This implies the invagination length  $\xi \simeq 400 \text{ nm}$ .

The competition between the edge and bending energies can be understood in the framework of a relatively simple model in which one assumes that the membrane matrix is flat and that the membrane domain forms a spherical cap with radius  $R$  (Lipowsky 1993). If the domain has surface area  $A = \pi L^2$  and spontaneous curvature  $C_0$ , its total energy  $F = F_{SC} + F_{\Sigma_e}$  has the form

$$F/2\pi\kappa = (L/R - LC_0/2)^2 + (L/\xi)[1 - (L/2R)^2]^{1/2}. \quad (8.7)$$

For  $C_0 = 0$ , such a model has also been studied in order to discuss the size of vesicles generated by sonification and to study the closure of open fluid membranes (Helfrich 1974b, Fromherz 1983, Boal and Rao 1992b). The energy  $F$  has several minima and maxima as a function of  $L/R$ .

For small  $L$ , the domain forms an incomplete bud corresponding to the minimum of  $F$  at small  $L/R$  values. As  $L$  grows, the edge of the domain becomes longer, and the energy of the incomplete bud is increased. At a certain critical size,  $L = L^*$ , the incomplete bud has the same energy as the complete bud corresponding to a complete sphere but both states are separated by an energy barrier. For the parameter values considered here, the energy barrier is typically large compared to the thermal energy  $\simeq T$ . In this case, the domain continues to grow in the incomplete bud state up to the limiting size  $L = L^0$  with

$$L^0 = 8\xi/[1 + (2\xi|C_0|)^{2/3}]^{3/2}, \quad (8.8)$$

at which this state becomes unstable (Lipowsky 1992).

The same type of budding instability is found from a systematic minimization procedure for closed vesicles composed of two types of domains,  $\alpha$  and  $\beta$  (Jülicher and Lipowsky 1993). In this paper, the non-trivial role of the Gaussian bending rigidity for vesicles with domains has also been emphasized. Shapes of 2D and 3D vesicles consisting of several domains with different spontaneous curvature have also been investigated systematically as a function of the pressure difference (Andelman *et al.* 1992, Kawakatsu *et al.* 1993).

### 8.1.3. Membranes with inclusions

Another type of inhomogeneity arises from inclusions of large particles such as proteins in a membrane. Such an object represents a defect in a fluid membrane. Depending on the boundary conditions between defect and membrane, the membrane-mediated interaction between two inclusions a distance  $R$  apart can be long-range repulsive or attractive. Various models can be studied (Goulian *et al.* 1993). For cone-line defects that impose a tilt on the surrounding membrane, a repulsive interaction  $\sim 1/R^4$  was found by minimizing overall curvature energy. If the two domain-like defects have finite but different bending rigidity, finite temperature leads to a long-range interaction  $\sim T/R^4$  which can be attractive or repulsive depending on the difference in bending rigidity. Finally, for flat domains a ‘Casimir’-type attractive interaction  $\sim T/R^4$  arises from the bending fluctuation ‘between’ the inclusions. A similar behaviour has been studied for membrane stacks (Palmer *et al.* 1994).

Defects cause local thickness changes of the bilayer according to the mattress model of mixed membranes (Bloom *et al.* 1991). Since a continuum model predicts that the membrane thickness profile in the vicinity of such a defect decays non-monotonically, the membrane-mediated interaction between these inclusions can have a minimum at finite separation  $R$  (Dan *et al.* 1994). Active inclusions such as proteins which pump ions modify the spectrum of long-wavelength curvature fluctuations from  $\sim q^4$  to  $\sim q^5$  under suitable conditions (Prost and Bruinsma 1996).

## 8.2. Fluid membranes with internal degrees of freedom

While homogeneous fluid membranes are characterized by their shape only, interesting ramifications arise for membranes with internal degrees of freedom. A paradigmatic case for an internal degree of freedom has been discussed above since for lipid mixtures the composition is a scalar field living on the membrane. We have seen how an internal energy contribution such as a line tension can be relieved by

budding of a domain, i.e. by changing the (external) geometry of the membrane. Similar phenomena occur if the internal degree of freedom is associated not with composition in a multi-component membrane but rather with orientation of molecules in a single-component membrane. Examples for such a degree of freedom are tilt of the lipid molecules as in smectic C order (de Gennes and Prost 1993), the bond orientational order of a hexatic membrane (Nelson and Peliti 1987, David *et al.* 1987), chirality of the constituent molecules (de Gennes and Prost 1993; Helfrich and Prost 1988), or flexo- and ferro-electric membranes (Peliti and Prost 1989).

The coupling between an internal degree of freedom to the curvature of the membrane can lead to various effects. First, it may even destroy the planar ground state of the membrane. For tilt, modulated phases such as different ripple phases or even square phases (Lubensky and Mackintosh 1993, Chen *et al.* 1995) can arise from such a coupling if it is strong enough. Likewise, chirality, which couples to the shape via tilt, can produce helical ribbons (Helfrich and Prost 1988, Nelson and Powers 1992, 1993, Selinger and Schnur 1993).

Second, for weak coupling the flat membrane as ground state may persist, but its long-wavelength spectrum of excitations, i.e. the effective elasticity, can be altered. For a hexatic membrane, the effective bending rigidity increases logarithmically with the length scale (Nelson and Peliti 1987). A renormalization group study (Powers and Nelson 1995) has shown that tilt order in the flat phase leads to the same elastic behaviour as hexatic order, as has been previously proposed for different reasons (Peliti and Prost 1989).

For closed vesicles, orientational order can lead to new phenomena not present for planar membranes. Tilt order on a spherical vesicle necessarily generates defects at the poles. This causes a transformation from a sphere towards a prolate shape (MacKintosh and Lubensky 1991). This work has been extended (Park *et al.* 1992) to cover more generally  $n$ -atic order on a membrane. Below the ordering transition, the shapes have polyhedral form with  $2n$  vertices. Since tangent order expels Gaussian curvature, cylindrical tubes can be more favourable than vesicles of spherical topology (Lubensky and Prost 1992). On a toroidal surface,  $n$ -atic order leads to a large variety of patterns and associated shape transformations (Evans 1995b).

### 8.3. Polymerized membranes and vesicles

#### 8.3.1. Fluctuating almost flat polymerized membranes

Polymerized or solid membranes have fixed internal connectivity in contrast to the fluid membranes discussed so far. These membranes can sustain shear. The in-plane displacements or ‘phonons’ of such membranes couple to the bending modes (Landau and Lifshitz 1989). For a flat membrane, thermal undulations lead via this nonlinear coupling to an effective bending rigidity.

$$\kappa(q) = (YT)^{1-\zeta} \kappa_0^{2\zeta-1} q^{2(\zeta-1)} \quad (8.9)$$

that depends on the scale, i.e. on the wave-number  $q$  (Nelson and Peliti 1987, Nelson 1988, Lipowsky and Girardet 1990). Here,  $Y$  is the 2D Young’s modulus,  $\kappa_0$  is the ‘bare’ bending rigidity, and  $\zeta$  is the roughness exponent. Both the value of this exponent and the existence of a genuine crumpled phase have initially been a matter of many Monte Carlo studies using different models. Meanwhile, the consensus seems to be that self-avoidance alone is sufficient to prevent a crumpling transition

even for zero bending rigidity (see, for example, Kroll and Gompper (1993)). The absence of a crumpling transition is in agreement with a freeze fracture electron microscopy and light scattering study on thin graphitic oxide sheets for which a crumpled phase could not be found under any conditions (Spector *et al.* 1994). The value of the exponent seems to settle towards  $\zeta \simeq 0.6$ , consistent with the prediction of an analytical approach (Le Doussal and Radzhovsky 1992). Such a numerical value would imply that the effective shear modulus vanishes on long scales (Aronovitz and Lubensky 1988). The dynamics of two parallel polymerized membranes have been investigated as a model for a red blood cell geometry (Frey and Nelson 1991).

### 8.3.2. Fluctuating polymerized vesicles

For a curved polymerized membrane, the coupling between phonons and bending becomes linear. A spherical shell cannot be bent without being stretched. As studied for a cylinder (Komura and Lipowsky 1992) and for a spherical vesicle (Zhang *et al.* 1993), this linear coupling implies that there is a crossover length  $L^* \simeq (R^2 \kappa / Y)^{1/4}$  for thermal fluctuations. While fluctuations below this crossover length behave like those of a flat membrane, the mean-square amplitudes of bending modes with a large wavelength are essentially independent of  $q$ .

### 8.3.3. Stiff polymerized vesicles

The low-temperature behaviour of polymerized vesicles depends crucially on the fact that a closed polymerized membrane of spherical topology necessarily has defects. In a planar membrane such defects lead to buckling (Seung and Nelson 1988). For a triangular network, one needs 12 fivefold disclinations to form a closed shell. By adding planar faces to an icosahedron, which is the smallest triangulated shape, larger vesicles can be formed.

For small vesicles, the total elastic energy of this shell arises mostly from the energy of the disclinations and scales as  $\sim \ln N$ , where  $N$  is the number of vertices (Tersoff 1992). For larger vesicles, the vesicle can lower its elastic energy by slightly bending the edges of the polyhedral shape. A scaling argument predicted the radius of curvature at the edges to scale as  $N^{1/3}$ , whereas the total energy scales as  $N^{1/6}$  (Witten and Li 1983). This behaviour was indeed verified by numerically minimizing the elastic energy for very large vesicles (Zhang *et al.* 1995). The numerical minimization revealed also that the mean curvature is negative over large portions of the icosahedron.

These polymerized vesicles have applications not only to vesicle shapes in the gel phase but also to fullerene buckyballs. They may also be relevant to clathrin-coated pits in golgi vesicle budding.

## 8.4. Red blood cell membrane

With the red blood cell, biology provides a main motivation for the study of polymerized membranes. Apart from the fluid lipid bilayer, the plasma membrane of a red blood cell contains a network of spectrin tetramers linked together at junctional complexes which forms a quasi-hexagonal structure attached to the bilayer by integral membrane proteins (Alberts *et al.* 1989). The spectrin network can be isolated by dissolving the lipid with detergents. It then no longer exhibits the typical biconcave shape of the red blood cell but rather becomes nearly spherical. Its morphological and elastic properties can be studied if the skeletons are suspended

with optical tweezers in a flow chamber (Svoboda *et al.* 1992). Likewise, X-ray diffraction as well as light scattering (Schmidt *et al.* 1993) probe the structural properties of this network.

For the compound red blood cell membrane, the presence of the network poses a conceptual problem for the calculation of shapes since it is not yet clear to what extent the network contributes to the stability of the shape. In fact, we have seen that even for lipid vesicles a discocyte shape minimizes the curvature energy in an appropriate range of the reduced volume. Thus, in the absence of external forces, the shape of the red blood cell could be controlled primarily by the bending elasticity of the bilayer together with the osmotic conditions, while the cytoskeleton is used to recover this shape after deformations of the cell shape. On the other hand, it is known that dissolving the network from the bilayer results in spontaneous budding of small vesicles. Thus, it seems that the network is relevant in stabilizing the red blood cell lipid membrane with its specific composition (Steck 1989).

Evidence for a presumably subtle interplay between network and bilayer also arises from measurements of the elastic properties of the red blood cell membrane and, in particular, from its shear modulus, which seems to be strongly scale dependent. On large scales, deformation in the micro-pipette (Waugh and Evans 1979) as well as deformation induced by an electric field (Engelhardt and Sackmann 1988) yield a shear modulus which is one order of magnitude larger than the one obtained from the analysis of the thickness fluctuations by flicker spectroscopy, which probes smaller scales (Strey *et al.* 1995). The latter paper gives a careful discussion of the various factors which may be at the origin of this discrepancy.

A comprehensive theoretical model for the red blood cell membrane has not yet emerged. Steps in such a direction are provided by a continuum theory in which the network is modelled as an ionic gel (Stokke *et al.* 1986a, b), as well as by recent computer simulations (Boal *et al.* 1992, Boal 1994). The analysis of these models shows a sensitive dependence of the shear modulus on the properties of the spectrin tethers. For an understanding of the red blood cell membrane, concepts from polymer physics and membrane physics thus have to merge.

These few remarks on the red blood cell, the quest for whose understanding marks one of the starting points of the research on vesicles, demonstrate the continuing inspiration biology brings to physics. Based on the experience acquired in comprehending vesicle configurations as described in this article, the study of these more complicated systems is anticipated to reveal more fascinating surprises in the near future.

#### Acknowledgments

I am indebted to R. Lipowsky for introducing me to this field, for an enjoyable collaboration, and for generous support at the University in Munich, at the IFF in Jülich, and at the MPI in Teltow. I am most grateful to M. Wortis both for support at Simon Fraser University, Vancouver, and for a pleasant collaboration. E. Sackmann organized the ‘Sonderforschungsbereich’ in Munich without which this work would never have been nucleated. I am indebted to him for support, for many inspiring discussions, and for a fruitful collaboration. K. Berndl, M. Jarić, F. Jülicher, M. Kraus, L. Miao, and W. Wintz contributed substantially via their theses to various parts of the present work. I am grateful to all of them as well as to S. Langer and P. Nelson for an enjoyable collaboration. Discussions and

collaboration with the experimentalists H.-G. Döbereiner, W. Fenzl, J. Käs, X. Michalet and J. Rädler have been most stimulating. I am grateful to E. Evans and W. Helfrich for always generously sharing their insights with me. I benefited from correspondence, discussions and collaboration with many more colleagues too numerous to list here. I thank C. Goh, S. Langer and A. Ulrich for critically reading through parts of an earlier version of this paper.

This paper is based on a habilitation thesis submitted in October 1994 to, and accepted in December 1995 by, the University of Munich. I would like to express my sincere thanks to H. Wagner for guidance and support over many years and during this process.

#### Appendix A. List of recurrent symbols

Symbol	Meaning	Defined in equation
$A$	area of the vesicle	2.49
$\Delta A$	area difference between the two monolayers	2.46
$\Delta A_0$	optimal area difference between the two monolayers	2.47
$b$	friction coefficient for monolayer slipping	7.28
$c_0$	reduced spontaneous curvature	2.56
$C_0$	spontaneous curvature	2.54
$d$	distance between bilayer mid-plane and monolayer neutral surface	after 2.19
$d_i^{(1,2,3)}$	linear term in an expansion of the geometrical quantities	4.5–4.7
$D_{ij}^{1,2,3}$	matrix elements of the second variation of the geometrical quantities	4.5–4.7
$E$	energy matrix	2.29
$E_0$	energy of a bending mode	2.14
$E_0^a$	energy of a bending mode of a bound bilayer	6.4
$f$	energy density of a bilayer membrane	2.23
$f_0$	energy density of a membrane in the classical model	2.10
$f_1^\pm$	elastic energy density of the monolayers	2.19
$F$	energy of a bilayer membrane	2.28
$F_0$	energy of a membrane in the classical model	2.13
$F_0^a$	energy of a bound bilayer in harmonic approximation	6.4
$g_i$	linear term in an expansion of the bending energy	4.4
$G$	dimensionless bending energy	2.51
$G_{ij}$	matrix of the second variation of the bending energy	4.4
$H$	mean curvature	2.1
$k^m$	elastic compression modulus of the monolayer	2.19
$K$	Gaussian curvature	2.2
$K$	external force acting on the liquid	7.1

## Appendix A—(Continued)

Symbol	Meaning	Defined in equation
$l_0$	distance from the wall for which the adhesion potential is minimal	6.28
$m$	reduced total mean curvature	2.56
$m_0$	reduced optimal area difference	2.56
$M$	total mean curvature	2.45
$\mathbf{n}$	normal vector	2.6
$N^\pm$	number of lipid molecules in the two layers	2.40
$P$	Lagrange multiplier for volume	3.1
$Q$	Lagrange multiplier for mean curvature	3.1
$R_g$	gas constant	2.37
$R_0$	equivalent sphere radius	2.49
$R_1^*$	inverse contact curvature	6.16
$S_{ij}$	elements of the stability matrix	4.10
$u_{l,m}$	expansion coefficients of fluctuating quasispherical shape	4.19
$v$	reduced volume	3.11
$\mathbf{v}$	velocity field of the surrounding liquid	7.1
$V^0$	value of the adhesion potential in its minimum	6.28
$V_f^0$	value of the adhesion potential for which a free vesicle becomes deformed	6.29
$V_u^0$	value of the adhesion potential for which thermally activated unbinding sets in	6.33
$w$	scaled contact potential for adhesion	6.17
$W$	(i) energy of a vesicle in the area-difference elasticity model (ii) contact potential for adhesion (in section 6)	2.50 6.15
$W_a$	value of contact potential at adhesion transition	6.18
$\alpha$	material parameter of the area-difference elasticity	2.52
$\gamma_0$	damping rate of a bending mode in the classical model	7.24
$\gamma_0^a$	damping rate of a bending mode of a bound membrane	7.45
$\gamma_{1,2}$	damping rates of coupled bilayer modes	7.34
$\Gamma^a$	kinetic coefficient of a bound membrane	7.43
$\Gamma_0$	kinetic coefficient in the classical model	7.22
$\Delta$	dimensionless excess area	4.18
$\kappa$	bilayer bending rigidity	2.10
$\tilde{\kappa}$	renormalized bilayer bending rigidity	2.30
$\kappa^m$	bending rigidity of a monolayer	2.34
$\kappa_G$	Gaussian bending rigidity of the bilayer	2.10
$\xi, \xi_\Sigma, \xi_\kappa$	crossover length scales for a bound bilayer	6.5 and 6.6
$\rho$	reduced density difference	2.24
$\bar{\rho}$	reduced average density deviation	2.25
$\rho^\pm$	reduced density difference deviations	2.22

Symbol	Meaning	Defined in equation
$\bar{\sigma}$	dimensionless effective tension	4.31
$\Sigma$	in sections 2–5: Lagrange multiplier for area in sections 6 and 7: external tension	3.1 6.1
$\bar{\Sigma}$	in section 6.5: Lagrange multiplier for area of a bound vesicle	before 6.34
$\tau$	ratio between reduced temperature and excess area	4.27
$\phi_0$	equilibrium number density of lipids in the monolayer	2.19
$\phi^\pm$	number densities of lipids in the monolayer	2.19
$\phi_{\text{proj}}^\pm$	number densities of lipids in the monolayer projected onto bilayer midplane	2.19
$\Phi$	variational free energy functional	3.1
$\Omega$	curvature of adhesion potential	6.2

## Appendix B. Determination of the bending rigidity

Great effort has been devoted in recent years to determining the bending rigidity  $\kappa$ . Conceptually, two different approaches can be distinguished. In the mechanical approach, the response of the membrane to an applied force is measured, from which the bending rigidity is deduced. The extreme softness of these systems is exploited by the second type of method where the bending rigidity is derived from the thermally excited membrane fluctuations.

One example of the mechanical approach (Evans 1983, Evans and Needham 1987) is provided by studies of tether formation from giant vesicles which are aspirated with a micro-pipette (Bo and Waugh 1989). The tether is pulled out by the gravitational force on a small glass bead which adheres to the vesicle's surface. The length of the tether is determined by the balance of the suction pressure, the gravitational force and bending energies. It has been realized only recently that, with this method, the bending rigidity  $\kappa$  and the non-local bending rigidity,  $\bar{\kappa} = \alpha\kappa$ , can be measured simultaneously (Waugh *et al.* 1992).

In the flickering experiments, the bending rigidity is derived from mean-square amplitudes of thermally excited membrane fluctuations using phase contrast microscopy combined with fast image processing. This technique has been used with tubular vesicles (Servuss *et al.* 1976, Schneider *et al.* 1984a), quasi-spherical vesicles (Schneider *et al.* 1984b, Engelhardt *et al.* 1985, Bivas *et al.* 1987, Faucon *et al.* 1989, Duwe *et al.* 1990, Meleard *et al.* 1992, Haeckl *et al.* 1995), shape fluctuations of almost planar membrane segments (Mutz and Helfrich 1990), and fluctuations of weakly bound vesicles (Zilker *et al.* 1987, Rädler *et al.* 1995).

A third class of experiments combines the mechanical with the entropic approach. Since aspiration of the vesicle in the micro-pipette changes the area available for fluctuations (Helfrich and Servuss 1984), the strength of the fluctuation can be controlled mechanically. From the relation between the area stored in the fluctuations and the suction pressure, which is related to the effective entropic tension, the bending rigidity can be deduced (Evans and Rawicz 1990). The same idea has also been used in a very different set-up where quasi-spherical vesicles are elongated in an ac electric field (Kummrow and Helfrich 1991). Again the bending

rigidity is derived from the relation between the area stored in the fluctuations and the applied field which controls the tension.

The values obtained by these techniques differ quite a bit among the different lipids. The typical range is  $\kappa \approx 2 \times 10^{-13}$ – $10^{-12}$  erg. Even for the same lipid, the bending rigidity differs by a factor of 2 using different methods. Sometimes, the same technique applied by different research groups yields significantly different values. In a recent attempt to resolve these discrepancies, the quasi-spherical fluctuations and the elongation in the electric field were analysed at the same vesicle to determine the bending rigidity (Niggemann *et al.* 1995). Depending on whether or not the glue sealing the cell was in contact with the vesicle, the two methods agreed or differed about a factor of 2–3. Helfrich proposes that a possible sensitivity to polymeric contamination from the sealing glue indicates that fluid membranes are rough on a suboptical scale (Helfrich 1989, 1995, Helfrich and Klösgen 1992). A surprisingly strong decrease of the bending rigidity with temperature was also found in Niggemann *et al.* (1995). For DOPC, for example,  $\kappa$  decreases by more than a factor of three from  $T = 13^\circ\text{C}$  to  $T = 34^\circ\text{C}$ .

The bending rigidity for mixtures is particularly interesting given the fact that biological membranes always involve mixtures. The addition of cholesterol to fluid bilayers increases the bending rigidity (as well as the area compressibility) significantly (Evans and Needham 1987, Duwe *et al.* 1990). However, the non-local bending rigidity seems not to change with the addition of cholesterol (Song and Waugh 1993). This may be related to the fact that cholesterol can flip between the monolayers quite rapidly.

A significant decrease in the apparent bending rigidity of an order of magnitude follows from the addition of a few (2–5) mol. % of a short bipolar lipid (bola lipid) or small peptides (e.g. valinomycin) (Duwe *et al.* 1990, Haeckl *et al.* 1995). Since the apparent bending rigidity then becomes comparable to the thermal energy  $T$ , these vesicles exhibit very strong shape fluctuations. Entropic terms then become relevant for the description of typical conformations. One must note, however, that bola lipid is much more soluble in water and thus will go in and out of the bilayer more rapidly.

### References

- ALBERTS, B., BRAY, D., LEWIS, J., RAFF, M., ROBERTS, K., and WATSON, J. D., 1989, *Molecular Biology of the Cell*, Second edn (New York: Garland).
- ANDELMAN, D., KAWAKATSU, T., and KAWASAKI, K., 1992, Equilibrium shape of two-component unilamellar membranes and vesicles, *Europhys. Lett.*, **19**, 57–62.
- ARONOVITZ, J. A., and LUBENSKY, T. C., 1988, Fluctuations of solid membranes, *Phys. Rev. Lett.*, **60**, 2634–2637.
- BACKER, J. M., and DAWIDOWICZ, E. A., 1981, Transmembrane movement of cholesterol in small unilamellar vesicles detected by cholesterol oxidase, *J. biol. Chem.*, **256**, 586–588.
- BAILEY, S. M., CHIRUVOLU, S., ISRAELACHVILI, J. N., and ZASADZINSKI, J. A. N., 1990, Measurements of forces involved in vesicle adhesion using freeze-fracture electron microscopy, *Langmuir*, **6**, 1326–1329.
- BAR-ZIV, R., FRISCH, T., and MOSES, E., 1995a, Entropic expulsion in vesicles, *Phys. Rev. Lett.*, **75**, 3481.
- BAR-ZIV, R., MENES, R., MOSES, E., and SAFRAN, S. A., 1995b, Local unbinding of pinched membranes. *Phys. Rev. Lett.*, **75**, 3356–3359.
- BAR-ZIV, R., and MOSES, E., 1994, Instability and pearling states produced in tubular membranes by competition of curvature and tension. *Phys. Rev. Lett.*, **73**, 1392–1395.
- BENVEGNU, D. J., and MC CONNELL, H. M., 1992, Line tension between liquid domains in lipid monolayers. *J. phys. Chem.*, **96**, 6820–6824.

- BERNDL, K., 1990, *Formen von Vesikeln*, Diplomarbeit, Ludwig-Maximilians-Universität, München.
- BERNDL, K., KÄS, J., LIPOWSKY, R., SACKMANN, E., and SEIFERT, U., 1990, Shape transformations of giant vesicles: extreme sensitivity to bilayer asymmetry, *Europhys. Lett.*, **13**, 659–664.
- BEYSENS, D., BOCCARA, N., and FORGACS, G., (editors), 1991, *Dynamical Phenomena at Interfaces, Surfaces and Membranes* (New York: Nova Science).
- BILLOIRE, A., and DAVID, F., 1986, Scaling properties of randomly triangulated planar random surfaces, *Nucl. Phys. B*, **275**, 617–640.
- BIVAS, I., BIVOLARSKI, L., MITOV, M. D., and DERZHANSKI, A., 1992, Correlations between the form fluctuation modes of flaccid quasispherical lipid vesicles and their role in the calculation of the curvature elastic modulus of the vesicle membrane. Numerical results, *J. Phys. II*, **2**, 1423–1438.
- BIVAS, I., HANUSSE, P., BOTHOREL, P., LALANNE, J., and AGUERRE-CHARIOL, O., 1987, An application of the optical microscopy to the determination of the curvature elastic modulus of biological and model membranes, *J. Phys.*, **48**, 855–867.
- BLOOM, M., 1992, The physics of soft, natural materials, *Phys. Canada*, **48**, 7–16.
- BLOOM, M., EVANS, E., and MOURITSEN, O. G., 1991, Physical properties of the fluid lipid-bilayer component of cell membranes: a perspective, *Quart. Rev. Biophys.*, **24**, 293–397.
- BO, L., and WAUGH, R. E., 1989, Determination of bilayer membrane bending stiffness by tether formation from giant, thin-walled vesicles, *Biophys. J.*, **55**, 509–517.
- BOAL, D. H., 1994, Computer simulation of a model network for the erythrocyte cytoskeleton, *Biophys. J.*, **67**, 521–529.
- BOAL, D. H., and RAO, M., 1992a, Scaling behavior of fluid membranes in three dimensions, *Phys. Rev. A*, **45**, 6947–6950; 1992b, Topology changes in fluid membranes, *Ibid.*, **46**, 3037–3045.
- BOAL, D. H., SEIFERT, U., and ZILKER, A., 1992, Dual network model for red blood cell membranes, *Phys. Rev. Lett.*, **69**, 3405–3408.
- BOROSKE, E., ELWENSPOEK, M., and HELFRICH, W., 1981, Osmotic shrinkage of giant egg lecithin vesicles, *Biophys. J.*, **34**, 95–109.
- BOULATOV, D. V., KAZAKOV, V. A., KOSTOV, I. K., and MIGDAL, A. A., 1986, Analytical and numerical study of a model of dynamically triangulated surfaces, *Nucl. Phys. B*, **275**, 641–686.
- BOZIC, B., SVETINA, S., ZEKS, B., and WAUGH, R. E., 1992, Role of lamellar membrane structure in tether formation from bilayer vesicles, *Biophys. J.*, **61**, 963–973.
- BRAKKE, K. A., 1992, The surface evolver, *Exp. Math.*, **1**, 141–165.
- BROCHARD, F., and DE GENNES, P. G., 1975, Hydrodynamic properties of fluid lamellar phases of lipid/water, *Pramana*, **1**, 1–21.
- BROCHARD, F., and LENNON, J. F., 1975, Frequency spectrum of the flicker phenomenon in erythrocytes, *J. Phys. (France)*, **36**, 1035–1047.
- BRUINSMA, R., 1991, Growth instabilities of vesicles, *J. Phys. II France*, **1**, 995–1012; 1995, Adhesion and rolling of leukocytes: a physical model, *Physics of Biomaterials*, NATO ASI series, Geilo, Norway.
- BRUINSMA, R., GOULIAN, M., and PINCUS, P., 1994, Self-assembly of membrane junctions, *Biophys. J.*, **67**, 746–750.
- BRYANT, G., and WOLFE, J., 1987, Electromechanical stresses produced in the plasma membranes of suspended cells by applied electric fields, *J. Membrane Biol.*, **96**, 129–139.
- BRYANT, R., 1984, A duality theorem for Willmore surfaces, *J. Differential Geom.*, **20**, 23–53.
- CAI, W., and LUBENSKY, T. C., 1994, Covariant hydrodynamics of fluid membranes, *Phys. Rev. Lett.*, **73**, 1186–1189; 1995, Hydrodynamics and dynamic fluctuations of fluid membranes, *Phys. Rev. E*, **52**, 4251–4266.
- CAI, W., LUBENSKY, T. C., NELSON, P., and POWERS, T., 1994, Measure factors, tension, and correlations of fluid membranes, *J. Phys. II France*, **4**, 931–949.
- CAMACHO, C. J., and FISHER, M. E., 1990, Tunable fractal shapes in self-avoiding polygons and planar vesicles, *Phys. Rev. Lett.*, **65**, 9–12; 1991, Semiflexible planar polymeric loops, *J. chem. Phys.*, **94**, 5693–5700.

- CANHAM, P. B., 1970, The minimum energy of bending as a possible explanation of the biconcave shape of the human red blood cell, *J. theoret. Biol.*, **26**, 61–81.
- CEVC, G., 1995, *Structure and Dynamics of Membranes*, edited by R. Lipowsky and E. Sackmann (Amsterdam: Elsevier), pp. 465–490.
- CEVC, G., FENZL, W., and SIGL, I., 1990, Surface induced X-ray reflection visualization of membrane orientation and fusion into multibilayers, *Science*, **249**, 1161–1163.
- CEVC, G., and MARSH, D., 1987, *Phospholipid Bilayers: Physical Principles and Models* (New York: Wiley).
- CHANG, D. C., CHASSY, B. M., SAUNDERS, J. A., and SOWERS, A. E., 1992, *Guide to Electroporation and Electrofusion* (San Francisco: Academic Press).
- CHEN, C.-M., LUBENSKY, T. C., and MACINTOSH, F. C., 1995, Phase transitions and modulated phases in lipid bilayers, *Phys. Rev. E*, **51**, 504.
- CHIRUVOLU, S., WALKER, S., ISRAELACHVILI, J., SCHMITT, F. J., LECKBAND, D., and ZASADZINSKI, J. A., 1994, Higher order self-assembly of vesicles by site specific binding, *Science*, **264**, 1753–1756.
- COOK-RÖDER, J., and LIPOWSKY, R., 1992, Adhesion and unbinding for bunches of fluid membranes, *Europhys. Lett.*, **18**, 433–438.
- CROWLEY, J. M., 1973, Electrical breakdown of bimolecular lipid membranes as an electromechanical instability, *Biophys. J.*, **13**, 711–724.
- DAN, N., BERMAN, A., PINCUS, P., and SAFRAN, S., 1994, Membrane-induced interactions between inclusions, *J. Phys. II France*, **4**, 1713–1725.
- DAVID, F., GUITTER, E., and PELITI, L., 1987, Critical properties of fluid membranes with hexatic order, *J. Phys. (France)*, **48**, 2059–2066.
- DAVID, F., and LEIBLER, S., 1991, Vanishing tension of fluctuating membranes, *J. Phys. II France*, **1**, 959–976.
- DE GENNES, P. G., and PROST, J., 1993, *The Physics of Liquid Crystals* (Oxford: Clarendon Press).
- DE GENNES, P. G., and TAUPIN, C., 1982, Microemulsions and the flexibility of oil/water interfaces, *J. chem. Phys.*, **86**, 2294–2304.
- DE LOOF, H., HARVEY, S. C., SEGREST, J. P., and PASTOR, R. W., 1991, Mean field stochastic boundary molecular dynamics simulation of a phospholipid in a membrane, *Biochemistry*, **30**, 2099–2113.
- DEE, G., and LANGER, J., 1983, Propagating pattern selection, *Phys. Rev. Lett.*, **50**, 383–386.
- DEULING, H. J., and HELFRICH, W., 1976, The curvature elasticity of fluid membranes: a catalogue of vesicle shapes, *J. Phys. (France)*, **37**, 1335–1345; 1977, A theoretical explanation for the myelin shapes of red blood cells, *Blood Cells*, **3**, 712–720.
- DIMITROV, D. S., 1984, Electric field induced breakdown of lipid bilayers and cell membranes: a thin viscoelastic film model, *J. Membrane Biol.*, **78**, 53–60.
- DO CARMO, M. P., 1976, *Differential Geometry of Curves and Surfaces* (New Jersey: Prentice-Hall).
- DÖBEREINER, H. G., 1995, *The Budding Transition of Phospholipid Vesicles: A Quantitative Study via Phase Contrast Microscopy*, Ph.D. Thesis, Simon Fraser University, Canada.
- DÖBEREINER, H.-G., EVANS, E., SEIFERT, U., and WORTIS, M., 1995, Spinodal fluctuations of budding vesicles, *Phys. Rev. Lett.*, **75**, 3360–3363.
- DÖBEREINER, H. G., KÄS, J., NOPPL, D., SPRENGER, I., and SACKMANN, E., 1993, Budding and fission of vesicles, *Biophys. J.*, **65**, 1396–1403.
- DOI, M., and EDWARDS, S. F., 1986, *The Theory of Polymer Dynamics* (Oxford: Clarendon Press).
- DUPLANTIER, B., 1990, Exact curvature energies of charged membranes of arbitrary shapes, *Physica A*, **168**, 179–197.
- DUPLANTIER, B., GOLDSTEIN, R. E., ROMERO-ROCHIN, V., and PESCI, A. I., 1990, Geometrical and topological aspects of electric double layers near curved surfaces, *Phys. Rev. Lett.*, **65**, 508–511.
- DUWE, H. P., 1989, *Korrelationsanalyse thermischer Formfluktuationen von Vesikel*, Ph.D. Thesis, Technische Universität München, Germany.
- DUWE, H. P., KÄS, J., and SACKMANN, E., 1990, Bending elastic moduli of lipid bilayers: modulation by solutes, *J. Phys. France*, **51**, 945–962.

- ENGELHARDT, H., DUWE, H. P., and SACKMANN, E., 1985, Bilayer bending elasticity measured by Fourier analysis of thermally excited surface undulations of flaccid vesicles, *J. Phys. Lett. (France)*, **46**, 395–400.
- ENGELHARDT, H., and SACKMANN, E., 1988, On the measurement of shear elastic moduli and viscosities of erythrocyte plasma membranes by transient deformation in high frequency electric fields, *Biophys. J.*, **54**, 495–508.
- EVANS, D. F., and WENNERSTRÖM, H., 1994, *The Colloidal Domain* (New York: VCH).
- EVANS, E., 1974, Bending resistance and chemically induced moments in membrane bilayers, *Biophys. J.*, **14**, 923–931; 1980, Minimum energy analysis of membrane deformation applied to pipet aspiration and surface adhesion of red blood cells, *Ibid.*, **30**, 265–284; 1983, Bending elastic modulus of red blood cell membrane derived from buckling instability in micropipet aspiration tests, *Ibid.*, **43**, 27–30; 1985, Detailed mechanics of membrane–membrane adhesion and separation. I. Continuum of molecular cross-bridges, *Ibid.*, **48**, 175–183; 1990, Adhesion of surfactant–membrane covered droplets: special features and curvature elasticity effects, *Colloids and Surfaces*, **43**, 327–347; 1991, Entropy driven tension in vesicle membranes and unbinding of adherent vesicles, *Langmuir*, **7**, 1900–1908; 1995a, *Structure and Dynamics of Membranes*, edited by R. Lipowsky and E. Sackmann (Amsterdam: Elsevier), pp. 723–754.
- EVANS, E., and METCALFE, M., 1984, Free energy potential for aggregation of mixed phosphatidylcholine/phosphatidylserin lipid vesicles in glucose polymer/dextran solutions, *Biophys. J.*, **45**, 715–720.
- EVANS, E., and NEEDHAM, D., 1987, Physical properties of surfactant bilayer membranes: thermal transitions, elasticity, rigidity, cohesion, and colloidal interactions, *J. chem. Phys.*, **91**, 4219–4228.
- EVANS, E., and RAWICZ, W., 1990, Entropy-driven tension and bending elasticity in condensed-fluid membranes, *Phys. Rev. Lett.*, **64**, 2094–2097.
- EVANS, E., and YEUNG, A., 1994, Hidden dynamics in rapid changes of bilayer shape, *Chem. Phys. Lipids*, **73**, 39–56.
- EVANS, E., YEUNG, A., WAUGH, R., and SONG, J., 1992, *The Structure and Conformation of Amphiphilic Membranes*, edited by R. Lipowsky, D. Richter and K. Kremer, Springer Proceedings in Physics, Vol. 66 (Berlin: Springer), pp. 148–153.
- EVANS, R. M. L., 1995b, Phase diagrams for deformable toroidal and spherical surfaces with intrinsic orientational order, *J. Phys. II France*, **5**, 507–530.
- FARGE, E., and DEVAUX, P. F., 1992, Shape changes of giant liposomes induced by an asymmetric transmembrane distribution of phospholipids, *Biophys. J.*, **61**, 347–357.
- FAUCON, J. F., MITOV, M. D., MELEARD, P., BIVAS, I., and BOTOREL, P., 1989, Bending elasticity and thermal fluctuations of lipid membranes. Theoretical and experimental requirements, *J. Phys. (France)*, **50**, 2389–2414.
- FENZL, W., SIGL, L., RICHARDSEN, H., and CEVC, G., 1995, The surface-confined structures of dimyristoylphosphatidylcholine bilayers in contact with the vesicle suspension as studied by means of X-ray reflectivity, *Colloids and Surfaces A*, **102**, 247–256.
- FISCHER, T. M., 1993, Bending stiffness of lipid bilayers. V. Comparison of two formulations, *J. Phys. II France*, **3**, 1795–1805; 1994, Mechanisms for determining the time scales in vesicle budding, *Phys. Rev. E*, **50**, 4156–4166.
- FOLTIN, G., 1994, Dynamics of incompressible fluid membranes, *Phys. Rev. E*, **49**, 5243–5248.
- FÖRSTER, D., 1986, On the scale dependence, due to thermal fluctuations, of the elastic properties of membranes, *Phys. Lett. A*, **114**, 115–120.
- FOURCADE, B., 1992, Theoretical results of toroidal vesicles, *J. Phys. II France*, **2**, 1705–1724.
- FOURCADE, B., MIAO, L., RAO, M., WORTIS, M., and ZIA, R. K. P., 1994, Scaling analysis of narrow necks in curvature models of fluid lipid–bilayer vesicles. *Phys. Rev. E*, **49**, 5276–5286.
- FOURCADE, B., MUTZ, M., and BENSIMON, D., 1992, Experimental and theoretical study of toroidal vesicles, *Phys. Rev. Lett.*, **68**, 2551–2554.
- FREY, E., and NELSON, D. R., 1991, Dynamics of flat membranes and flickering in red blood cells, *J. Phys. I France*, **1**, 1715–1757.

- FROMHERZ, P., 1983, Lipid-vesicle structure: size control by edge-active agents, *Chem. Phys. Lett.*, **94**, 259–266.
- GEBHARDT, C., GRULER, H., and SACKMANN, E., 1977, On domain structure and local curvature in lipid bilayers and biological membranes, *Z. Naturforsch.*, C, **32**, 581–596.
- GOLDSTEIN, R. E., NELSON, P., POWERS, T., and SEIFERT, U., 1996, Front propagation in the pearlring instability of tubular vesicles, *J. Phys. II France*, **6**, 767–796.
- GOMPPER, G., and KROLL, D. M., 1989, Steric interactions in multimembrane systems: a Monte Carlo study, *Europhys. Lett.*, **9**, 59–64; 1992a, Inflated vesicles: a new phase of fluid membranes, *Ibid.*, **19**, 581–586; 1992b, Shape of inflated vesicles, *Phys. Rev. A*, **46**, 7466; 1993, Floppy fluid vesicles in elongational flow, *Phys. Rev. Lett.*, **71**, 1111–1114; 1994, Phase diagram of fluid vesicles, *Ibid.*, **73**, 2139–2142; 1995a, Driven transport of fluid vesicles through narrow pores, *Phys. Rev. E*, **52**, 4198–4208; 1995b, Phase diagram and scaling behavior of fluid vesicles, *Ibid.*, **51**, 512–525.
- GOMPPER, G., and SCHICK, M., 1994, Self assembling amphiphilic systems, *Phase Transition and Critical Phenomena*, edited by C. Domb and J. Lebowitz (London: Academic).
- GOOS, J., and GOMPPER, G., 1993, Topological defects in lamellar phases: passages, and their fluctuations, *J. Phys. I France*, **3**, 1551–1567.
- GOULIAN, M., BRUINSMA, R., and PINCUS, P., 1993, Long-range forces in heterogeneous fluid membranes, *Europhys. Lett.*, **22**, 145–150.
- GRANEK, R., and OLAMI, Z., 1995, Dynamics of Rayleigh-like instability induced by laser tweezers in tubular vesicles of self-assembled membranes, *J. Phys. II France*, **5**, 1349–1370.
- GRULER, H., 1975, Chemoelastic effects of membranes, *Z. Naturforsch. C*, **30**, 608–614.
- HAECKL, W., SEIFERT, U., and SACKMANN, E., 1995, Effects of fully and partially solubilized amphiphiles on bilayers bending stiffness and temperature dependence of the effective tension of giant vesicles (preprint).
- HEINRICH, V., BRUMEN, M., HEINRICH, R., SVETINA, S., and ZEKS, B., 1992, Nearly spherical vesicle shapes calculated by use of spherical harmonics: axisymmetric and nonaxisymmetric shapes and their stability, *J. Phys. II France*, **2**, 1081–1108.
- HEINRICH, V., SVETINA, S., and ZEKS, B., 1993, Nonaxisymmetric vesicle shapes in a generalized bilayer-couple model and the transition between oblate and prolate axisymmetric shapes, *Phys. Rev. E*, **48**, 3112–3123.
- HELFRICH, W., 1973, Elastic properties of lipid bilayers: theory and possible experiments, *Z. Naturforsch. C*, **28**, 693–703; 1974a, Blocked lipid exchanges in bilayers and its possible influence on the shape of vesicles, *Ibid.*, **29**, 510–515; 1974b, The size of bilayer vesicles generated by sonication, *Phys. Lett. A*, **50**, 115–116; 1978, Steric interaction of fluid membranes in multilayer systems, *Z. Naturforsch.*, **33**, 305–315; 1985, Effect of thermal undulations on the rigidity of fluid membranes and interfaces, *J. Phys. (France)*, **46**, 1263–1268; 1986, Size distributions of vesicles: the role of the effective rigidity of membranes, *Ibid.*, **47**, 321–329; 1987, Measures of integration in calculating the effective rigidity of fluid surfaces, *Ibid.*, **48**, 285–289; 1989, Hats and saddles in liquid membranes, *Liq. Crystals*, **5**, 1647–1658; 1993, Mean field theory of n-layer unbinding, *J. Phys. II France*, **3**, 385–393; 1994, Lyotropic lamellar phases, *J. Phys.: condens. Matter*, **6**, A79–A92; 1995, *Structure and Dynamics of Membranes*, edited by R. Lipowsky and E. Sackmann (Amsterdam: Elsevier), pp. 691–722.
- HELFRICH, W., and KLÖSGEN, B., 1992, *Dynamical Phenomena at Interfaces, and Surfaces and Membranes*, edited by D. Beysens, N. Boccara and G. Forgacz (New York: Nova), pp. 211–220.
- HELFRICH, W., and KOZLOV, M. M., 1994, Flexibility and roughness of mixed and partially polymerized bilayers in terms of the hat model and local bending frustration, *J. Phys. II France*, **4**, 1427–1438.
- HELFRICH, W., and PROST, J., 1988, Intrinsic bending force in anisotropic membranes made of chiral molecules, *Phys. Rev. A*, **38**, 3065–3068.
- HELFRICH, W., and SERVUSS, R. M., 1984, Undulations, steric interaction and cohesion of fluid membranes, *Il Nuovo Cimento*, D, **3**, 137–151.
- HO, J. S., and BAUMGÄRTNER, A., 1990, Simulation of fluid self-avoiding membranes, *Europhys. Lett.*, **12**, 295–300.

- HOFFMAN, H., THUNIG, C., MUNKERT, U., MEYER, H. W., and RICHTER, W., 1992, From vesicles to the  $L_3$  (sponge) phase in alkyldimethylamine oxide/heptanol systems, *Langmuir*, **8**, 2629–2638.
- HOMAN, R., and POWNALL, H. J., 1988, Transbilayer diffusion of phospholipids: dependence on headgroup structure and acyl chain length, *Biochim. Biophys. Acta*, **938**, 155–166.
- HOTANI, H., 1984, Transformation pathways of liposomes, *J. molec. Biol.*, **178**, 113–120.
- HSU, L., KUSNER, R., and SULLIVAN, J., 1992, Minimizing the squared mean curvature integral for surfaces in space forms, *Exp. Math.*, **1**, 191–207.
- HU, J.-G., and OU-YANG, Z.-C., 1993, Shape equations of the axisymmetric vesicles, *Phys. Rev. E*, **47**, 461–467.
- HYUGA, H., KINOSITA, K., JR, and WAKABAYASHI, N., 1991a, Deformation of vesicles under the influence of strong electric fields, *Jap. J. appl. Phys.*, **30**, 1141–1148; 1991b, Deformation of vesicles under the influence of strong electric fields. II, *Ibid.*, **30**, 1333–1335.
- ISRAELACHVILI, J. N., 1991, *Intermolecular and Surface Forces*, second edn (London: Academic Press).
- ISRAELACHVILI, J. N., and WENNERSTRÖM, H., 1990, Hydration or steric forces between amphiphilic surfaces? *Langmuir*, **6**, 873–876.
- JANIAK, M. J., SMALL, D. M., and SHIPLEY, G. G., 1979, Temperature and compositional dependence of the structure of hydrated dimyristoyl lecithin, *J. biol. Chem.*, **254**, 6068–6078.
- JANKE, W., and KLEINERT, H., 1987, Fluctuation pressure of a stack of membranes, *Phys. Rev. Lett.*, **58**, 144–147.
- JARIC, M., SEIFERT, U., WINTZ, W., and WORTIS, M., 1995, Vesicular instabilities: the prolate-to-oblate transition and other shape instabilities of fluid bilayer membranes, *Phys. Rev. E*, **52**, 6623.
- JENKINS, J. T., 1977, Static equilibrium configurations of a model red blood cell, *J. math. Biol.*, **4**, 149–169.
- JÜLICHER, F., 1993, *Die Morphologie von Vesikeln*, Ph.D. Thesis, Universität zu Köln, Germany.
- JÜLICHER, F., and LIPOWSKY, R., 1993, Domain induced budding of vesicles, *Phys. Rev. Lett.*, **70**, 2964–2967.
- JÜLICHER, F., and SEIFERT, U., 1994, Shape equations for axisymmetric vesicles: a clarification, *Phys. Rev. E*, **49**, 4728–4731.
- JÜLICHER, F., SEIFERT, U., and LIPOWSKY, R., 1993a, Conformal degeneracy and conformal diffusion of vesicles, *Phys. Rev. Lett.*, **71**, 452–455; 1993b, Phase diagrams and shape transformations of toroidal vesicles, *J. Phys. II France*, **3**, 1681–1705.
- KALER, E. W., HERRINGTON, K. L., MURTHY, A. K., and ZASADZINSKI, J. A. N., 1992, Phase behavior and structures of mixtures of anionic and cationic surfactants, *J. phys. Chem.*, **96**, 6698–6707.
- KALER, E. W., MURTHY, A. K., RODRIGUEZ, B. E., and ZASADZINSKI, J. A. N., 1989, Spontaneous vesicle formation in aqueous mixtures of single-tailed surfactants, *Science*, **245**, 1371–1374.
- KARCHER, H., PINKALL, U., and STERLING, I., 1988, New minimal surfaces in  $S^3$ , *J. Differential Geom.*, **28**, 169–185.
- KÄS, J., and SACKMANN, E., 1991, Shape transitions and shape stability of giant phospholipid vesicles in pure water induced by area-to-volume changes, *Biophys. J.*, **60**, 825–844.
- KÄS, J., SACKMANN, E., PODGORNIK, R., SVETINA, S., and ZEKS, B., 1993, Thermally induced budding of phospholipid vesicles—a discontinuous process, *J. Phys. II France*, **3**, 631–645.
- KAWAKATSU, T., ANDELMAN, D., KAWASAKI, K., and TANIGUCHI, K., 1993, Phase transitions and shape of two component membranes and vesicles. I: Strong segregation limit, *J. Phys. II France*, **3**, 971–997.
- KLEINERT, H., 1986, Thermal softening of curvature elasticity in membranes, *Phys. Lett.*, **A**, **114**, 263–268.
- KOMURA, S., and LIPOWSKY, R., 1992, Fluctuations and stability of polymerized vesicles, *J. Phys. II France*, **3**, 1563–1575.

- KRAMER, L., 1971, Theory of light scattering from fluctuations of membranes and monolayers, *J. chem. Phys.*, **55**, 2097–2105.
- KRAUS, M., and SEIFERT, U., 1994, Relaxation modes of an adhering bilayer membrane, *J. Phys. II France*, **4**, 1117–1134.
- KRAUS, M., SEIFERT, U., and LIPOWSKY, R., 1995, Gravity-induced shape transformations of vesicles, *Europhys. Lett.*, **32**, 431–436.
- KROLL, D. M., and GOMPPER, G., 1992, The conformation of fluid membranes: Monte Carlo simulations, *Science*, **255**, 968–971; 1993, Floppy tethered networks, *J. Phys. I France*, **3**, 1131–1140.
- KUMMROW, M., and HELFRICH, W., 1991, Deformation of giant lipid vesicles by electric fields, *Phys. Rev. A*, **44**, 8356–8360.
- KUSNER, R., 1989, Comparison surfaces of the Willmore problem, *Pacific J. Math.*, **138**, 317–345.
- KUSNER, R., 1994, Private communication.
- LAMMERT, P. E., PROST, J., and BRUINSMA, R., 1996, Ion drive for vesicles and cells, *J. theoret. Biol.*, **178**, 387–391.
- LANDAU, L. D., and LIFSHITZ, E. M., 1989, *Elastizitätstheorie* (Berlin: Akademie-Verlag).
- LANGER, J., and SINGER, D., 1984, Curves in the hyperbolic plane and mean curvature of tori and  $R^3$  and  $S^3$ , *Bull. London Math. Soc.*, **16**, 531–534.
- LANGER, S. A., and SEIFERT, U., 1996, in preparation.
- LANGEVIN, D., 1992, *Light Scattering by Liquid Surfaces and Complementary Techniques* (New York: Marcel Dekker).
- LASIC, D. D., 1995, *Structure and Dynamics of Membranes*, edited by R. Lipowsky and E. Sackmann (Amsterdam: Elsevier), pp. 491–520.
- LAWSON, H. B., 1970, *Ann. Math.*, **92**, 335–374.
- LE DOUSSAL, P., and RADZHOVSKY, L., 1992, Self-consistent theory of polymerized membranes, *Phys. Rev. Lett.*, **69**, 1209–1212.
- LEIBLER, S., 1986, Curvature instability in membranes, *J. Phys. (France)*, **47**, 507–516.
- LEIBLER, S., and ANDELMAN, D., 1987, Ordered and curved meso-structures in membranes and amphiphilic films, *J. Phys.*, **48**, 2013–2018.
- LEIBLER, S., SINGH, R. R. P. and FISHER, M. E., 1987, Thermodynamic behavior of two-dimensional vesicles, *Phys. Rev. Lett.*, **59**, 1989–1992.
- LIPOWSKY, R., 1990, *Fundamental Problems in Statistical Mechanics VII*, edited by H. van Beijeren (Amsterdam: Elsevier), pp. 139–170; 1991, The conformation of membranes, *Nature*, **349**, 475–481; 1992, Budding of membranes induced by intramembrane domains, *J. Phys. II France*, **2**, 1825–1840; 1993, Domain-induced budding of fluid membranes, *Biophys. J.*, **64**, 1133–1138; 1995, *Structure and Dynamics of Membranes*, edited by R. Lipowsky and E. Sackmann (Amsterdam: Elsevier), pp. 521–602.
- LIPOWSKY, R., and GIRARDET, M., 1990, Shape fluctuations of polymerized or solidlike membranes, *Phys. Rev. Lett.*, **65**, 2893–2896.
- LIPOWSKY, R., and GROTEHANS, S., 1993, Hydration versus protrusion forces between lipid bilayers, *Europhys. Lett.*, **23**, 599–604.
- LIPOWSKY, R., and LEIBLER, S., 1986, Unbinding transitions of interacting membranes, *Phys. Rev. Lett.*, **56**, 2541–2544.
- LIPOWSKY, R., RICHTER, D., and KREMER, K. (editors), 1992, *The Structure and Conformation of Amphiphilic Membranes*, Springer Proceedings in Physics, Vol. 66 (Berlin: Springer).
- LIPOWSKY, R., and SACKMANN, E., 1995, *Structure and Dynamics of Membranes* (Amsterdam: Elsevier).
- LIPOWSKY, R., and SEIFERT, U., 1991a, Adhesion of membranes: a theoretical perspective, *Langmuir*, **7**, 1867–1873; 1991b, Adhesion of vesicles and membranes, *Molec. Crystals, Liq. Crystals*, **202**, 17–25.
- LIPOWSKY, R., and ZIELINSKA, B., 1989, Binding and unbinding of lipid membranes: a Monte Carlo study, *Phys. Rev. Lett.*, **62**, 1572–1575.
- LUBENSKY, T. C., and MACINTOSH, F. C., 1993, Theory of ripple phases of lipid bilayers, *Phys. Rev. Lett.*, **71**, 1565–1568.
- LUBENSKY, T. C., and PROST, J., 1992, Orientational order and vesicle shape, *J. Phys. II France*, **2**, 371–382.

- LUKE, J. C., 1982, A method for the calculation of vesicle shapes, *SIAM J. appl. Math.*, **42**, 333–345.
- LUKE, J. C., and KAPLAN, J. I., 1979, On theoretical shapes of bilayer lipid vesicles under conditions of increasing membrane area, *Biophys. J.*, **25**, 107–111.
- MACINTOSH, F. C., and LUBENSKY, T. C., 1991, Orientational order, topology, and vesicle shapes, *Phys. Rev. Lett.*, **67**, 1169–1172.
- MAGGS, A. C., and LEIBLER, S., 1990, Adsorption and fluctuations of two-dimensional vesicles, *Europhys. Lett.*, **12**, 19–24.
- MAGGS, A. C., LEIBLER, S., FISHER, M. E., and CAMACHO, C. J., 1990, Size of an inflated vesicle in two dimensions, *Phys. Rev. A*, **42**, 691–695.
- MARATHE, Y., and RAMASWAMY, S., 1989, Frequency-dependent viscosity of membrane solution, *Europhys. Lett.*, **8**, 581–585.
- MARKIN, V. S., 1981, Lateral organization of membranes and cell shapes, *Biophys. J.*, **36**, 1–19.
- MARRA, J., and ISRAELACHVILI, J. N., 1985, Direct measurements of forces between phosphatidylcholine and phosphatidylethanolamine bilayers in aqueous electrolyte solutions, *Biochemistry*, **24**, 4608–4618.
- MARSH, D., 1990, *Handbook of Lipid Bilayers*, (Boca Raton, Florida: CRC Press).
- MECKE, K. R., 1995, Bending rigidity of fluctuating membranes, *Z. Phys. B*, **97**, 379–387.
- MELEARD, P., FAUCON, J. F., MITOV, M. D., and BOTHEREL, P., 1992, Pulsed-light microscopy applied to the measurement of the bending elasticity of giant liposomes, *Europhys. Lett.*, **19**, 267–271.
- MENGER, F. M., and GABRIELSON, K. D., 1995, Die cytomimetische organische Chemie—ein erster Bericht, *Angew. Chem.*, **107**, 2260–2278.
- MERKEL, R., SACKMANN, E., and EVANS, E., 1989, Molecular friction and epitactic coupling between monolayers in supported bilayers, *J. Phys. (France)*, **50**, 1535–1555.
- MERMIN, N. D., and WAGNER, H., 1966, Absence of ferromagnetism or antiferromagnetism in one- or two-dimensional isotropic Heisenberg models, *Phys. Rev. Lett.*, **17**, 1133–1136.
- MEUNIER, J., LANGEVIN, D., and BOCCARA, N., 1987, *Physics of Amphiphilic Layers* (Berlin: Springer-Verlag).
- MIAO, L., 1992, Equilibrium shapes and shape transitions of fluid lipid-bilayer vesicles, *Ph.D. Thesis*, Simon Fraser University, Canada.
- MIAO, L., FOURCADE, B., RAO, M., WORTIS, M., and ZIA, R. K. P., 1991, Equilibrium budding and vesiculation in the curvature model of fluid lipid vesicles, *Phys. Rev. A*, **43**, 6843–6856.
- MIAO, L., SEIFERT, U., WORTIS, M., and DÖBEREINER, H. G., 1994, Budding transitions of fluid-bilayer vesicles: the effect of area difference elasticity, *Phys. Rev. E*, **49**, 5389–5407.
- MICHALET, X., 1994, *Etude expérimentale de vésicule phospholipidiques de genre topologique non sphérique*, *Ph.D. Thesis*, l'Université de Paris, VII, France.
- MICHALET, X., and BENSIMON, D., 1995a, Vesicles of toroidal topology: observed morphology and shape transformations, *J. Phys. II France*, **5**, 263–287; 1995b, Observation of stable shapes and conformal diffusion in genus 2 vesicles, *Science*, **269**, 666.
- MICHALET, X., BENIMON, D., and FOURCADE, B., 1994a, Fluctuation vesicles of nonspherical topology, *Phys. Rev. Lett.*, **72**, 168–171.
- MICHALET, X., JÜLICHER, F., FOURCADE, B., SEIFERT, U., and BENIMON, D., 1994b, La physique des liposomes, *La Recherche*, **25**, 1012–1018.
- MILNER, S. T., and ROUX, D., 1992, Flory theory of the unbinding transition, *J. Phys. I France*, **2**, 1741–1754.
- MILNER, S. T., and SAFRAN, S. A., 1987, Dynamical fluctuations of droplet microemulsions and vesicles, *Phys. Rev. A*, **36**, 4371–4379.
- MORSE, D. C., and MILNER, S. T., 1994, Fluctuation and phase behavior of fluid membrane vesicles, *Europhys. Lett.*, **26**, 565–570; 1995, Statistical mechanics of closed fluid membranes, *Phys. Rev. E*, **52**, 5918.
- MOY, V. T., FLORIN, E.-L., and GAUB, H. E., 1994, Intermolecular forces and energies between ligands and receptors, *Science*, **266**, 257–259.

- MUI, B. L.-S., DÖBEREINER, H.-G., MADDEN, T. D., and CULLIS, P. R., 1995, Influence of transbilayer area asymmetry on the morphology of large unilamellar vesicles, *Biophys. J.*, **69**, 930–941.
- MUTZ, M., and BENSIMON, D., 1991, Observation of toroidal vesicles, *Phys. Rev. A*, **43**, 4525–4527.
- MUTZ, M., and HELFRICH, W., 1989, Unbinding transition of a biological model membrane, *Phys. Rev. Lett.*, **62**, 2881–2884; 1990, Bending rigidities of some biological model membranes as obtained from the Fourier analysis of contour sections, *J. Phys. (France)*, **51**, 991–1002.
- NAITO, H., OKUDA, M., and ZHONG-CAN, O. Y., 1993, Counterexample to some shape equations for axisymmetric vesicles, *Phys. Rev. E*, **48**, 2304–2307; 1995, New solutions to the Helfrich variational problem for the shapes of lipid bilayer vesicles: beyond Delaunay surfaces, *Phys. Rev. Lett.*, **74**, 4345–4348.
- NEEDHAM, D., and HOCHMUTH, R. M., 1989, Electro-mechanical permeabilization of lipid vesicles, *Biophys. J.*, **55**, 1001–1009.
- NEEDHAM, D., MCINTOSH, T. J., and EVANS, E., 1988, Thermomechanical and transition properties of dimyristoylphosphatidylcholine/cholesterol bilayers, *Biochemistry*, **27**, 4668–4673.
- NELSON, D., 1988, *Random Fluctuations and Pattern Growth*, edited by H. E. Stanley and N. Ostrowsky, pp. 193–215.
- NELSON, D., PIRAN, T., and WEINBERG, S. (editors), 1989, *Statistical Mechanics of Membranes and Surfaces* (Singapore: World Scientific).
- NELSON, D. R., and PELITI, L., 1987, Fluctuation in membranes with crystalline and hexatic order, *J. Phys. France*, **48**, 1085–1092.
- NELSON, P., and POWERS, T., 1992, Rigid chiral membranes, *Phys. Rev. Lett.*, **69**, 3409–3412; 1993, Renormalization of chiral couplings in tilted bilayer membranes, *J. Phys. II France*, **3**, 1535–1569.
- NELSON, P., POWERS, T., and SEIFERT, U., 1995, Dynamical theory of the pearling instability in cylindrical vesicles, *Phys. Rev. Lett.*, **74**, 3384.
- NETZ, R. R., 1995, Complete unbinding of fluid membranes in the presence of short-range forces, *Phys. Rev. E*, **51**, 2286–2294.
- NETZ, R. R., and LIPOWSKY, R., 1993, Unbinding of symmetric and asymmetric stacks of membranes, *Phys. Rev. Lett.*, **71**, 3596–3599; 1995, Stacks of fluid membranes under pressure and tension, *Europhys. Lett.*, **29**, 345–350.
- NEUMANN, E., SOWERS, A. E., and JORDAN, C. A. (editors), 1989, *Electroporation and Electrofusion in Cell Biology* (New York: Plenum Press).
- NEZIL, F. A., and BLOOM, M., 1992, Combined influence of cholesterol and synthetic amphiphilic peptides upon bilayer thickness in model membranes, *Biophys. J.*, **61**, 1176–1183.
- NIGGEMANN, G., KUMMROW, M., and HELFRICH, W., 1995, The bending rigidity of phosphatidylcholine bilayers: dependence on experimental method, sample cell sealing and temperature, *J. Phys. II France*, **5**, 413–425.
- OU-YANG, Z. C., 1990, Anchor ring-vesicle membranes, *Phys. Rev. A*, **41**, 4517–4520.
- OU-YANG, Z. C., and HELFRICH, W., 1987, Instability and deformation of a spherical vesicle by pressure, *Phys. Rev. Lett.*, **59**, 2486–2488; 1989, Bending energy of vesicle membranes: general expressions for the first, second and third variation of the shape energy and applications to spheres and cylinders, *Phys. Rev. A*, **39**, 5280–5288.
- PALMER, K. M., GOULIAN, M., and PINCUS, P., 1994, Fluctuation-induced forces in stacked fluid membranes, *J. Phys. II France*, **4**, 805–817.
- PARK, J., LUBENSKY, T. C., and MACKINTOSH, F. C., 1992, *n*-atic order and continuous shape changes of deformable surfaces of the genus zero, *Europhys. Lett.*, **20**, 279–284.
- PARSEGAN, V. A., FULLER, N., and RAND, R. P., 1979, Measured work of deformation and repulsion of lecithin bilayers, *Natl Acad. Sci. USA*, **76**, 2750–2854.
- PARSEGAN, V. A., and RAND, R. P., 1995, *Structure and Dynamics of Membranes* edited by R. Lipowsky and E. Sackmann (Amsterdam: Elsevier), pp. 643–690.
- PELITI, L., 1991, *Biologically Inspired Physics* (New York and London: Plenum Press).
- PELITI, L., and LEIBLER, S., 1995, Effects of thermal fluctuations on systems with small surface tension, *Phys. Rev. Lett.*, **54**, 1690–1693.

- PELITI, L., and PROST, J., 1989, Fluctuations in membranes with reduced symmetry, *J. Phys. France*, **50**, 1557–1571.
- PETERSON, M. A., 1985a, Geometrical methods for the elasticity theory of membranes, *J. math. Phys.*, **26**, 711–717; 1985b, An instability of the red blood cell shape, *J. appl. Phys.*, **57**, 1739–1742; 1985c, Shape fluctuations of red blood cells, *Molec. Crystals, Liq. Crystals.*, **127**, 159–186; 1988, Comment on ‘Instability and deformation of a spherical vesicle by pressure’, *Phys. Rev. Lett.*, **61**, 1325; 1989, Deformation energy of vesicles at fixed volume and surface area in the spherical limit, *Phys. Rev. A*, **39**, 2643–2645; 1992, Linear response of the human erythrocyte to mechanical stress, *Phys. Rev. A*, **45**, 4116–4131.
- PETERSON, M. A., STREY, H., and SACKMANN, E., 1992, Theoretical and phase contrast microscopic eigenmode analysis of erythrocyte flicker: amplitudes, *J. Phys. II France*, **2**, 1273–1285.
- PFEIFFER, W., KÖNIG, S., LEGRAND, J. F., BAYERL, T., RICHTER, D., and SACKMANN, E., 1993, Neutron spin echo study of membrane undulations in lipid multibilayers, *Europhys. Lett.*, **23**, 457–462.
- PINCUS, P., 1976, Excluded volume effects and stretched polymer chains, *Macromolecules*, **9**, 386–388.
- PINKALL, U., 1985, Hopf tori in  $S^3$ , *Invent. Math.*, **81**, 379–386.
- PINKALL, U., and STERLING, I., 1987, Willmore surfaces, *Math. Intelligencer*, **9**, 38–43.
- PODGORNÍK, R., SVETINA, S., and ZEKS, B., 1995, Parametrization invariance and shape equations of elastic axisymmetric vesicles, *Phys. Rev. E*, **51**, 544.
- POLYAKOV, A. M., 1987, *Gauge Fields and Strings* (Cambridge, MA: Harvard Academic Publishers).
- PORTE, G., 1992, Lamellar phases and disordered phase of fluid bilayer membranes, *J. Phys.: condens. Matter*, **4**, 8649–8670.
- POWERS, T., and NELSON, P., 1995, Fluctuating membranes with tilt order, *J. Phys. II France*, **5**, 1671–1678.
- PROST, J., and BRUINSMA, R., 1996, Shape fluctuation of active membranes, *Europhys. Lett.*, **33**, 321–326.
- RÄDLER, J., 1993, *Über Wechselwirkung flüider Phospholipid-Membranen mit Festkörperoberflächen*, Ph.D. Thesis, TU-München, Germany.
- RÄDLER, J., and SACKMANN, E., 1992, *The Structure and Conformation of Amphiphilic Membranes*, edited by R. Lipowsky, D. Richter and K. Kremer (Berlin: Springer), pp. 158–161.
- RÄDLER, J. O., FEDER, T. J., STREY, H. H., and SACKMANN, E., 1995, Fluctuation analysis of tension controlled undulation forces between giant vesicles and solid substrates, *Phys. Rev. E*, **51**, 4526–4536.
- RAND, R. P., and PARSEGIAN, V. A., 1989, Hydration forces between phospholipid bilayers, *Biochim. Biophys. Acta*, **988**, 351–376.
- ROUX, D., COULON, C., and CATES, M. E., 1992, Sponge phases in surfactant solutions, *J. phys. Chem.*, **96**, 4174–4187.
- SACKMANN, E., 1994, Membrane bending energy concept of vesicle- and cell-shapes and shape-transitions, *FEBS Letters*, **346**, 3–16.
- SAFRAN, S., 1994, *Statistical Thermodynamics of Surfaces, Interfaces, and Membranes* (Reading, UK: Addison-Wesley).
- SAFRAN, S. A., PINCUS, P., and ANDELMAN, D., 1990, Theory of spontaneous vesicle formation in surfactant mixtures, *Science*, **248**, 354–356.
- SAFRAN, S. A., PINCUS, P. A., ANDELMAN, D., and MACKINTOSH, F. C., 1991, Stability and phase behavior of mixed surfactant vesicles, *Phys. Rev. A*, **43**, 1071–1078.
- SCHMIDT, C. F., SVOBODA, K., LEI, N., PETSCHE, I. B., BERMAN, L. E., SAFINYA, C. R., and GREST, G. S., 1993, Existence of a flat phase in red cell membrane skeletons, *Science*, **259**, 952–955.
- SCHNEIDER, M. B., JENKINS, J. R., and WEBB, W. W., 1984a, Thermal fluctuations of large cylindrical phospholipid vesicles, *Biophys. J.*, **45**, 891–899; 1984b, Thermal fluctuations of large quasi-spherical bimolecular phospholipid vesicles, *J. Phys. France*, **45**, 1457–1472.

- SCHNITZLER, W., 1993, *Simulation und Analyse dreidimensionaler Vesikel- und Erythrozytenformen*, Diplomarbeit RWTH Aachen, Germany.
- SEIFERT, U., 1990, Shape transformation and free, toroidal and bound vesicles, *J. de Physique, Colloque*, **51**, C7, 339–344; 1991a, Adhesion of vesicles in two dimensions, *Phys. Rev. A*, **43**, 6803–6814; 1991b, Conformal transformations of vesicle shapes, *J. Phys. (A)*, **24**, L573–578; 1991c, Vesicles of toroidal topology, *Phys. Rev. Lett.*, **66**, 2404–2407; 1993, Curvature-induced lateral phase segregation in two component vesicles, *Ibid.*, **70**, 1335–1338; 1994, Dynamics of a bound membrane, *Phys. Rev. E*, **49**, 3124–3127; 1995a, The concept of effective tension for fluctuating vesicles, *Z. Physik B*, **97**, 299–309; 1995b, *Fluid membranes—theory of vesicle conformations*, *Habilitation Thesis*, Juel-Bericht 2997, Forschungszentrum Jülich; 1995c, *Interplay of Genetic and Physical Processes in the Development of Biological Form*, Les Houches Series, edited by D. Felix, M. A. Beysens, F. Gaill and G. Forgacs (Singapore: World Scientific), pp. 38–44; 1995d, Self-consistent theory of bound vesicles, *Phys. Rev. Lett.*, **74**, 5060–5063.
- SEIFERT, U., BERNDL, K., and LIPOWSKY, R., 1991, Shape transformations of vesicles: phase diagrams for spontaneous curvature and bilayer-coupling models, *Phys. Rev. A*, **44**, 1182–1202.
- SEIFERT, U., and LANGER, S. A., 1993, Viscous modes of fluid bilayer membranes, *Europhys. Lett.*, **23**, 71–76; 1994, Hydrodynamics of membranes: the bilayer aspect and adhesion, *Biophys. Chem.*, **49**, 13–22.
- SEIFERT, U., and LIPOWSKY, R., 1990, Adhesion of vesicles, *Phys. Rev. A*, **42**, 4768–4771; 1993, *Dynamical Phenomena at Interfaces, Surfaces and Membranes*, edited by D. Beysens, N. Boccara and G. Forgacs (New York: Nova), pp. 295–304.
- SEIFERT, U., MIAO, L., DÖBEREINER, H. G., and WORTIS, M., 1992, *The Structure and Conformation of Amphiphilic Membranes*, Springer Proceedings in Physics, Vol. 66, edited by R. Lipowsky, D. Richter and K. Kremer, (Berlin: Springer), pp. 93–96.
- SELINGER, J. V., and SCHNUR, J. M., 1993, Theory of chiral lipid tubules, *Phys. Rev. Lett.*, **71**, 4091–4094.
- SERVUSS, R. M., HARBICH, W., and HELFRICH, W., 1976, Measurements of the curvature elastic modulus of egg lecithin bilayers, *Biochim. Biophys. Acta*, **436**, 900–903.
- SERVUSS, R. M., and HELFRICH, W., 1989, Mutual adhesion of lecithin membranes at ultralow tensions, *J. Phys. (France)*, **50**, 809–827.
- SEUNG, H. S., and NELSON, D. R., 1988, Defects in flexible membranes with crystalline order, *Phys. Rev. A*, **38**, 1005–1018.
- SHEET, M. P., and SINGER, S. J., 1974, Biological membranes as bilayer couples. A molecular mechanism of drug-erythrocyte interactions, *Proc. Natl. Acad. Sci. (USA)*, **71**, 4457–4461.
- SONG, J., and WAUGH, R. E., 1993, Bending rigidity of SOPC membranes containing cholesterol, *Biophys. J.*, **64**, 1967–1970.
- SPECTOR, M. S., NARANJO, E., CHIRUVOLU, S., and ZASADZINSKI, J. A., 1994, Conformations of a tethered membrane: crumpling in graphite oxide? *Phys. Rev. Lett.*, **73**, 2867.
- STECK, T. L., 1989, *Cell Shape Determinants, Regulations, and Regulatory Role*, edited by W. Stein and F. Bronner (New York: Academic Press), pp. 205–246.
- STOKKE, B. T., MIKKELSEN, A., and ELGSAETER, A., 1986a, The human erythrocyte membrane skeleton may be an ionic gel. I. Membrane mechanochemical properties, *Eur. Biophys. J.*, **13**, 203–218; 1986b, The human erythrocyte membrane skeleton may be an ionic gel. II. Numerical analyses of cell shapes and shape transformations, *Ibid.*, **13**, 219–233.
- STREY, H., PETERSON, M., and SACKMANN, E., 1995, Measurement of erythrocyte membrane elasticity by flicker eigenmode decomposition, *Biophys. J.*, **69**, 478–488.
- SVETINA, S., OTTOVA-LEITMANOVA, A., and GLASER, R., 1982, Membrane bending energy in relation to bilayer couples concept of red blood cell shape transformations, *J. theoret. Biol.*, **94**, 13–23.
- SVETINA, S., and ZEKS, B., 1983, Bilayer couple hypothesis of red cell shape transformations and osmotic hemolysis, *Biochim. Biophys. Acta*, **42**, 86–90; 1989, Membrane bending energy and shape determination of phospholipid vesicles and red blood cells, *Eur.*

- Biophys. J.*, **17**, 101–111; 1992, The elastic deformability of closed multilayered membranes is the same as that of a bilayer membrane, *Ibid.*, **21**, 251–255.
- SOVODA, K., SCHMIDT, C. F., BRANTON, D., and BLOCK, S. M., 1992, Conformation and elasticity of the isolated red blood cell membrane skeleton, *Biophys. J.*, **63**, 784–793.
- TANIGUCHI, T., KAWASAKI, K., ANDELMAN, D., and KAWAKATSU, T., 1994, Equilibrium shape deformations of two-component vesicles, *J. Phys. II France*, **4**, 1333–1362.
- TERSOFF, J., 1992, Energies of fullerenes, *Phys. Rev. B*, **46**, 15546–15549.
- THOMSEN, G., 1924, Grundlagen der konformen Flächentheorie, *Abh. Math. Sem. Univ. Hamburg*, **3**, 31–56.
- VAN SAARLOOS, W., 1988, Front propagation into unstable shapes, *Phys. Rev. A*, **37**, 211–229.
- VIST, M. R., and DAVIS, J. H., 1990, Phase equilibria of cholesterol/dipalmitoyl-phosphatidylcholine mixtures.  $^2\text{H}$  nuclear magnetic resonance and differential scanning calorimetry, *Biochemistry*, **29**, 451–464.
- WAUGH, R., and EVANS, E. A., 1979, Thermoelasticity of red blood cell membrane, *Biophys. J.*, **26**, 115–132.
- WAUGH, R. E., SONG, J., SVETINA, S., and ZEKS, B., 1992, Local and nonlocal curvature elasticity in bilayer membranes by tether formation from lecithin vesicles, *Biophys. J.*, **61**, 974–982.
- WHEATER, J. F., 1994, Random surfaces: from polymer membranes to strings, *J. Phys. A*, **27**, 3323–3353.
- WIESE, W., HARIBICH, W., and HELFRICH, W., 1992, Budding of lipid bilayer vesicles and flat membranes, *J. Phys.: condens. Matter*, **4**, 1647–1657.
- WILLMORE, T. J., 1965, Note on embedded surfaces, *Anal. Scient. ale Univ. Iasi (Sect. Ia)*, **11**, 493–496; 1982, *Total Curvature in Riemannian Geometry* (Chichester, UK: Ellis Horwood).
- WINTERHALTER, M., and HELFRICH, W., 1986, Effect of voltage on pores in membranes, *Phys. Rev. A*, **36**, 5874–5876; 1992, Bending elasticity of electrically charged bilayers: coupled monolayers, neutral surfaces, and balancing stresses, *J. phys. Chem.*, **96**, 327.
- WINTZ, W., DÖBEREINER, H.-H., and SEIFERT, U., 1996, Starfish vesicles, *Europhys. Lett.*, **33**, 403–408.
- WITTEN, T. A., and LI, H., 1983, Asymptotic shape of a fullerene ball, *Europhys. Lett.*, **23**, 51–55.
- WORTIS, M., SEIFERT, U., BERNDL, K., FOURCADE, B., MIAO, L., RAO, M., and ZIA, R. K. P. 1993, *Dynamical Phenomena at Interfaces, Surfaces and Membranes*, edited by D. Beysens, N. Boccara and G. Forgacs (New York: Nova), pp. 221–236.
- WU, S. H. W., and MCCONNELL, H. M., 1975, Phase separations in phospholipid membranes, *Biochemistry*, **14**, 847–854.
- YEUNG, A., and EVANS, E., 1995, Unexpected dynamics in shape fluctuations of bilayer vesicles, *J. Phys. II France*, **5**, 1501–1523.
- YEUNG, A. K. C., 1994, *Mechanics of Inter-Monolayer Coupling in Fluid Surfactant Bilayers*, Ph.D. Thesis, University of British Columbia, Canada.
- ZHANG, Z., DAVIS, H. T., and KROLL, D. M., 1993, Scaling behavior of self-avoiding tethered vesicles, *Phys. Rev. E*, **48**, R651–654.
- ZHANG, Z., DAVIS, H. T., MAIER, R. S., and KROLL, D. M., 1995, The asymptotic shape of elastic networks, *Phys. Rev. E*, **52**, 5404–5413.
- ZHENG, W. M., and LIU, J., 1993, Helfrich shape equation for axisymmetric vesicles as a first integral, *Phys. Rev. E*, **48**, 2856–2860.
- ZILKER, A., ENGELHARDT, H., and SACKMANN, E., 1987, Dynamic reflection interference contrast (RIC-) microscopy: a new method to study surface excitations of cells and to measure membrane bending elastic moduli, *J. Phys. (France)*, **48**, 2138–2151.
- ZILKER, A., ZIEGLER, M., and SACKMANN, E., 1992, Spectral analysis of erythrocyte flickering in the  $0.3\text{--}4 \mu\text{m}^{-1}$  regime by microinterferometry combined with fast image processing, *Phys. Rev. A*, **46**, 7998–8001.
- ZIMMERMANN, U., 1992, Electric field-mediated fusion and related electrical phenomena, *Biochem. Biophys. Acta*, **694**, 227–277.
- ZUCKERMAN, D., and BRUINSMA, R., 1995, Statistical mechanics of membrane adhesion by reversible molecular bonds, *Phys. Rev. Lett.*, **74**, 3900–3903.